UNRAVELING NANOSCALE THERMAL TRANSPORT IN MULTILAYERED SEMICONDUCTORS

A Dissertation
Presented to
The Academic Faculty

by

Kartik Kothari

In Partial Fulfillment
of the Requirements for the Degree
Doctor of Philosophy in the
School of Physics

Georgia Institute of Technology
December 2019

UNRAVELING NANOSCALE THERMAL TRANSPORT IN MULTILAYERED SEMICONDUCTORS

Approved by:

Dr. Martin Maldovan, Advisor
School of Physics and
School of Chemical and Biomolecular Engineering
Georgia Institute of Technology

Dr. Asegun Henry
School of Mechanical Engineering
Massachusetts Institute of Technology

Dr. Dragomir Davidovic
School of Physics
Georgia Institute of Technology

Dr. Zhuomin Zhang
School of Mechanical Engineering
Georgia Institute of Technology

Dr. Phillip N. First
School of Physics
Georgia Institute of Technology

Date Approved: August 23, 2019

To my grandfathers, Dr. Chain Raj Kothari and Mr. Sajjan Mal Mehta

ACKNOWLEDGEMENTS

I would like to express my gratitude to my advisor, Prof. Martin Maldovan, for his support and constant guidance throughout my research. His drive for excellence and diligence at work inspired me and allowed me to develop as a researcher. I would also like to thank him for encouraging independent research while providing required and timely guidance throughout my progress as a PhD student. I am also grateful for his mentorship which provided enriching lifelong lessons. I would like to thank my dissertation committee members, Prof. Dragomir Davidovic, Prof. Asegun Henry, Prof. Phillip N. First and Prof. Zhuomin Zhang, for their interest in my research and spending their valuable time in reviewing my dissertation and providing valuable feedback. I also extend my gratitude to my research group members, Abhinav Malhotra and Juan Manuel Restrepo for their valuable inputs and collaborations.

I would like to express my gratitude to my parents, for their unconditional love and support and teaching me values and morals by leading a life which inspires me. I also thank my sister, Prerna, for being a source of love and enthusiasm whenever I needed. I am indebted for the sacrifices of my family which have allowed me to pursue my dreams. They have been cheerleaders for my success and a fountain of love even halfway across the world.

I would also like to thank my Art of Living family who continue to make me feel at home and cared for wherever I go. In particular, I would like to thank Preeti Bhat, Mona Shah-Joshi and Annelies Richmond for gifting me this family and mentoring me. Without their love and support, I don’t think I would have survived the PhD. I would like to

specially thank Umesh Unnikrishnan, Lipi Vora, Arti Verma and Abhishek Raj Bhatt for being there for me whenever I needed.

I want to express my deepest gratitude to my Guru, Sri Sri Ravi Shankar, for gracing my life with His presence and guidance. His wisdom and blessings are the light of my life – they have uplifted me in every situation of my life. I feel blessed to have been born in His lifetime and to be an instrument of spreading happiness.

TABLE OF CONTENTS

LIST OF FIGURES

LIST OF SYMBOLS

η	Roughness
θ_i	Incident angle
κ	Thermal conductivity, W cm^{-1} K^{-1}
$\Delta\kappa_{bulk}$	Enhancement of thermal conductivity beyond the bulk value
$\Delta\kappa_{iso}$	Enhancement of κ beyond isolated thin-film conductivity
ρ	Volumetric density
τ	Relaxation time
ω	Phonon frequency, rad s^{-1}
d	Period length
f	Phonon population away from equilibrium
f^0	Phonon population at equilibrium
f_{Si} / f_{Ge} / f_{GaAs}	Volume fraction of Si / Ge / GaAs
g	Phonon population deviation from equilibrium, $f - f^0$
$\vec{j}$	Thermal flux
$\vec{k}$	Wavevector
l	Phonon mean free path in nanostructures
l_x	*x*-component of mean free path in nanostructures
P_{ij}	Reflection Coefficient
Q_{ij}	Transmission Coefficient
T	Temperature
∇T	Temperature gradient
$\vec{v}$	Phonon group velocity

SUMMARY

Thermal transport at small length scales has attracted significant attention in recent years and various experimental and theoretical methods have been developed to establish the impact of nanostructuring on thermal conductivity. A thorough comprehension and control of thermal transport in nanoscale thermoelectric, microelectronic and optoelectronic devices is crucial since it is paramount to their optimum performance. The fundamental understanding of how phonons move and the physical mechanisms behind nanoscale thermal transport, however, remain poorly understood. In this thesis, we move beyond thermal conductivity calculations and provide a rigorous and comprehensive physical description of thermal phonon transport in layered nanostructures by solving the Boltzmann transport equation and extending the Beckman-Kirchhoff surface scattering theory with shadowing to precisely describe phonon-interface interactions.

We commence with analyzing periodic layered nanostructures called superlattices. We explicate in-plane thermal energy distribution in Si-Ge, GaAs/AlAs and their alloy-based superlattices by segregating it in two different heat transport modes having different physical properties at small length scales: layer-restricted and extended heat modes. We study how interface conditions, periodicity, and composition can be used to manipulate the distribution of thermal energy flow among such layer-restricted and extended heat modes. We predict the frequency and mean free path spectra of superlattices, which provide inputs for thermal management and investigation of the existence of phonon wave effects. For III-V superlattices, we provide an extensive microscopic analysis of phonon transport to enable rational thermal material design. We also predict the thermal conductivity of

realistic finite-sized GaAs/AlAs superlattices for efficient heat control in III-V superlattice-based optoelectronic devices.

Next, we provide a thorough analysis of cross-plane thermal conduction in GaAs/AlAs and their alloy-based superlattices while rigorously accounting for phonon interlayer coupling and interfacial structural characteristics. We present a comprehensive study of superlattice thermal transport, including structure-property relations, spectral and modal descriptions, and contrast it with in-plane heat conduction thereby explaining the resultant anisotropy in III-V semiconductor superlattices.

Through a rigorous understanding of interfacial phonon scattering, we uncover the phonon injection mechanism which provides pathways in modulating thermal conduction of specific layers within layered nanostructures. We examine thin film-on-substrate, a ubiquitously found architecture in nanostructured optoelectronic devices. We study thermal transport in thin films mounted over substrates and observe an unconventional behavior of thermal conductivity variation with film thickness. Specifically, we find an increased thermal conductivity with decreasing thickness which is attributed to phonon injection from substrate media. We provide an extensive investigation of the influence of interlayer thermal phonon coupling between the thin film and substrate on the thermal conductivity of the film and contrast it with bulk and isolated free-standing thin-film values. We consider Ge thin films grown over Si substrate and $Al_{0.1}Ga_{0.9}As$ thin films grown over GaAs substrate. We present a detailed spectral and structural analysis of thermal conductivity and its enhancement to enable rational thermal material design for optoelectronic applications.

We fundamentally investigate interfacial coupling through analyzing the transmission coefficient and its variation on the phonon frequency and interfacial roughness. We study thermal conductivity enhancement through a 2D visualization of the spatial distribution of heat through mapping phonon MFPs and their corresponding thermal conductivity contributions. We juxtapose the visual analysis for Ge bulk, isolated thin-film and thin-film on (Si) substrate and investigate the impact of roughness and temperature on this localized distribution of phonon MFPs.

We also include an elementary discussion on thermal phonon wave effects and classify the kinds of wave effects that can occur in a superlattice, namely, quantum confinement and thermal band gaps. We elaborate upon the mechanisms which cause them and provide strategies to enhance the possibility of their occurrence in layered nanostructures and highlight that a rigorous description of the physical and structural conditions including periodicity, interfacial roughness, volume fraction and temperature needs to be specified when quantifying the extent of coherent phonon conduction.

The results and insights in this thesis advance the fundamental understanding of heat transport in layered nanostructures and the prospects of rationally designing thermal systems with tailored phonon transport properties. Our conclusions in this work provide key physical insights into rational material design for thermal modulation and inputs for thermal management which is a crucial component in enhancing the performance of electronic, optoelectronic and thermoelectric devices. We conclude with highlighting future avenues and challenges that open up pathways for further in-depth research into nanoscale thermal transport.

CHAPTER 1. INTRODUCTION

Nanostructuring semiconductors has revolutionized technology by enabling the development and implementation of nanoscale devices for multifarious applications such as energy materials, microelectronics [1,2], optoelectronics [3,4], thermoelectrics [5-7] etc. A crucial aspect of designing efficient nanoscale devices is the ability to control nanoscale thermal transport. Fundamentally, the comprehension and modulation of physical mechanisms determining thermal transport in nanostructures is vital to rational design of devices. Thermal transport in semiconductors is primarily modelled by considering wave-packets of heat known as phonons. A phonon is a quasiparticle composed of collective vibrations of atoms in a medium which also characterizes chief phonon transport properties namely – group velocity, thermal capacity and mean free path (MFP). Nanostructuring semiconductors can impact all three of these – herein, group velocity and thermal capacity modulation occur through coherent phonon interactions whereas MFP modulation can occur through incoherent mechanisms as well. The focus of this work is to understand the interplay of various phonon scattering mechanisms to control the MFP of these heat carriers in nanostructured semiconductors.

1.1 Relevance of Nanoscale Thermal Transport

Conventional nanostructuring approaches have led to reduction of thermal conductivity from bulk values and present a dependence of the nanoscale conductivity on the characteristic length of the nanostructure such as thin-film conductivity decreases with reducing thickness [8-12]. The reduction in thermal conductivity finds key applications in thermoelectrics which are devices that generate electricity when subject to a thermal

gradient. The independent control of heat and charge carriers (i.e. phonons and electrons) enables efficient thermoelectric energy conversion since a reduction in thermal conductivity, while maintaining electrical conductivity, results in the enhancement of the thermoelectric figure of merit $ZT = S^2\sigma T / \kappa$, where S is the Seebeck coefficient, T is the temperature, σ is the electrical conductivity, and κ is the thermal conductivity [7]. Whereas thermal conductivity reduction has its applications, ineffective heat dissipation is currently a limitation on efficiency of nano and micro optoelectronic devices. Nano engineering of semiconductors also plays a central role in optimizing the performance of a broad variety of optoelectronic devices which find numerous applications such as photodetectors [3,4], quantum cascade lasers (QCLs) [4,13,14], modulators [15-17] etc. III-V semiconductor superlattices are extensively used in optoelectronic devices, specifically GaAs/AlAs and GaAs/$Al_xGa_{1-x}As$ superlattices find applications as photodetectors [18-20], photodiodes [21,22] and QCLs [4,14,23]. A key to peak performance of these modern optoelectronic devices is thermal management. Vertical Cavity Surface Emitting Lasers (VCSELs) suffer from reduction of effective gain at high temperature due to increased rate of Auger recombination of carriers which limits their output power [24,25]. Long laser lifetimes necessitate an upper bound on the temperature of active layers thus making efficient heat removal a crucial aspect of designing laser systems [26]. The efficiency and lifetime of a Light Emitting Diode (LED) depends on the junction temperature and the need for greater power dissipation inflicts a thermal limitation on their performance [27]. In photodetectors, thermally induced device failure occurs at high optical powers or photocurrents due to heat accumulation in the depletion layer [28]. Additionally, the maximum photocurrent and long term operation of photodetectors is also thermally limited due to dark current runaway

mechanisms [29,30]. Thus, investigation of thermal transport in semiconductor nanostructures would pave the way for efficient optoelectronic, thermoelectric and microelectronic device operations.

1.2 Interfacial Scattering of Phonons

Nanostructuring significantly transforms the thermal properties of semiconductors through interaction of phonons with interfaces and boundaries [31]. Thus, apprehension of phonon interfacial scattering at the nanoscale leads towards the ultimate goal in nanoscale heat conduction which is to be able to fundamentally understand and control the underlying physical mechanisms that govern phonon transport in order to rationally design thermal conduction.

1.2.1 Classical Theory

Nanoscale phonon transport is essentially governed by incoherent and coherent scattering of phonons [32-37]. Both these transport regimes are radically affected by the presence of boundaries and interfaces which control the extent to which phonons are scattered specularly and diffusively [31,32,38,39]. Numerous studies have established that thermal transport in nanostructures is significantly impacted by phonon interfacial interaction mechanisms. The two classical models describing phonon interaction with interfaces are the acoustic mismatch model (AMM) and the diffuse mismatch model (DMM). According to the AMM [40], phonon dynamics at the interface are determined under the assumption that phonons behave like plane waves. The transmission and reflection coefficients are determined by an acoustic analog of Fresnel's equations [41], specifically, by acoustic mismatch factors such as difference in volumetric density and

sound propagation velocities. The interfaces are assumed to be perfectly smooth and there is no room for diffusive scattering. On the other hand, the DMM [41,42] presents the extreme opposite and assumes that there is completely diffusive scattering at the interface i.e. the phonon scattering at the interface is independent of its incident mode or polarization albeit it is elastic. The probability of transmission at the interface is proportional to the density of states of the medium the phonon is emitted into. These models suffer from severe drawbacks such as neglecting interfacial roughness-induced scattering and there is experimental evidence to prove the inaccuracy of these models [1,43].

1.2.2 Contemporary Theories

Contemporary theoretical methods employed in nanoscale thermal transport and phonon interfacial interaction analysis can be divided into atomistic (e.g. molecular dynamics MD, density-functional-theory DFT) and continuum (e.g. Boltzmann transport) approaches each having its own advantages and drawbacks. MD techniques provide useful insights on the dependence of thermal conductivity on different physical variables and first-principle approaches allow to study the thermal conductivity based on DFT techniques. The detailed nanostructure surface features (which can be experimentally measured [44]) and their impact on thermal conductivity, however, are difficult to be incorporated. On the other hand, BTE approaches require the bulk phonon mean-free-path as input, which needs to be obtained using other methods (DFT) or fitting parameters. Once the bulk phonon mean-free-path is known, the thermal conductivity of multiple nanostructures (including surface characteristics) can be readily obtained without using fitting parameters. Another contrast between atomistic and continuous approaches is the length scale range; atomistic simulations are computationally intensive at large scales preventing the prediction of nano-

to-bulk thermal properties, while the BTE allows bulk-to-nanoscale predictions but requires incorporation of wave effects (e.g. coherent interference and confinement) at very small length scales.

Recent works have employed atomistic formulations to analyze interfacial phonon transmission. Z. Tian et al [45] studied phonon transmission across an Si/Ge interface using atomistic Green's function (AGF) approach and concluded that atomic mixing increases transmission and interfacial conductance. B. Latour et al. [46] used AGF with first-principle force constants to model transmission across a perfectly smooth Si/Ge interface and found that mass-mismatch was the key parameter in controlling transmission and reflection. W. Zhang et al [47] extended the AGF formulation to account for interfacial phonon transport in Si/Ge heterostructures while accounting for effects such as strain. L. Jia et al [48] employed AGF to study variation in transmission with roughness and found that there existed a roughness for which the enhancement of transmission and conductance (beyond that for a sharp interface) showed a maximum. They attributed this to a trade-off between increasing diffusive scattering and broadening of frequency transport window with increasing interfacial roughness. S. Merabia et al [49] used molecular dynamics (MD) to analyze thermal boundary conductance across rough interfaces and found that interfacial boundary shape played a key role in determining conductance. They found that sinusoidal and wavy interfaces resulted in maximum Kapitza conductance. T. English et al [50] used non-equilibrium MD and studied the dependence of interfacial conductance on multiple parameters and found that density of states overlap between materials across the interface generally increases conductance but presence of compositional disorder can cause it to reduce. L. Sun et al [51] employed the MD wave-packet method to investigate phonon

transport at Si/Ge interfaces and found that transmission reduces with increasing roughness. A. Alkurdi et al [52] used lattice dynamics with ab initio force constants and presented a modal analysis to examine the dependence of the critical angle of transmission at an Si/Ge interface on parameters such as temperature, interfacial bonding and interaction. Despite extensive studies using atomistic approaches, they were limited in accounting for anharmonicity, accurately modelling interfacial features and are often times computationally expensive when providing mode-resolved transmission information and scaling to large characteristic lengths. Thereby, while atomistic approaches can provide qualitative trends in interfacial phonon scattering, their extension to accurate thermal conductivity predictions in devices involving interfaces is challenging.

1.3 Thermal Transport in Nanostructures - Superlattices

The previous extensive study of interfacial scattering indicates the importance of understanding phonon interfacial interactions which have a clear influence on thermal transport in nanostructured materials involving phonon exchange between materials. A ubiquitously employed nanostructure involving interfacial interactions across layered materials is superlattice. Superlattices are single-crystal nanostructures consisting of periodically arranged layered materials that can provide physical properties that are radically different from those corresponding to the constituent materials. Their ease of manufacture and tunability has made superlattices a standard platform for semiconductor devices with widespread applications in optoelectronics [3,4], thermoelectrics [5-7,53], energy conversion [5], electronics [54], photonics [55], and phononics [56]. For instance, Si-Ge based superlattices find application in thermoelectrics [57-59] while III-V semiconductor superlattices find applications in optoelectronics including photodiodes

[21,22] and quantum cascade lasers (QCLs) [14,23]. Thermal management in such devices is vital to their optimum performance thereby making a thorough comprehension of superlattices' thermal transport properties essential.

1.3.1 Theoretical Methodologies

In recent years, the transport of thermal phonons in superlattices has been investigated by studying the effects of coherent [33,34,36,60] and incoherent [32,61,62] surface scattering of phonons. The coherent scattering of phonons involves the preservation of phonon phase upon interaction with interfaces, and an appropriate periodicity in the nanostructure may generate phonon wave interference effects under certain conditions [33,63]. Conversely, incoherent scattering involves randomization of phonon phases and conventionally manifests as a reduction in the thermal conductivity. We next survey a variety of atomistic and continuum methods which have been used to investigate superlattices, in both coherent and incoherent regimes of thermal transport.

1.3.1.1 Molecular Dynamics Formalism

Using molecular dynamics, Daly et al.[64] studied thermal transport in a simplified model for GaAs/AlAs superlattices. They found that for superlattices having smooth interfaces, the cross-plane thermal conductivity shows a minimum as a function of the superlattice period. The existence of such minimum was previously predicted using wave theory and indicates the presence of phonon wave effects[65]. In contrast, for superlattices with interfacial species mixing, the thermal conductivity increased with period length as observed in experiments[62,66]. Trends in cross-plane thermal conductivity in superlattices were also investigated by Chen et. al.[67]. They found that a minimum in

thermal conductivity occurred if the MFP is close to or larger than the period and the lattice constants are similar. From MD simulations [62,64-71], it is clear that a minimum in thermal conductivity exists if the superlattice interfaces are perfect and they vanish for interfaces with species mixing. The precise determination of phonon wave effects and their relation to surface features (i.e. roughness and correlation lengths) is however difficult to obtain with current MD models.

1.3.1.2 First Principles Formalism

Using first-principles, Garg et al.[72] analyzed the thermal conductivity of Si/Ge superlattices with relatively smooth surfaces and found that, for increasing period, the in-plane conductivity increases monotonically while a minimum was observed for the cross-plane configuration. More recently, the cross-plane thermal conductivity in Si/Ge superlattices via ab initio calculations was investigated and compared with experiments by Chen et. al.[73], and found that surface segregation and intermixing of atoms may further reduce thermal conduction. In addition, Garg et. al.[74] predicted using DFT that short-period superlattices with perfect interfaces could have high conductivity due to reduced availability of scattering channels. Tian et al.[75] also calculated the cross-plane superlattice thermal conductivity using atomistic Green's functions and found an optimum period length which minimizes the thermal conductivity. Detailed surface features and their effects are difficult to include in first-principle approaches while Green's function methods approximate thermal conduction by considering ballistic transport.

1.3.1.3 Boltzmann Transport Formalism

In addition to atomistic models, the Boltzmann transport equation (BTE) was employed by Chen [32,61,76] to study in-plane and cross-plane thermal conductivity in GaAs/AlAs and Si/Ge superlattices, respectively. It was found that accounting for frequency dependent internal scattering and partially diffuse and partially specular interfaces was fundamental to obtain agreement between theory and experiments. Liu et. al.[77] evaluated the cross-plane thermal conductivity of Si/SiGe superlattices theoretically using BTE and experimentally by the 3ω technique. The thermal conductivity was found to decrease with decreasing ratio of layer thickness, specularity and period length. These BTE models consider frequency independent phonon-surface interactions and the interface specularity is thus incorporated as an empirically adjusted parameter. More recently, Aksamija et al.[78] proposed a simplified BTE model to calculate the thermal conductivity of $Si_xGe_{1-x}/Si_yGe_{1-y}$ superlattices using a surface specularity parameter dependent on wavevector and interface roughness. The model was employed to obtain the anisotropy, temperature, and period variation of the thermal conductivity. Building up on this model, Mei et al.[79] recently calculated the in-plane and cross-plane thermal conductivities of III-V superlattices. Being an improvement with respect to constant specularity models, the proposed BTE approach does not consider phonon reflections and transmissions at the interfaces, which is the fundamental principle that gives rise to phonon coherent interference and significantly influences the superlattice thermal conductivity.

1.3.2 Experimental Investigations

Experimental measurements of superlattice thermal conductivity have shown a variety of trends. Lee et. al.[62] showed that the cross-plane thermal conductivity of Si-Ge superlattices increased with increasing period length and suddenly decreased due to

formation of dislocations. On the other hand, Capinski et. al.[80] measured the cross-plane thermal conductivity of GaAs/AlAs superlattices and found that it increases with increasing period length. Furthermore, Huxtable et. al.[81] observed that the thermal conductivity of Si/SiGe alloy superlattices increased with increasing period while that of $Si_xGe_{1-x}/Si_yGe_{1-y}$ superlattices was weakly dependent on period. More recently, experiments on epitaxial oxide superlattices by Ravichandran et. al.[33] exhibited a minimum in the thermal conductivity as a function of period length, thereby demarcating a transition from coherent to incoherent phonon surface scattering. In terms of the temperature dependence, experiments show that the thermal conductivity of Si/Ge superlattices increase up to a temperature of ~200 K, after which it remains fairly constant[62,81-84]. More recently, Luckyanova et. al. [36] studied the impact of varying total thickness of GaAs-AlAs superlattice structures and found that for relatively low temperatures (T<150K), the thermal conductivity increased linearly with the number of periods. This result constituted their basis to deduce coherent phonon transport in superlattices. In a recent study, Cheaito et. al. [85] confirmed the experimental measurements in [36] and further explored the impact of varying period thickness and total superlattice thickness. They concluded that inspecting both physical variables is crucial to comprehending the relative contribution of coherent and incoherent phonons towards heat conduction in superlattices.

1.4 Thermal Transport in Nanostructures – Nanomembranes

The study of interfacial and boundary interactions of thermal phonons also plays a key role in determining thermal transport in layered nanostructures such as nanomembranes and thin film-on-substrate architectures which are ubiquitous configurations in optoelectronic devices [83,86-89]. Optoelectronic devices such as

photodetectors, LEDs, lasers etc. are often fabricated using the thin film-on-substrate architecture using a wide range of III-V semiconductor compounds [89-92]. Regulating thermal conduction in these devices is critical to optimum performance and can enhance their efficiency. For instance, heat dissipation in laser system design is vital to longer lifetimes of active layers to maintain an upper bound on temperature [26]. The junction temperature of an LED determines its lifetime and efficiency, thereby making thermal dissipation a crucial factor in limiting their performance [27].

1.4.1 Theoretical Methods

There has been extensive amount work on achieving reduced thermal conduction in nanomembrane systems, but approaches that can enhance thermal conduction have been limited. In particular, being able to devise physical mechanisms that would allow to increase thermal conduction is of crucial importance in the efficiency of electronic and optoelectronic devices. In recent years, physical mechanisms behind thermal transport in nanomembranes have been analyzed via atomistic and continuum based approaches [8-12,93-100]. Using molecular dynamics, first principles and lattice dynamics, the in-plane and cross-plane Si thin film thermal conductivity has been predicted from ballistic to diffusive limits for a wide range of sizes and temperatures [97,99,101]. D.P. Sellan et al utilized the lattice Boltzmann formalism to study cross-plane thermal transport in Si thin films and found that frequency dependent thermal conductivity contribution varied with thickness [11]. C.J. Gomes et al examined in-plane and cross-plane thermal conductivity in Si thin films using equilibrium MD and concluded that thermal conductivity reduced with reducing thickness [101]. Continuum approaches based on the Boltzmann Transport Equation (BTE) have also been used to predict heat conduction in silicon nanomembranes

while considering averaged momentum-dependent specularities [100], frequency-dependent specularities [12], and Beckmann-Kirchhoff formalism [102,103]. Investigations of thermal conduction in nanomembranes also include thin films on substrates such as silicon on insulator (SOI) architectures [9,100,104]. Importantly, although enhancing thermal conduction is essential to create highly efficient electronics and optoelectronics, to date, all studies on nanomembranes have shown that thermal conduction decreases as the spacing is decreased and the development of approaches that enable to increase heat conduction in these nanosystems has been difficult.

1.5 Objectives of This Work

Through this literature survey we discern that thermal transport manipulation is critical to enhancing efficiency of nanoscale devices in a wide variety of applications including optoelectronics, microelectronics and thermoelectrics. A diverse set of devices necessitate a broad range of control of thermal properties, which not only includes a handle on the thermal conductivity but also incorporates modulating heat conduction at a spectral level by regulating the amount of heat carried by varying phonon frequencies, wavelengths and MFPs. A rigorous description also moves beyond thermal conductivity prediction, and delineates the thermal energy distribution within nanostructures by elucidating the various phonon trajectories and interactions and the factors that impact phonon movement. A key requirement to achieving such a detailed analysis of thermal transport in layered nanostructures is a rigorous theoretical description of phonon interfacial scattering incorporating experimentally determinable interfacial characteristics. Incorporating the interfacial scattering mechanism through appropriate boundary conditions, along with other phonon scattering mechanisms and using a modal analysis would provide a complete

picture of thermal transport in nanostructures. This would not only provide us crucial inputs for thermal management during nanoscale device design but also open avenues for exploring unique thermal transport phenomenon such as phonon wave effects – thermal band gaps and phononic quantum wells.

1.6 Dissertation Structure

In Chapter 2 of this thesis, we expound a comprehensive model elucidating phonon interfacial interaction which accounts for interfacial features such as roughness and correlation length, phonon properties such as frequency, group velocity and incident angle and material properties of media adjacent to the interface. We adopt a Boltzmann Transport Equation (BTE) formalism which yields a quantitative model that predicts thermal transport in nanostructures across manifold length scales ranging from nanometers to millimeters. We integrate the BTE formalism along with the interfacial scattering model through boundary conditions rooted in the principle of detailed balance of phonons and the conservation of thermal flux to explicate an accurate thermal transport picture.

In Chapter 3, we study the impact of various structural characteristics such as characteristic length, interfacial roughness and volume fraction on not only the thermal conductivity predictions but also illustrate the thermal energy distribution based on various interfacial interactions of phonons. We present a meticulous analysis of thermal phonon spectra by highlighting the amount of heat carried by different phonon frequencies and mean free paths. These can provide vital inputs in rational thermal material design by implementing mechanisms which can modulate thermal conduction of a specific band of phonons. We also furnish a microscopic analysis of thermal transport by analyzing the

amount of heat carried by thermal phonons subject to various trajectories and examine the amount of thermal conduction continually carried after multiple phonon interactions with interfaces. We implement a finite sized analysis by determining the thermal conductivity of superlattices with a finite number of periods which administers thermal predictions for realistic applications and devices. We carry out the above outlined rigorous thermal analysis of semiconductor superlattices composed of Si/Ge, GaAs/AlAs and their alloys in the in-plane and cross-plane configurations. We contrast these configurations and study the anisotropy as a function of period length and interfacial roughness. We also specify a modal analysis of thermal transport wherein we provide the conductivity contribution of different phonon modes. Next, we explicate in detail the interlayer phononic coupling emerging from the phonon interfacial scattering and how that can modulate thermal conduction in thin-films. We apply the principles of the phonon injection mechanism and interlayer coupling to an important nanostructure configuration – thin-film on substrate architecture. We quantitatively predict how film thickness, temperature, and roughness influence substrate-coupling which impacts the thermal properties of a thin-film. Additionally, we spectrally examining thermal conductivity and the coupling-induced conductivity enhancement in FOS systems. Lastly, we expatiate on interfacial coupling by analyzing the frequency and roughness dependence of the transmission coefficient and visually depict the impact of interlayer coupling on spatial distribution of thermal energy by providing a localized spatial distribution of thermal phonon MFPs.

In Chapter 4, we deliberate over phonon wave effects in periodic nanostructures and classify them into two categories for superlattices depending on the phonon trajectories. We highlight the importance of studying the thermal energy distribution

caused by various trajectories and its relevance in understanding the impact of wave effects on thermal conduction. In this forthcoming research field, we outline some strategies that can enhance the possibility of their occurrence. We also specify the parameters needed to provide a rigorous description of wave effects and comprehend the extent of coherent vs incoherent phonon transport.

In Chapter 5, we conclude the dissertation with a summary of our observations of thermal transport in layered nanostructures, specifically superlattices and thin-films on substrate while highlighting the key results and findings. We also provide an outlook about the future avenues of research and open challenges in the field of nanoscale thermal transport.

CHAPTER 2.

CONTINUUM MODEL FOR MODE-WISE HEAT TRANSFER

We investigate nanoscale thermal transport in layered nanostructures by employing the Boltzmann Transport formalism along with an accurate model for phonon interfacial scattering. We commence with outlining a methodology to compute the thermal conductivity in nanostructures through a combination of the Boltzmann Transport Equation and the Fourier's Law. Thereafter, we provide a rigorous statistical analysis to study scattering of phonons from a rough interface and thereby, determine the transmission and reflection coefficients for thermal phonons. We next highlight the boundary conditions associated with different layered nanostructures and thermal transport configurations, specifically, in-plane heat conduction in superlattices and film-on-substrate architectures and cross-plane transport in superlattices. Broadly speaking, these boundary conditions consist of detailed balance of phonons at interfaces and utilizing symmetries within the nanostructure. Integrating the phonon scattering model, Boltzmann formalism and the appropriate boundary conditions, we are able to predict the thermal conductivity of nanostructures as a function of a variety of structural and physical parameters such as characteristic length, volume fraction, roughness, temperature etc. Our mode-wise implementation of computing thermal transport allows us to move beyond conductivity predictions and also determine thermal spectra within nanostructures.

2.1 Thermal Conductivity

The thermal conductivity of nanostructures is calculated by using the well-established Fourier's law of heat conduction, which is given by

$$\vec{j} = -\kappa \vec{\nabla} T \tag{1}$$

where $\vec{j}$ is the heat flux, κ is thermal conductivity and $\vec{\nabla} T$ is the temperature gradient. Kinetic theory establishes that the heat flux[31] $\vec{j}$ is given by the product of the energy $\hbar\omega$ carried by phonons, their distribution functions *f* and their velocities $\vec{v}$. Integration over all possible phonons with wavevectors $\vec{k}$ gives the thermal flux as

$$\vec{j} = \frac{1}{(2\pi)^3} \sum_p \int \hbar \omega_{\vec{k},p} f_{\vec{k},p} \vec{v}_{\vec{k},p} d^3k \tag{2}$$

where the subscript *p* denotes the different polarizations of phonons (i.e. longitudinal and transverse). The thermal conductivity κ of the nanostructure is calculated by combining Eqs. (1) and (2) and integrating the flux along the characteristic length t_0 as

$$-\kappa \vec{\nabla} T = \frac{1}{t_0} \int \vec{j} dl \tag{3}$$

The calculation of the thermal conductivity using Eqs. (2) and (3) requires the distribution of phonons $f_{\vec{k},p}$ for the superlattice, which is determined by the Boltzmann Transport Equation (BTE).

2.2 Boltzmann Transport Equation

The generalized form of the Boltzmann Transport Equation, which allows to obtain the phonon distribution functions $f_{\vec{k},p}$, is given by[31]

$$\frac{\partial f_{\vec{k},p}}{\partial t} + \vec{v}_{\vec{k},p} . \vec{\nabla} f_{\vec{k},p} = \left(\frac{\partial f_{\vec{k},p}}{\partial t} \right)^{scatt} \tag{4}.$$

Since we are interested in solving the BTE for phonons in the steady-state case, i.e. constant heat flux, the first term vanishes. Using the single-mode relaxation time approximation[31], the scattering term on the right-hand side of Eq. (4) is given by $\frac{f^0 - f}{\tau}$, where f^0 is the equilibrium phonon distribution function given by the Bose-Einstein distribution function and $\tau = \tau(\vec{k}, p, T)$ is the phonon relaxation time, which is a function of the wavevector $\vec{k}$, polarization *p*, and temperature *T*. Given that the above equation is applicable for each polarization *p* and each $\vec{k}$-mode, subscripts will be omitted. Expanding $f = f^0 + g$, where g is the deviation function from the equilibrium, Eq. (4) reduces to

$$\vec{v} . \vec{\nabla} f = -\frac{g}{\tau} \tag{5}$$

In general *f* is a function of the position vector $\vec{r}$. We define our coordinate system such that the nanostructure is uniform in the *y* direction. The thermal gradient is applied in the *x*-direction so the equilibrium distribution f^0 is dependent only on the *x*-coordinate and the distribution *f* is independent of the *y* coordinate due to continuous translation symmetry. Using these coordinate conventions, we can transform Eq. (5) into

$$v_x \frac{\partial f}{\partial x} + v_z \frac{\partial f}{\partial z} = -\frac{g}{\tau} \tag{6}$$

Assuming that the deviation from equilibrium is small, i.e. $g << f^0$, we obtain the general solution to first order of the differential equation (6), where g can be written as a function of the x_i coordinate (specified by the configuration of thermal transport) and an arbitrary function $\varphi_{\vec{k}}$

$$g_{\vec{k}}(x_i) = -v_x \tau \frac{\partial f^0}{\partial T} \frac{\partial T}{\partial x} \left[1 + \varphi_{\vec{k}} \exp\left(\frac{-x_i}{v_{x_i} \tau} \right) \right] \tag{7}$$

The function $\varphi_{\vec{k}}$ determining the phonon distribution function is rigorously obtained by applying boundary conditions of the specific nanostructure, which are implemented after a careful analysis of phonon surface scattering at the interfaces. Once $\varphi_{\vec{k}}$ (and therefore $g_{\vec{k}}$) is calculated, Eqs. (1) – (3) allow to obtain the resultant thermal conductivity of the superlattice.

2.3 Phonon Scattering at Rough Surfaces

For layered nanostructures, the boundary conditions are given by an energy balance upon scattering of phonons at the rough interfaces. We use a rigorous statistical analysis to study the scattering of thermal phonons from rough surfaces. The scattering of electromagnetic waves from rough surfaces has been studied in detail by Beckmann and Spizzichino[103]. This analysis however is limited to free surfaces (e.g. solid-air interfaces) preventing the study of phonon scattering at surfaces between two different

solid materials. We employ a generalized analysis of surface scattering[105], where the Beckmann-Kirchhoff theory has been extended to include forward scattering i.e. the reflection and transmission of phonons at a rough interface between two homogeneous and isotropic solids. We outline below the main points to obtain a generalized solution for scattering between two interfaces and subsequently extend it to the case of superlattices.

Consider the height *z* of an interface between two media 1 and 2 (with respect to a middle plane) given by the function $z = \zeta\left(x, y\right)$, where the average value of *z*, i.e. $<\zeta\left(x, y\right)>$ with respect to the plane is zero. The region for media 1 is given by $z > \zeta\left(x, y\right)$ and that for media 2 is given by $z < \zeta\left(x, y\right)$. Assuming that ζ is a random variable representing the heights of the surface, the roughness of the surface η is defined as the standard deviation of ζ. Without losing generality, we assume that the incident wavevector $\vec{k}$ lies in the *x*-*z* plane. To describe the interaction of phonons with an interface, consider $\mathrm{u} = \exp\left[i\left(\vec{k}.\vec{r}\right) - \omega t\right]$ be the displacement phonon field which is the solution of the Helmholtz equation $\Delta u + k^2 u = 0$ [103]. When the radius of curvature of the interface is much larger than the wavelength, the Kirchhoff boundary conditions apply[103]

$$u\,|_{z\to\zeta^+} = \left(1+\Re\right)e^{i\vec{k}.\vec{r_s}},\ \frac{\partial u}{\partial n}|_{z\to\zeta^+} = i\left(1-\Re\right)\left(\vec{k}.\vec{n}\right)e^{i\vec{k}.\vec{r_s}} \tag{8}$$

$$u\,|_{z\to\zeta^-} = \Im e^{i\vec{k}.\vec{r_s}},\ \frac{\partial u}{\partial n}|_{z\to\zeta^-} = i\Im\left(\vec{\tilde{k}}.\vec{n}\right)e^{i\vec{k}.\vec{r_s}} \tag{9}$$

where $\vec{n}$ denotes the unit vector normal to the surface $z = \zeta\left(x, y\right)$ at point $\vec{r_s} = x\hat{x} + y\hat{y} + \zeta\left(x, y\right)\hat{z}$ and $\vec{\tilde{k}}$ is the local refracted wave vector. Also, $\Re$ and $\Im$ denote the standard reflection and transmission coefficients from a *perfectly smooth* surface, respectively. The solution of the Helmholtz equation at a distance *R* from the surface, at $\overrightarrow{R'}$ and $\overrightarrow{R''}$ in medium 1 and 2, respectively, gives

$$u\left(\overrightarrow{R'}\right) \approx \frac{ie^{ik_1 R}}{4\pi R}\int_S \left[\Re\left(\vec{k} - \overrightarrow{k'}\right) - \left(\vec{k} + \overrightarrow{k'}\right)\right].\vec{n}e^{i\left(\vec{k}-\overrightarrow{k'}\right).\vec{r_s}}dS \tag{10}$$

$$u\left(\overrightarrow{R''}\right) \approx \frac{ie^{ik_2 R}}{4\pi R}\int_S \Im\left(\vec{\tilde{k}} + \overrightarrow{k''}\right).\vec{n}e^{i\left(\vec{k}-\overrightarrow{k''}\right).\vec{r_s}}dS \tag{11}$$

where $\overrightarrow{k'}$ is the reflected wave vector, $\overrightarrow{k''}$ is the overall reflected wave vector, k_1 is the magnitude of the incident and reflected wavevector, and k_2 is the magnitude of the refracted wave vector. Carrying out a rigorous statistical analysis[105], one can obtain the reflection P_{ij} and transmission Q_{ij} coefficients from a *rough* interface, where *i* and *j* denote the two solid media across the surface, which are given by

$$P_{ij} = \Re_{ij}^2 \exp\left(-4\eta^2 k_i^2 \cos^2\theta_i\right) \tag{12}$$

$$Q_{ij} = \left(1 - \Re_{ij}^2\right)\exp\left(-\eta^2\left(k_i \cos\theta_i - k_j \cos\theta_j\right)^2\right) \tag{13}$$

where

$$\Re_{ij}^2 = \left(\frac{\rho_i v_i \cos\theta_i - \rho_j v_j \cos\theta_j}{\rho_i v_i \cos\theta_i + \rho_j v_j \cos\theta_j} \right)^2 \tag{14}$$

In these equations, ρ_i, θ_i, and v_i denote density, incident angle, and group velocity $v_i = \nabla_{\mathbf{k}} \omega_i(\vec{k})$, where $\omega_i(\vec{k})$ is the phonon dispersion relation in medium *i*, respectively. The reflection and transmission coefficients are subsequently extended to account for shadowing effects [102]. Since $\Re_{ij}^2 = \Re_{ji}^2$, we have $Q_{ij} = Q_{ji}$, which is the principle of detailed balance for phonons. Independent of the nature of the boundary conditions, the law of reflection and refraction states that the tangential component of the wavevector is conserved. That is

$$k_i \sin\theta_i = k_j \sin\theta_j \tag{15}$$

For incident angles larger than the critical angle, $\Re_{ij}^2 = 1$ and phonons are subject to total internal reflection and therefore restricted to propagate within a layer. Importantly, the surface scattering model described above thus allows to obtain the phonon thermal energy reflected and transmitted at *rough* interfaces.

2.4 Boundary Conditions and Energy Balance at Interfaces

In this section, we investigate thermal transport in a variety of layered nanostructures and illustrate the corresponding boundary conditions for energy balance along with their schematic.

2.4.1 Superlattices – In-plane Conduction

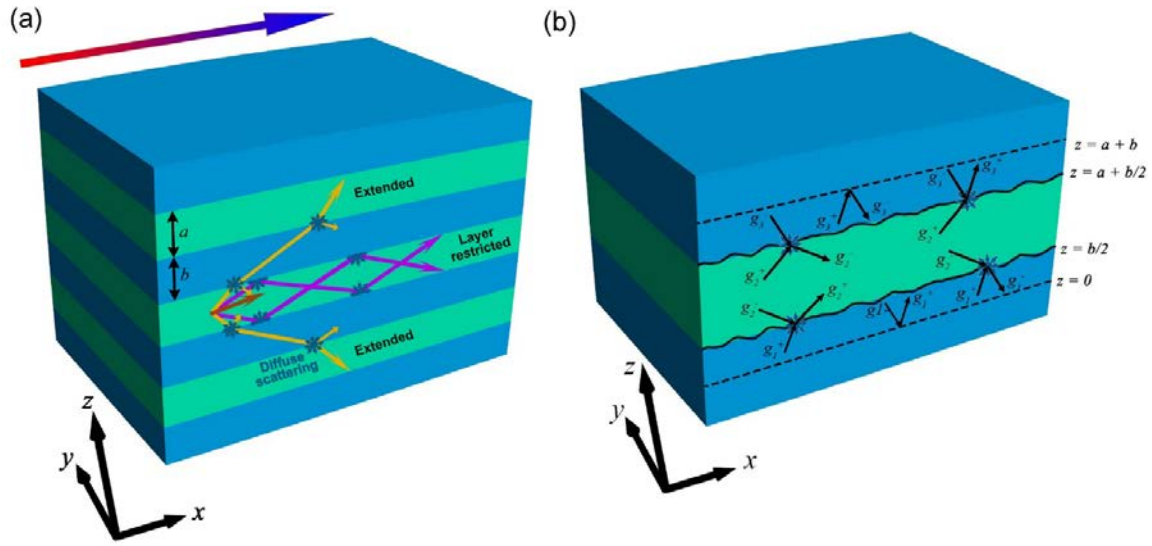

Figure 1. (a) Schematic for extended and layer-restricted phonons (yellow and purple arrows respectively). Phonons layer-restricted by MFP reduction are shown by an orange arrow. The thermal gradient in the x-direction is denoted by the overhead arrow where red and blue denote hot and cold temperatures respectively. (b) Schematic of interfacial scattering from rough interfaces in a superlattice (i.e. phonon coupling) where the unit cell is demarcated by dashed lines.

2.4.1.1 Thermal Energy Distribution

A fundamental understanding of superlattice thermal transport requires not only to establish the thermal conductivity but also to elucidate how phonons move within the system. Developing such deep understanding necessitates the establishment of the amount of phonons that are specularly and diffusely scattered at the interfaces, the amount of heat that is channeled within a single superlattice layer, and the amount of heat that is transported across multiple layers. We move beyond thermal conductivity calculations and establish how thermal phonons are transported within the superlattices. Phonons originating at point within a superlattice can follow different paths depending on their frequency and incident angle. Some phonons can reach an interface and undergo specular transmission into the adjacent layer and continue to propagate in the different layers of the

superlattice. We call these “extended phonons”. Phonons can also reach an interface and undergo total reflection due to two different physical principles: total internal reflection or band structure mismatch (i.e. no accessible frequency on the adjacent layer). Since these phonons move within a single layer, they are called “layer–restricted phonons” (Figure 1(a)). Note that if the reduced phonon MFP is less than the distance needed to reach an interface in the direction of its wavevector, the phonons will also be layer restricted. Thus, a precise physical description of phonon transport in superlattices predicts the spatial distribution of thermal energy flow and allows a segregation of the amount of heat carried by extended and layer-restricted phonons.

2.4.1.2 Boundary Conditions – Symmetries and Detailed Balance

Thermal transport in layer-restricted phonons is modelled as phonon mode transport in a thin-film. On the other hand, we comprehend thermal transfer by applying the principle of detailed balance of energy at the interface along with utilizing appropriate symmetries within the superlattice structure. Due to translational symmetry along the *z*-direction, the BTE needs to be solved only within a single unit cell of the superlattice, which when repeated in the *z*-direction reproduces the entire superlattice. In our calculations, the unit cell begins halfway through a layer of material B and extends halfway into the next layer of material B as illustrated in Figure 1(b).

We write the general solution of g given by Eq. (7) as follows [106]

$$g_i^{\pm} = -v_{x,i}\tau_i \frac{\partial f_i^0}{\partial T}\frac{\partial T}{\partial x}\left[1+\varphi_i^{\pm}\left(\vec{k}\right)\exp\left(\frac{\mp z}{|v_{z,i}|\tau_i}\right)\right] \tag{16}$$

where the subscript *i* denotes a particular layer in the superlattice and the superscript '+' or '–' denotes the direction of k_z, where '+' denoted a positive k_z and vice versa. We define $l_{x,i} = v_{x,i}\tau_i$ and $l_{z,i} = \left|v_{z,i}\right|\tau_i$. To exploit the translational symmetry of the superlattice, we consider (for each layer) translated versions of the general solution of *g*

$$
\begin{aligned}
g_1^+ &= -l_{x,1}\frac{\partial f_1^0}{\partial T}\frac{\partial T}{\partial x}\left[1+\varphi_1^+\left(\vec{k}\right)\exp\left(-\frac{z+(b/2)}{l_{z,1}}\right)\right] \\
g_1^- &= -l_{x,1}\frac{\partial f_1^0}{\partial T}\frac{\partial T}{\partial x}\left[1+\varphi_1^-\left(\vec{k}\right)\exp\left(+\frac{z-(b/2)}{l_{z,1}}\right)\right] \\
g_2^+ &= -l_{x,2}\frac{\partial f_2^0}{\partial T}\frac{\partial T}{\partial x}\left[1+\varphi_2^+\left(\vec{k}\right)\exp\left(-\frac{z-(b/2)}{l_{z,2}}\right)\right] \\
g_2^- &= -l_{x,2}\frac{\partial f_2^0}{\partial T}\frac{\partial T}{\partial x}\left[1+\varphi_2^-\left(\vec{k}\right)\exp\left(+\frac{z-\left(a+(b/2)\right)}{l_{z,2}}\right)\right] \\
g_3^+ &= -l_{x,3}\frac{\partial f_3^0}{\partial T}\frac{\partial T}{\partial x}\left[1+\varphi_3^+\left(\vec{k}\right)\exp\left(-\frac{z-\left(a+(b/2)\right)}{l_{z,3}}\right)\right] \\
g_3^- &= -l_{x,3}\frac{\partial f_3^0}{\partial T}\frac{\partial T}{\partial x}\left[1+\varphi_3^-\left(\vec{k}\right)\exp\left(+\frac{z-\left(a+(3b/2)\right)}{l_{z,3}}\right)\right]
\end{aligned}
\qquad (17)
$$

Note that since the phonon frequency remains constant during reflection and transmission, we can simplify the expressions in Eq. (17) and omit the term $\frac{\partial f_i^0}{\partial T}\frac{\partial T}{\partial x}$ when

applying the boundary conditions. By considering the mirror symmetries, the following boundary conditions apply for the superlattice [106]

$$g_1^+ = g_1^- \ \ at \ \ z = 0 \tag{18}$$

$$g_3^+ = g_3^- \ \ at \ \ z = a + b \tag{19}$$

In addition, at the interfaces between different materials, energy balance for phonon reflection and transmission establishes that

$$g_1^-\left(-k_z\right) = P_{12} g_1^+\left(k_z\right) + Q_{12} g_2^-\left(-k_z'\right) \qquad at\ z = b/2 \tag{20}$$

$$g_2^+\left(k_z'\right) = P_{21} g_2^-\left(-k_z'\right) + Q_{12} g_1^+\left(k_z\right) \qquad at\ z = b/2 \tag{21}$$

$$g_2^-\left(-k_z'\right) = P_{23} g_2^+\left(k_z'\right) + Q_{23} g_3^-\left(-k_z\right) \qquad at\ z = a + b/2 \tag{22}$$

$$g_3^+\left(k_z\right) = P_{32} g_3^-\left(-k_z\right) + Q_{23} g_2^+\left(k_z'\right) \qquad at\ z = a + b/2 \tag{23}$$

Note that the primed notation is to emphasize that while in medium 1 the wavevector is $\vec{k}$, the wavevector in medium 2 is $\vec{k}'$. The solution of the system of Eqs. (20) - (23) fully determines the functions $\varphi_i^{\pm}\left(\vec{k}\right)$ which establish the distribution of phonons $g_i^{\pm}$ deviated from equilibrium for each layer [Eqs. (17)]. Calculation of the distribution functions $g_i^{\pm}$ allows us to determine the thermal conductivity using Eqs. (2) and (3). Note that all variables in our theoretical framework depend on the wavevector $\vec{k}$, allowing to perform a full frequency-dependent analysis of all phonon transport properties,

including a rigorous treatment of phonon scattering at the interfaces and phonon coupling between superlattice layers.

2.4.2 Superlattices – Cross-plane Configuration

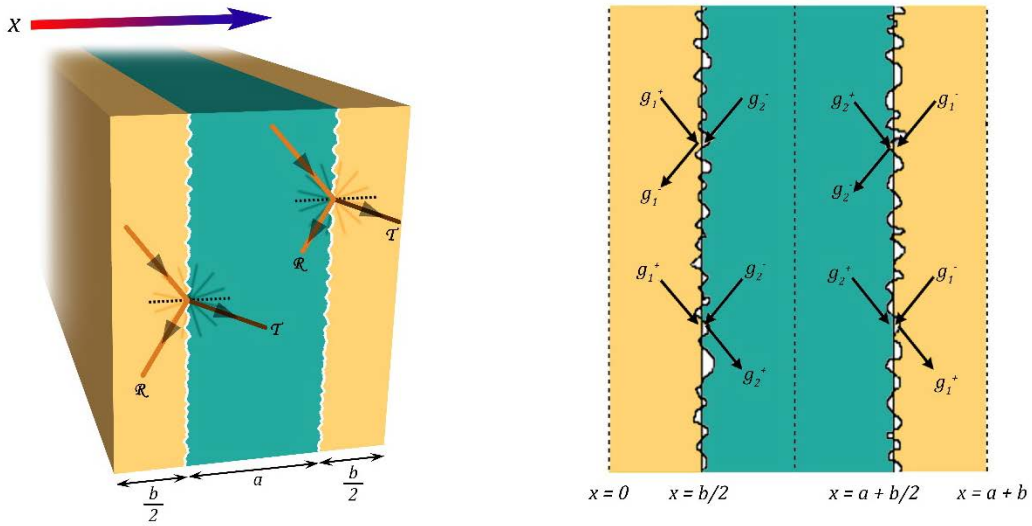

Figure 2. Schematic for cross-plane heat conduction in superlattices showing phonon reflection and transmission (left) and the detailed balance when phonons are scattered at the interfaces (right).

We examine thermal transport in superlattices in the cross-plane configuration i.e. the thermal gradient being perpendicular to the interfaces in the superlattice. Under steady-state and the application of a temperature gradient $\partial T/\partial x$ along the x-direction (i.e. cross-plane direction) and to linear-order approximation, the Boltzmann transport equation [31] for the deviation g of the phonon population distribution function f from the equilibrium distribution f^0 (i.e. $g = f - f^0$) can be written as

$$v_{\mathbf{k},p}^{x}\frac{\partial g_{\mathbf{k},p}}{\partial x}+\frac{g_{\mathbf{k},p}}{\tau_{\mathbf{k},p}}=-v_{\mathbf{k},p}^{x}\frac{\partial f_{\mathbf{k},p}^{0}}{\partial T}\frac{\partial T}{\partial x} \tag{24}$$

The thermal current can be separated in terms of phonons that move forward (described by g^+) and those moving backwards (described by g^-). The solution to the BTE for g^+ and g^- is obtained by applying periodic boundary conditions and establishing detailed balance conditions at the interfaces which rigorously incorporate the interlayer phonon coupling by accounting for interfacial characteristics, acoustic contrast of materials, as well as conservation of flux. Taking P_{ij} and Q_{ij} as reflection and transmission coefficients [Eqs. (12) – (13)] between media i and j, the detailed balance condition are given by

$$g_1^- = P_{12} g_1^+ + Q_{21} g_2^- \quad at \quad x = b/2 \tag{25}$$

$$g_2^+ = P_{21} g_2^- + Q_{12} g_1^+ \quad at \quad x = b/2 \tag{26}$$

$$g_2^- = P_{21} g_2^+ + Q_{12} g_1^- \quad at \quad x = a + b/2 \tag{27}$$

$$g_1^+ = P_{12} g_1^- + Q_{21} g_2^+ \quad at \quad x = a + b/2 \tag{28}$$

where 1 and 2 denote the different media across the interface. Once the deviation functions g^+ and g^- are obtained as a function of x within a given layer in the superlattice, we obtain the local thermal conductivity using Eq. 2. The thermal conductivity of each layer in the superlattice is obtained by integrating the thermal conductivity in the x-direction while considering flux conservation, which provides a first-order approximation to the position-dependent temperature gradient. To calculate the overall cross-plane thermal conductivity of the superlattice, we account for the interfacial resistance in terms of the thermal boundary resistance (TBR) [78] and obtain the overall thermal conductivity as follows,

$$\kappa_{Cross-plane} = \frac{t_1 + t_2}{\frac{t_1}{\kappa_1} + \frac{t_2}{\kappa_2} + TBR} \tag{29}$$

where t_i and κ_i (i = 1, 2) are the thicknesses and thermal conductivities of the two layers of the superlattice.

2.4.3 Phonon Injection Mechanism

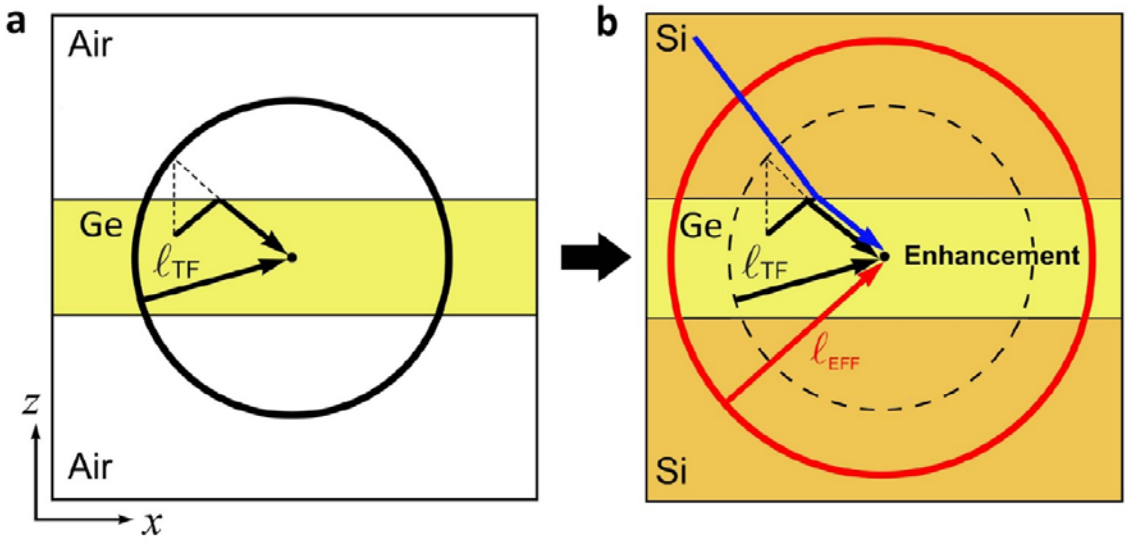

Figure 3. Phonon Injection. (a) Schematic for phonon contributions to the thermal conductivity of a germanium thin film under a temperature gradient along the x direction. The thermal flux at point O is carried by phonons whose last collision was, on the average, at a distance of mean free path ℓ_{TF} away from O, as represented by the black circular line. For simplicity we neglect the angular dependence of ℓ_{TF}. (b) When the germanium film is in contact with the silicon film, phonons from silicon can be injected into germanium (blue arrow). These phonons had their last collision at a larger distance than those arriving from germanium. As a result, the effective mean free path ℓ_{EFF} is larger (red circular line) and the thermal conductivity at point O is enhanced.

The transmission of phonons across an interface involving two different adjacent materials i.e. interfacial phononic coupling, leads to modulation of thermal properties of the materials involved. The thermal conductivity modulation in multilayered nanomaterials

depends on the efficiency of the phonon injection mechanism (Figure 3) which is governed by the thickness of layers involved as well as phonon interfacial coupling. When the layer thicknesses are smaller than phonon mean free paths, phonon interfacial exchange can significantly influence thermal properties of the different layers.

Phonon interactions at an interface involve a fraction of phonons undergoing specular transmission and reflection while the rest are diffusively scattered in all angular directions. In an unprecedented observation [107], we found that thermal conductivity of nanomembranes could be enhanced through utilization of nanostructuring and interfacial phonon coupling. This enhancement is an increment beyond the isolated thin-film thermal conductivity. This can be understood by realizing that thermal conductivity is a localized property in a nanostructure, i.e. conductivity at a point is determined by phonons reaching that point from an average distance equal to the mean free path of the phonons. Thus, any aberration within the mean free path distance from a point will alter the thermal conductivity of that point. When layered nanostructures involving multiple materials are fabricated, the interfacial coupling allows phonons from one material to be injected into another and contribute to the thermal transport of the other material. In a study involving Ge nanomembranes cladded by Si layers [107,108], we found that the phonon injection mechanism resulted in the thermal conductivity enhancement of the Ge nanomembranes since phonons originating in Si and terminating at a point inside Ge had travelled a larger distance (larger phonon group velocities and relaxation times) vis-à-vis phonons that only moved in Ge thin-film. Thus, we were able to conclude that nanostructuring need not necessarily lead to conductivity reduction, but can also provide avenues for enhancement when phonon coupling is involved.

The efficacy of the phonon injection mechanism is contingent upon the phonon interfacial coupling between the two materials and their thicknesses. Interfacial coupling has been studied by a variety of atomistic methods [45,46,48-50] which are unable to account for interfacial roughness and anharmonic phononic behavior in the nanostructures. Our formalism for interfacial coupling accounts for reflection and transmission while accounting for the phonon properties (frequency and incidence angle), acoustic properties of the adjacent materials (density, phonon group velocities) as well as interfacial structural characteristics (roughness and correlation length). Additionally, for elastic scattering at the interfaces, non-overlap of phonon dispersion relations leads to further resistance to the phonon injection mechanism. We provide illustrations of this distinction (Section 3.3) when considering phonon injection from the substrate into the thin-film for film-on-substrate architectures where we find that interlayer coupling between $Al_{0.1}Ga_{0.9}As$ and GaAs is larger than that in Ge and Si due to closer dispersion relations and acoustic properties [109].

2.4.4 Thin-Film on Substrate

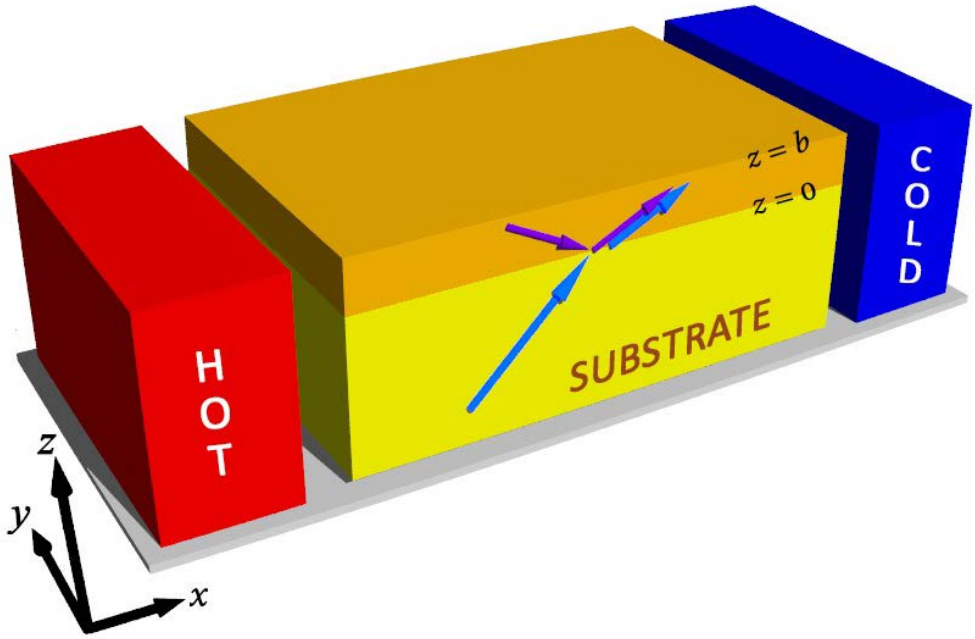

Figure 4. Schematic of a film-on-substrate (FOS) architecture where the film is shown in orange and the substrate in yellow. Arrows represent phonons originating at the film and the substrate and contributing to film phonon transport after reflection and transmission (interlayer coupling).

An important application of interfacial coupling and therein rooted, the phonon injection mechanism is the modulation of thermal conduction in nanomembranes that are grown atop a substrate. In order to investigate thin-film on substrate systems, we consider a baseline physical system consisting of a thin film of material A on top of a substrate of material B. Our choice of A and B is motivated from optoelectronic applications such as photodetectors where configurations based on Si, Ge, GaAs and AlGaAs semiconductors are found ubiquitously [90,110-112]. We focus on studying the thermal transport modulation in the thin film due to the presence of the substrate and not that of the entire nanostructure.

In the FOS architecture, we define η_o as the outer interfacial roughness at the interface between the thin film and air and η_i as the inner roughness between the thin film and the substrate. The detailed balance of energy across the interfaces requires a thorough treatment of interfacial scattering which provides the transmission and reflection properties [Eqs. (12) – (13)] in the FOS structure (Figure 4), which is given by

$$g_2^- = P_{21} g_2^+ + Q_{12} g_1^- \quad at\ z = 0 \tag{30}$$

$$g_1^+ = P_{12} g_1^- + Q_{12} g_2^+ \quad at\ z = 0 \tag{31}$$

$$g_1^- = P_{10} g_1^+ \quad at\ z = t \tag{32}$$

where P_{10} and P_{12} are the reflection coefficients for phonons at the film-air and film-substrate interfaces respectively, and Q_{12} is the transmission coefficient across the film-substrate interface. The thermal conductivity κ of the thin-film in the FOS architecture is calculated by considering a relatively thick substrate and applying Fourier's law Eq. (1) while averaging heat flux $J(z)$ over the film thickness t. Using the above mode-wise implementation of the BTE, we thus account for thermal transport in the FOS while rigorously accounting for interface phonon coupling and scattering.

CHAPTER 3.

ANALYSIS OF THERMAL TRANSPORT CHARACTERISTICS

We examine thermal conduction in layered semiconductor nanostructures by providing an accurate model for thermal conduction, specifically, a rigorous implementation of interlayer coupling through a detailed analysis of interfacial scattering. We utilize the principle of detailed balance of phonons along with specular transmission and reflection coefficients found from a statistical analysis to compute the amount of heat distributed amongst various layers of a nanostructure. We study how thermal transport is impacted by varying structural conditions such as characteristic length, interfacial roughness and volume fraction of constituents involved. We also move beyond thermal conductivity predictions to furnish an extensive comprehension of the thermal spectral analysis by detailing the frequency and mean free path spectra which provide crucial inputs in manipulating heat conduction and guiding rational thermal material design. We begin with investigating thermal transport in superlattices (Si/Ge and GaAs/AlAs based) in the in-plane and through-plane configurations. Thereafter, we investigate how interfacial coupling with other materials impacts thermal properties of a thin-film. Lastly, we also carry out a deeper analysis of interfacial coupling by studying the transmission coefficient, visualizing the impact of coupling on spatial distribution of thermal energy and carrying out a spectral analysis of coupling-induced conductivity modulation.

3.1 Si/Ge Superlattices – In-plane Configuration

Our goal is to move beyond calculation of thermal conductivity and to establish thermal energy distribution within superlattices. To achieve this goal, we first predict the amount of heat carried by extended and layer-restricted phonons and provide insights on the effects of periodicity, volume fraction and surface scattering. As we discuss in the next sections, extended and layer-restricted phonons constitute different heat conduction modes with distinct physical properties that can give rise to different wave-interference phonon effects on thermal energy transport. We thereafter predict thermal phonon spectra segregating the heat into extended and layer-restricted phonons. We also provide a comprehensive analysis of the dependence of thermal conductivity on temperature across various length scales.

3.1.1 Role of Periodicity on Thermal Energy Distribution

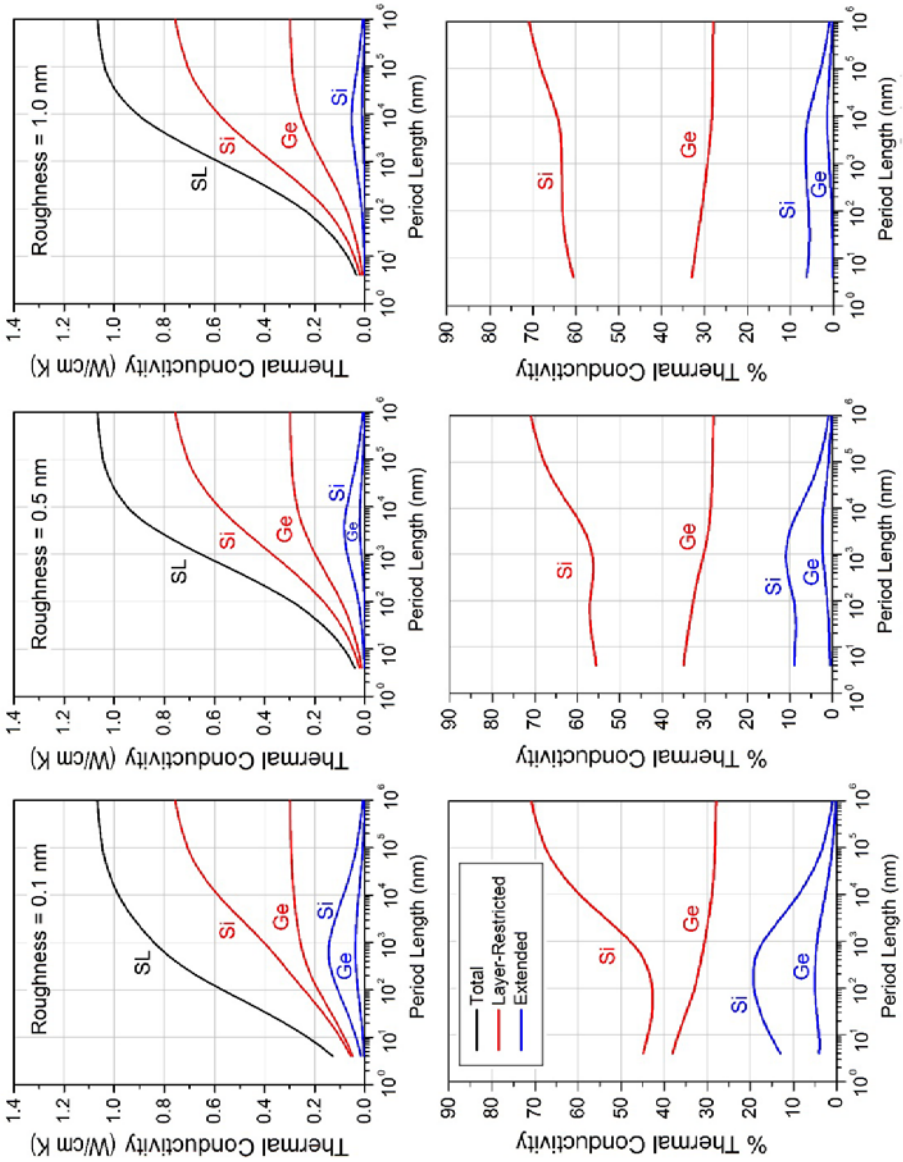

Figure 5. (a) Distribution of thermal energy carried by for layer-restricted phonons (red), extended phonons (blue), and total thermal conductivity (black) as a function of superlattice period length for surface roughness η =0.1 nm, 0.5 nm, and 1.0 nm. (b) Variation of percentage contribution of extended and layer-restricted phonons in Si and Ge to the total superlattice thermal conductivity.

We show in Figure 5 the effects of superlattice period on the thermal conductivity and energy distributions for Si/Ge superlattices under different interface conditions at room temperature. The different contributions to thermal conductivity arising from extended (e-Si, e-Ge) and layer-restricted (r-Si, r-Ge) phonons are shown separately with blue and red lines respectively while black lines show the total in-plane superlattice thermal conductivity κ_{SL}. Note that e-Si refers to phonons that are extended and originating in Si, while e-Ge refers to extended phonons originating in Ge. Bulk phonon mean-free-paths and dispersion relations for Si and Ge are taken from existing values in the literature [12,113-115]. We observe that κ_{SL} decreases as the period length decreases, which is attributed to increased phonon interface scattering due to an increased interface density and the absence of wave effects (see CHAPTER 4). Figure 5a quantitatively show how κ_{SL} varies with period for different surface roughnesses (η =0.1, 0.5, and 1 nm) at the interfaces. While κ_{SL} is significantly reduced for larger η values at small length scales, for large periods κ_{SL} saturates to the bulk value $\kappa_{SL} = 0.5(\kappa_{bulk-Si} + \kappa_{bulk-Ge}) = 0.5(1.56 + 0.60) = 1.08$ W/cm.K independently of the surface condition. This trend confirms to the physical concept that at large periods, superlattices behave as bulk multilayers and κ_{SL} does not depend on interface features. We found in Figure 5a that, with increasing period, the contribution of extended phonons (i.e. those moving across different layers) undergoes a maximum and then vanishes asymptotically. The increase in contribution is due to the reduced interface density as the period increases, whereas the decline is due to the fact that as period lengths approach bulk values, the number of incident phonons on the interfaces reduces since phonon MFPs become much smaller than the layer thicknesses. That is, due to the limited extent of the bulk phonon

mean-free-paths there are no extended phonons for large superlattice periods. Contrarily, the contribution of layer-restricted phonons (i.e. those moving in a single layer) increases monotonically with increasing period lengths and, similarly to κ_{SL}, reach the bulk values $0.5\kappa_{bulk-Si}$ and $0.5\kappa_{bulk-Ge}$ for large periods. This is consistent since at large periods phonons do not see the interfaces and move within a single layer while carrying the heat. In Figure 5b, we also analyze the relative contributions of the components of conductivity, i.e. their percentage contribution to the total conductivity, as a function of the period length and for different surface conditions. We found that with increasing period length, the relative contribution of phonons restricted to Si shows a minimum (correlated to the maximum in e-Si) while that of those restricted to Ge decreases. The relative contributions of phonons extended across layers also exhibit maxima before tending to negligible amounts at large period lengths. The contribution of different phonon transport modes to the thermal conductivity is dependent on the superlattice period and surface conditions and, in particular, we found that there exist a specific period for which the amount of heat carried by extended phonons is maximized.

3.1.2 Influence of Superlattice Volume Fraction

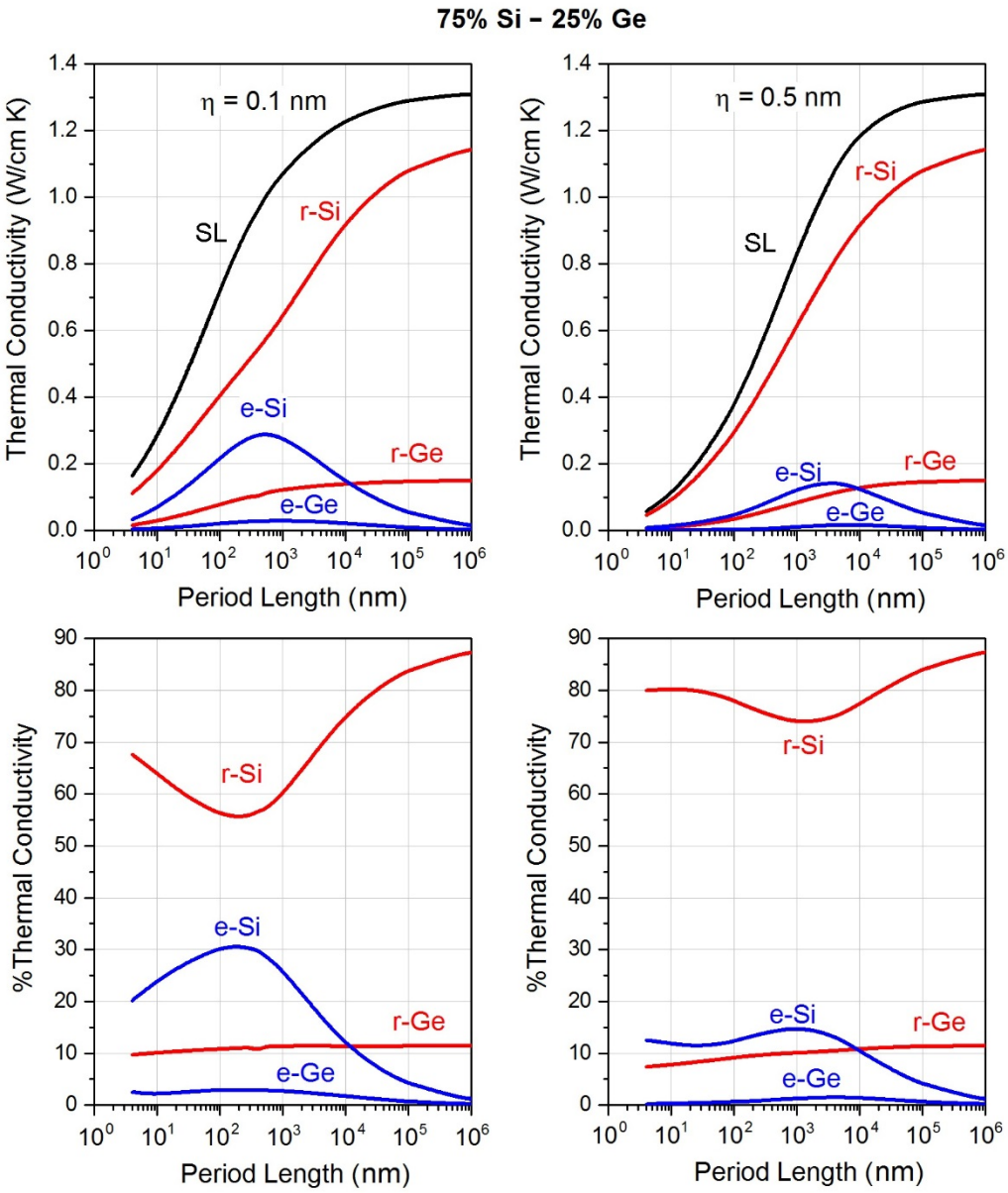

Figure 6. (a) Variation of thermal conductivity of layer-restricted and extended phonons as a function of period length for Si/Ge superlattices having volume fraction of f_{Si} = 0.75, with roughness values of 0.1 nm and 0.5 nm. (b) Relative contribution of extended and layer-restricted phonons in the corresponding superlattices.

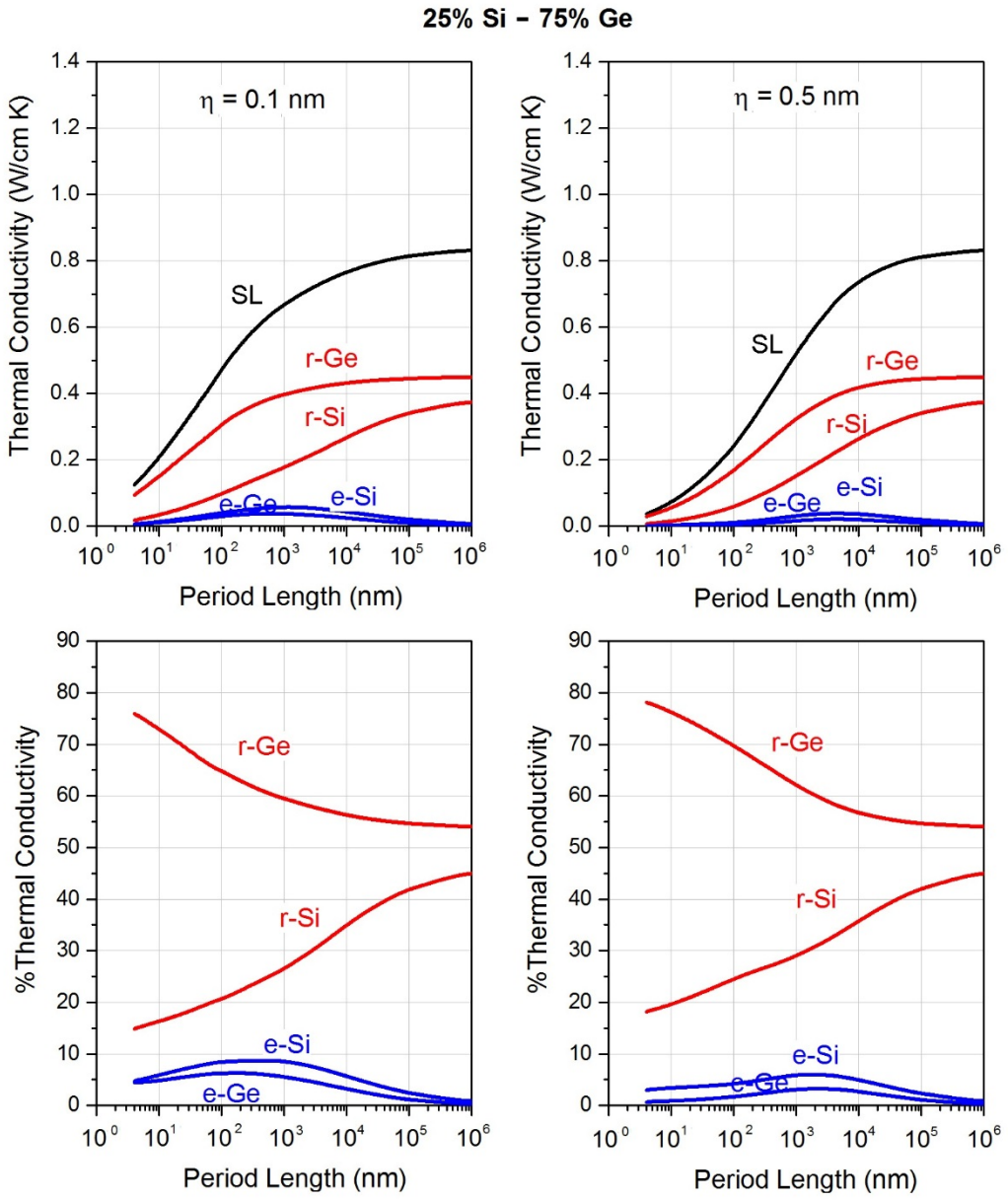

Figure 7. (a) Variation of thermal conductivities with period length for Si/Ge SLs, having volume fraction of f_{Si} = 0.25, with surface roughness η = 0.1 nm and η = 0.5 nm. (b) Relative contribution of extended and layer-restricted phonons.

Next, we investigate the phonon energy distributions within the superlattices as a function of the volume fraction f of the constituent materials. We consider two vastly different SiGe superlattice conditions by choosing f_{Si}=0.75 and f_{Si}=0.25 and show in Figure 6 and Figure 7 the variation of the thermal conductivity with period for different surface

conditions. For a fixed period length, decreasing f_{Si} decreases the thermal conductivity κ_{SL}, which is analogous to the bulk case, since $\kappa_{bulk-Si} > \kappa_{bulk-Ge}$. For f_{Si}=0.75 (Figure 6), the contribution to conductivity of phonons restricted to Si is increased with respect to f_{Si}=0.50 due to its higher volume fraction. Note that the contribution of extended phonons originating from Si and the maximum is also more pronounced than f_{Si}=0.50 and for period lengths $d<10^4$ nm the contribution is larger than that of those restricted in Ge. For larger periods, however, a reversed behavior is observed due to the zero-limit contribution of extended phonons at large periods. In terms of relative contributions, phonons restricted to Si still exhibits a minima with increasing period length (Figure 6b) which is in agreement with the trend found for f_{Si}=0.50. The relative contributions of layer-restricted phonons in Ge are weakly dependent on the period length. On the other hand, a maximum is still found in the relative contribution of extended phonons from Si and Ge. For f_{Si}=0.25 (Figure 7), we observe that the contribution to conductivity of layer-restricted phonons in Ge is the largest (due to the large Ge volume fraction) followed by that of phonons restricted to Si and thereafter that of extended phonons originating from Si and Ge. This feature is maintained across all period length scales. In terms of relative contributions, the relative contribution of phonons restricted to Ge decreases while that of phonons restricted to Si increases with increasing period. Importantly, by comparing Figure 5- Figure 7, we found that reducing the volume fraction of Si does not alter the existence of a maximum for extended phonons but the amount of heat carried by these phonons is significantly reduced. Note that all the aforementioned maxima and minima for the distribution of thermal energy are more pronounced in the case of small interface roughness as reduced interface

scattering allows for larger mean free paths and thus a larger proportion of extended phonons.

3.1.3 Impact of Interface Roughness

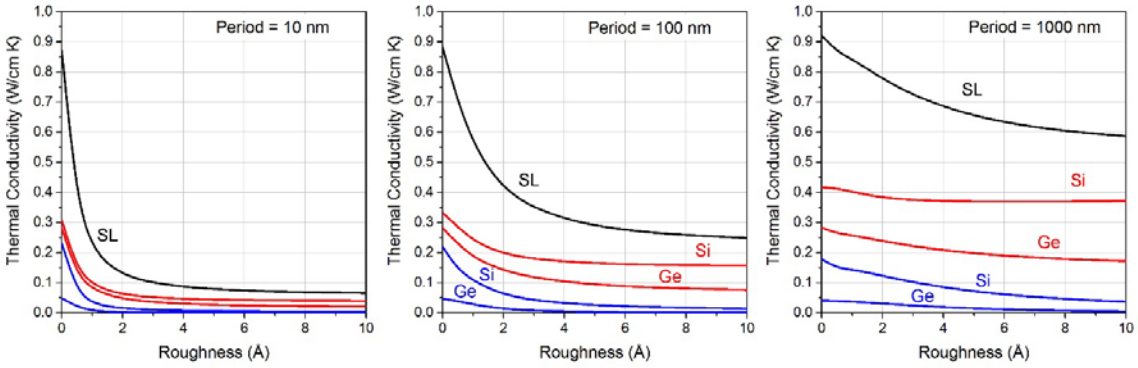

Figure 8. Effects of interface roughness on the amount of heat carried by layer-restricted and extended phonons in superlattices with periods d=10nm, 100 nm, and 1000 nm. Black, red and blue curves represent total, layer-restricted and extended components of conductivity respectively.

Since interface conditions are a critical aspect for superlattice thermal transport, we investigate in detail the variation of energy distribution and thermal conductivity with respect to surface roughness in superlattices f_{Si}= f_{Ge}=0.50. Figure 8 shows κ_{SL} when the interface roughness is varied from η = 0 nm to 1 nm. We quantitatively show how κ_{SL} reduces and converges to a constant value as the roughness increases. This behavior is observed in restricted and extended components of the conductivity and across different period lengths. This is attributed to the fact that as we increase interface roughness, the fraction of phonons that are specularly scattered diminishes asymptotically. Very rough surfaces lead to complete diffusive scattering and that gives the lowest value of conductivity for a specific period length. On the other hand, we observe that κ_{SL} increases at η = 0. This is due to the absence of diffuse interface scattering in the superlattice. In this

case, it is only the impedance mismatch which modulates the amount of heat carried in different constituent elements. Since impedance mismatch is non-vanishing in Si/Ge SLs, we note that κ_{SL} does not tend to bulk values at $\eta = 0$ in the quasi-ballistic regime.

From the previous discussions, it is clear that the amount of thermal energy carried by layer-restricted and extended phonons can be tailored by manipulating the structural features of the superlattice such as period, volume fraction, and surface roughness. This means that it is possible to rationally design superlattices with maximal or minimal proportions of heat carried by extended or layer-restricted phonons. These different heat transport processes can give rise to different physical properties and wave effects as we discuss in CHAPTER 4.

3.1.4 Heat Frequency Spectrum in Superlattices

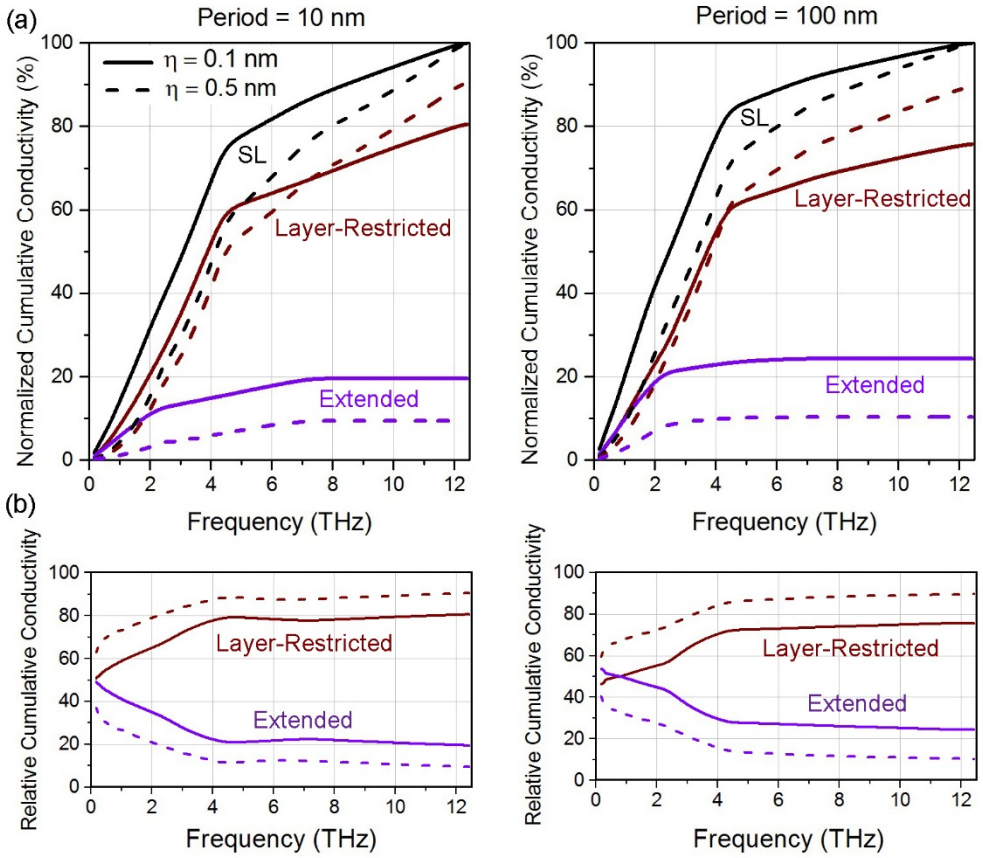

Figure 9. (a) Frequency spectrum for Si/Ge SL of period lengths d = 10 nm and d = 100 nm at roughness values of η = 0.1 nm and η = 0.5 nm (solid and dashed curves respectively). (b) Relative cumulative contribution of extended and layer-restricted phonons (purple and brown respectively) as a function of frequency in the corresponding SLs.

One important aspect in nanoscale heat transport is the establishment of the amount of heat carried by phonons with different frequencies. The prediction of the heat frequency spectrum allows to determine whether heat is carried by low, middle, or high frequency phonons, which can be utilized to rationally design thermal materials and devices [35,116,117]. Next, we study the heat frequency spectrum in Si/Ge superlattices. Figure 9 shows the normalized cumulative conductivity and relative cumulative conductivity at room temperature as a function of frequency for period lengths d =10 nm and 100 nm, and f_{Si}= f_{Ge}=0.5. Two different surface roughnesses were considered for both superlattices, η =

0.1 nm and 0.5 nm. Note that when the period decreases, the proportion of heat carried by high frequency phonons increases. For instance, for d =10 nm, η = 0.1 nm, approximately 50% of the heat is carried by phonons with frequencies less than 3 THz, while this proportion is increased to 60% for d =100 nm. This is due to reduced phonon scattering at the boundaries (due to lower interface density) in longer period length superlattices, which allows for larger mean-free-paths. Thus, a lower frequency phonon can carry more heat in a longer period superlattice. Figure 9a also quantitatively establishes the shift in the frequency spectrum with change in interface roughness. We note that with increase in roughness, the total superlattice conductivity spectrum shifts towards the right i.e. higher frequencies (or blue shift). This suggests that increase in interface roughness scatters lower frequencies more significantly (due to larger MFPs), thus higher frequencies carry more heat. The kink around 5 THz is due to the existence of only longitudinal modes at high frequencies. In Figure 9b, we present the relative cumulative conductivity as a function of phonon frequency. The plots indicate the fraction of heat carried by layer-restricted and extended phonons up to a certain frequency for different periods and surfaces roughnesses. For example, at d =100 and η = 0.5 nm, approximately 65% of the heat conduction is layer-restricted and the remaining ~35% is extended for phonons up to 3 THz in frequency. Figure 9b shows that with increasing interface roughness the fraction of heat that is layer-restricted is increased. This is consistent with the limiting case of fully diffuse interfaces wherein there will be no thermal conductivity contribution of extended modes and all heat will be layer-restricted. This observation provides a mechanism that can be utilized to control the proportion of thermal conductivity which is layer-restricted and extended by manipulating the roughness. We provide further verification of this trend in the next

section. We also note that as frequency increases more phonons tend to be restricted. This is attributed to the larger mean-free-paths of low-frequency phonons which allow them to reach the interfaces to a larger extent. Also, low-frequency phonons have large wavelengths and are more specularly reflected at the interfaces, enabling transmission across different layers.

3.1.5 Phonon Mean-Free-Path Spectrum

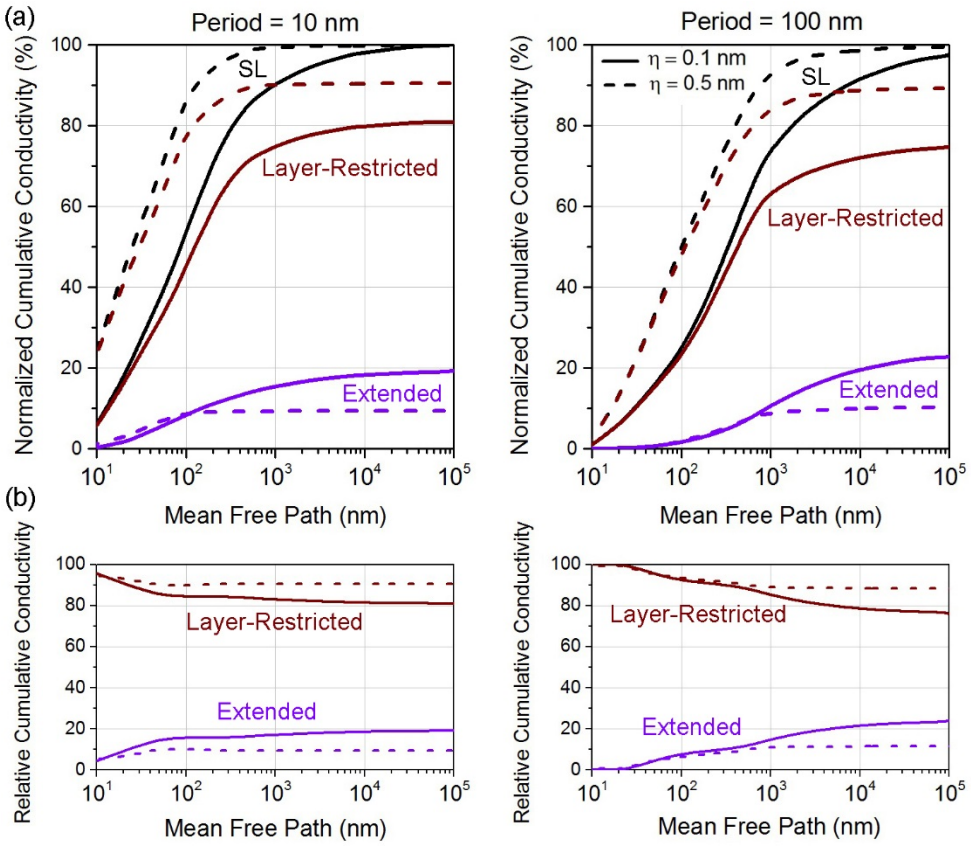

Figure 10. (a) Mean-free-path spectrum for Si/Ge SL of period lengths *d* = 10 nm and 100 nm at roughness values of 0.1 nm and 0.5 nm (solid and dashed curves respectively). (b) Relative cumulative contribution of extended and layer-restricted phonons (purple and brown respectively) as a function of mean-free-path in the corresponding SLs.

In addition to the frequency spectrum, a critical thermal transport property is the phonon mean-free-path spectrum, which allows to determine how far phonons move while carrying heat. In superlattices, the reduced phonon MFPs in each layer *i* depend on the *z*-coordinate of the point where the phonon originates and the wavevector $\vec{k}$, and are given by the solutions of the BTE by dropping the factor $\partial f_i^0 / \partial x$ from Eq. 16. We consider superlattices of period lengths 100 nm and 10 nm and surface roughness of 0.1nm and 0.5nm (f_{Si}= f_{Ge}=0.50). Figure 10a gives the normalized cumulative conductivity at room temperature as a function of the MFP. The normalized cumulative conductivity tends to saturate starting at MFPs approximately 1 μm for period d =10nm. This implies that phonons having MFP larger than the saturation MFP do not carry significant portion of heat. We note that for all the components of conductivity, the saturation MFP shifts to higher values as the period length increases to d =100 nm i.e. the curves shift to the right. This is consistent, since a shorter period length would imply shorter MFPs due to higher influence of boundary scattering. We observe that, in agreement with the frequency spectrum, more heat is layer-restricted than extended between the layers. This is due to the following reasons – (1) high frequency phonons of Si having frequency higher than the maximum frequency allowed in Ge (for either polarization – longitudinal or transverse) carry significant amount of heat and (2) phonons that are restricted in Ge via total internal reflection (due to the large acoustic impedance between Si and Ge) also carry substantial heat. Also, in agreement with the previous section, we observe that with increasing roughness, a larger fraction of heat conduction is restricted to a layer.

3.1.6 Temperature Dependence and Comparison with Experiments

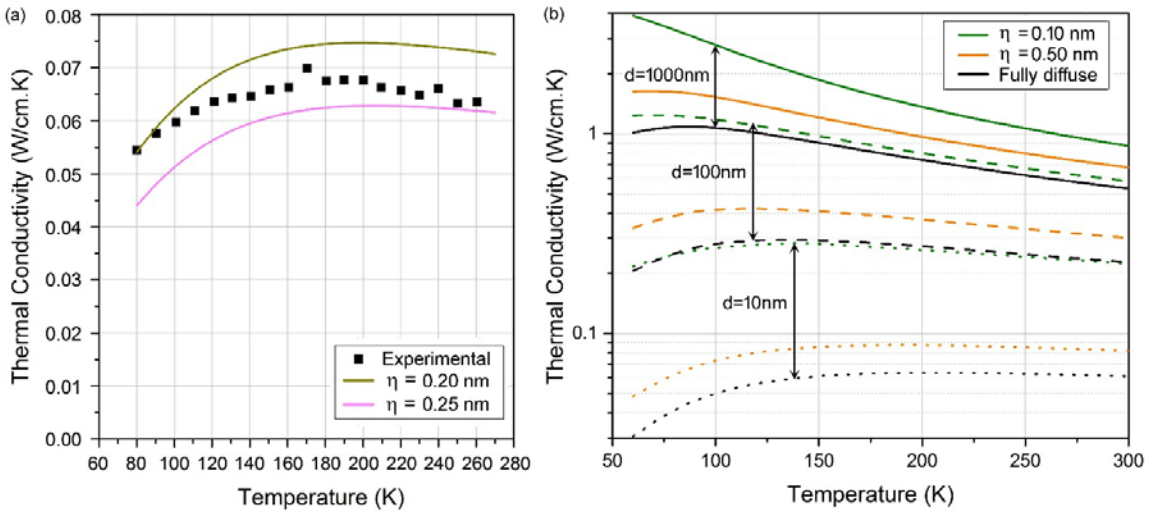

Figure 11. (a) Comparison between the theoretical predictions and experimental data for a 50-50 Si-Ge SL of period length 4 nm. (b) Temperature variation of thermal conductivity for Si-Ge SL of periods length *d* = 10 nm, 100 nm, and 1000 nm (dotted, dashed and solid curves respectively) at roughness values η = 0.1 nm, η = 0.5 nm and fully diffuse scattering (green, orange and black curves respectively).

Figure 11a shows the comparison between theoretical predictions and experimental measurements of superlattice thermal conductivity as a function of temperature. We note that measurements of in-plane thermal conductivity of SiGe superlattices in the literature are scarce. The theoretical (solid lines) and experimental (symbols) plots show the temperature variation of in-plane thermal conductivity in a Si/Ge superlattice with period d=4 nm and f_{Si}= f_{Ge}=0.50. We observe that κ_{SL} initially increases with increase in temperature, reaches a maximum and then shows a weak dependence with increase in temperature. The observed reduction of κ_{SL} at low temperatures is a result of decreasing phonon occupation as the temperature is reduced. At higher temperatures, phonon occupation does not change significantly, and the weak dependence of κ_{SL} on temperature is a consequence of the dominance of interface scattering over phonon-phonon scattering due to the small superlattice period. We see that our predictions can explain the trends by

providing a match with the experimental data [84]. In addition, Figure 11a shows the sensitivity of κ_{SL} with respect to surface roughness where a small decrease in η leads to a slight increase in κ_{SL}. We provide in Figure 11b the dependence of κ_{SL} on temperature for a vast range of structural features, where periods are increased by orders of magnitude from d = 10nm to d = 1μm, and three surface roughness conditions η = 0.1 nm, η = 0.5 nm, and fully diffusive interfaces are considered. Note that at high temperatures (>100K), with increasing period length, there is a reduction of thermal conductivity with temperature due to phonon-phonon scattering, in contrast to a nearly constant dependence for small periods due to the dominance of phonon-surface scattering.

3.2 GaAs/AlAs Superlattice – In-plane Configuration

In this section, we use an approach analogous to that employed for Si/Ge superlattices, to model thermal phonon interface scattering accounting for roughness, correlation length, and interlayer coupling and apply it to elucidate in-plane thermal transport mechanisms in III-V compound semiconductor superlattices. Along with providing predictions of the impact of varying structural parameters on thermal conductivity, we present a systematic description of thermal spectra in terms of frequency and mean free paths of phonons. We perform an extensive microscopic analysis detailing various interfacial interaction mechanisms in GaAs/AlAs superlattices and segregating thermal conductivity contributions of phonons with respect to the different physical mechanisms determining their trajectory**.** We investigate these contributions through predictions of the quantity of heat retained by phonons after N transmissions and reflections at interfaces while moving through the superlattice structure. We employ the analysis to

investigate thermal conduction in optoelectronic applications such as QCLs and Quantum Well Infrared Photodetectors (QWIPs) and determine thermal conductivity variation with well and barrier widths. We also compute the conductivity for realistic finite-sized superlattices used in these devices. Our results provide key inputs for thermal control in III-V semiconductor superlattice-based optoelectronic devices which is crucial for achieving an optimum performance.

3.2.1 Effect of Structural Properties

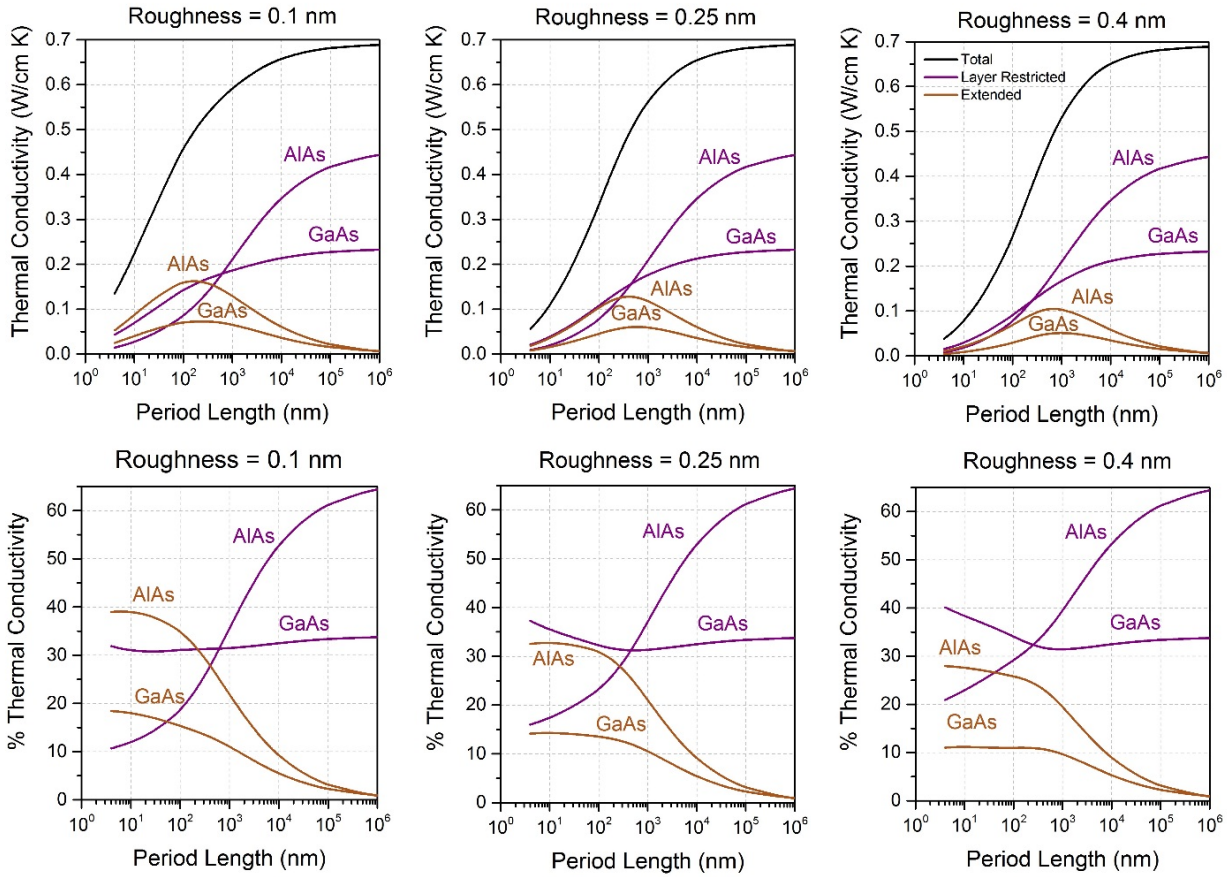

Figure 12. (a) Thermal conductivity and (b) Relative thermal conduction in GaAs/AlAs superlattices as a function of period length for varying interfacial roughness η = 0.10 nm, 0.25 nm and 0.40 nm at *T* = 300 K. The total, layer-restricted, and extended phonon thermal transport is depicted by black, purple and brown lines respectively.

In Figure 12a, we examine the effect of period length variation on thermal conductivity in GaAs/AlAs superlattices and illustrate the thermal energy distribution (i.e. the decomposition of thermal conduction into "layer-restricted" and "extended" phonons) for various interface roughness conditions. We observe an increase in the overall thermal conductivity with increasing period length due to decreasing interface density. We note that for strong interlayer coupling (small interface roughness and period lengths < 50 nm) the extended phonons in GaAs and AlAs have a larger contribution than layer-restricted phonons. This is in sharp contrast to Si/Ge superlattices where layer-restricted phonons are the major contributors to thermal conductivity irrespective of period length and roughness [118]. This is due to the lower impedance mismatch between GaAs and AlAs as compared to Si and Ge arising from similar lattice constants, dispersion relations, and physical properties of GaAs and AlAs. We see that for large interface roughness, this behavior ceases and the contribution of layer-restricted phonons becomes dominant. We observe that the thermal conductivity contribution of extended phonons exhibits a maxima with increasing period length due to a trade-off between reduction in interface density and finite thermal phonon MFPs. Thus, for large values of period length, thermal conductivity contribution of extended phonons asymptotically tends to a negligible value. In Figure 12a, we also provide the quantitative prediction of the thermal conductivity variation with interface roughness, where we show how, with increasing interface roughness, the thermal conductivity of superlattices reduces due to incremental diffusive scattering of phonons. For calculations, bulk dispersion relations and phonon mean-free-paths data for GaAs and AlAs and their alloys are taken from existing values in the literature [79,119-122]. The bulk mean-free-paths $l_{0j}(\vec{k}) = v(\vec{k})\tau_{0j}(\vec{k})$, where $\tau_{0j}(\vec{k})$ is the relaxation time, are

calculated by considering scattering by phonons. By separately considering isotropic longitudinal (LA) and transverse (TA) acoustic polarizations, we obtain the phonon-phonon relaxation times for GaAs and AlAs by comparing Boltzmann calculations to the experimental bulk thermal conductivity [12]. We note that our phonon-phonon relaxation times show reasonable good agreement across the entire frequency spectrum with those calculated from first-principles [123] and similar approaches [79]. Optical modes are neglected, as owing to their low group velocities and high scattering rates their contribution to thermal conductivity is low [31]. For room temperature, we consider thermal transport being incoherent in GaAs/AlAs superlattices (see last paragraph) [63]. In Figure 12b, we analyzed the relative thermal conductivity contributions of distinct phonon components. The relative contribution of layer-restricted phonons in AlAs increases monotonically while that in GaAs shows a slight minima with period length. We remark that the relative contribution of extended phonons largely shows a monotonic decrease thereby indicating that although thermal conduction by extended phonons is maximum at specific period length (> 100 nm), maximum proportion of extended heat conduction exists for very short period lengths.

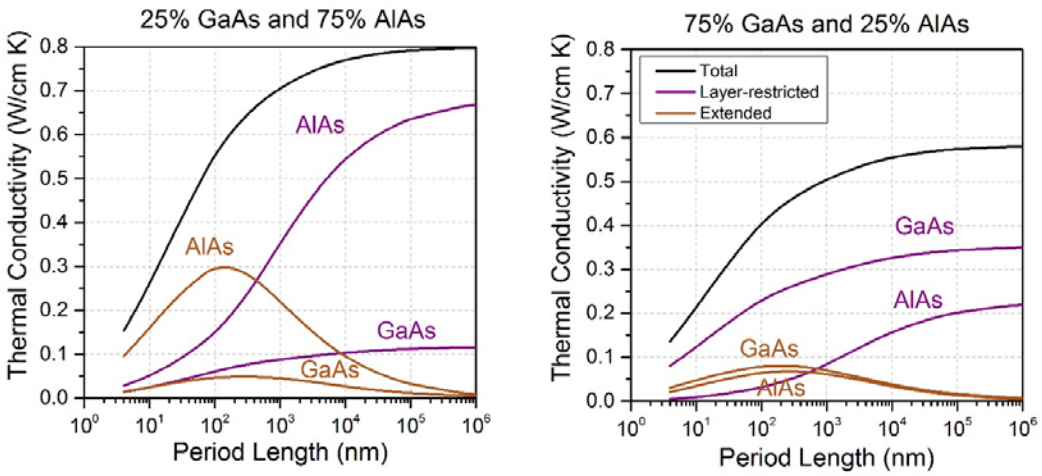

Figure 13. Thermal conductivity of GaAs/AlAs superlattices with interface roughness η = 0.10 nm for two different volume fractions f_{GaAs} = 0.25 and f_{GaAs} = 0.75 where the total, layer-restricted, and extended phonon thermal transport is depicted by black, purple and brown lines respectively.

We next study the variation of thermal energy distribution with volume fraction. In Figure 13, we have considered two vastly different volume fractions of the constituents, f_{GaAs} = 0.25 and f_{GaAs} = 0.75. We show how the thermal conductivity of GaAs-AlAs superlattices decreases with decreasing volume fraction of AlAs. This is consistent since bulk conductivity of AlAs is larger than that for GaAs. We remark that, for large values of period length the thermal conductivity of the superlattice tends to the weighted average of the bulk conductivities of GaAs and AlAs, thus in alignment with the notion that surface characteristics do not have a significant impact at the macro scale. This agrees with our previous discussion since at large period lengths, phonons do not see the interfaces and are constrained to move within a single layer. We also note that, in Figure 13, extended phonons exhibit a maximum with increasing period length, but their contribution to thermal conductivity significantly reduces with decreasing volume fraction of AlAs.

3.2.2 Microscopic Thermal Analysis

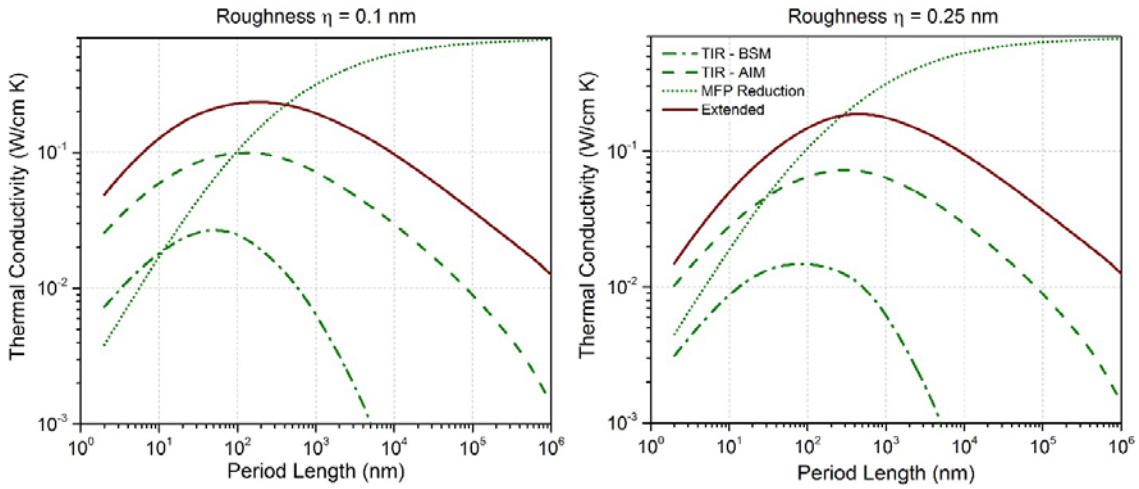

Figure 14. Thermal energy distribution in GaAs/AlAs superlattices showing thermal conduction by different interfacial interaction mechanisms of thermal phonons. The extended phonon conductivity is denoted by the solid brown line while the TIR-BSM, TIR-AIM and MFP reduced (components of layer-restricted phonons) are denoted by the green dash-dotted, dashed and dotted lines respectively.

After quantifying the impact of periodicity, volume fraction, and interface roughness on thermal transport in GaAs/AlAs superlattices, we next consider a thermal analysis at a microscopic level and distinguish the different mechanisms which constrain phonons within a specific material layer and evaluate the thermal conduction through each mechanism. There exist three possible physical mechanisms which cause layer-restricted phonons i.e. phonons constrained to move within a layer (Figure 1) – (1) total internal reflection by acoustic impedance mismatch (TIR-AIM), in which phonons are constrained to a layer because the phonon incidence angle exceeds the critical angle at the interface due to an acoustic impedance mismatch between two materials, (2) total internal reflection by band structure mismatch (TIR-BSM), in which phonons of a particular frequency are unable to transmit into the adjacent layer and thus remain in a single layer because that frequency is not available in the dispersion relation of the adjacent material and (3) MFP reduction, in which phonons are unable to reach the interface due to diffused scattering

thus remain constrained within a layer. In Figure 14, we show the distribution of thermal conduction in superlattices into four different components depending on the trajectory and physical mechanisms encountered by phonons. We present the thermal conductivity contributions of phonons subject to TIR-BSM (green dash-dotted curve), TIR-AIM (green dashed curve), MFP reduction (green dotted curve) and extended (brown solid curve) phonons as a function of period length. Note that our mode-wise implementation of the BTE (Methodology Section) takes into consideration wavevector directions, frequencies, angles, point of origin, mean free paths, and phonon coupling between materials (i.e. reflection and transmission) allowing to separate phonons having different physical properties (e.g. phonons that transmit or internally reflect at the interfaces). This detailed description of phonon transport enables to decompose the total thermal conductivity into various parts based on the trajectory and physical mechanisms behind phonon transport (i.e. extended or layer restricted, TIR-AIM, TIR-BSM, and MFP). At larger period lengths, all phonons are MFP layer-restricted due to finite MFPs. That is, TIR and extended components of conductivity tend to negligible values while the reduced-MFP component tends to the mean of the bulk conductivities of GaAs and AlAs. We observe that, irrespective of period length and roughness, the contribution of the extended phonons is larger than contribution of phonons subject to TIR-AIM or TIR-BSM. This behavior is unique to the component materials of the superlattice and is attributed to similar dispersion relations and low acoustic impedance mismatch between GaAs and AlAs. We notice that, with increase in roughness, the maxima for TIR and extended components of conductivity are lowered (indicative of the overall reduction in conductivity) and shifted to a larger period length value. This is because, superlattices of smaller period length undergo larger

MFP reduction (in contrast with superlattices of larger period length). The segregation of thermal transport into these four components allows for a thorough understanding of the movement of heat within superlattices.

3.2.3 Interaction with Multiple Interfaces

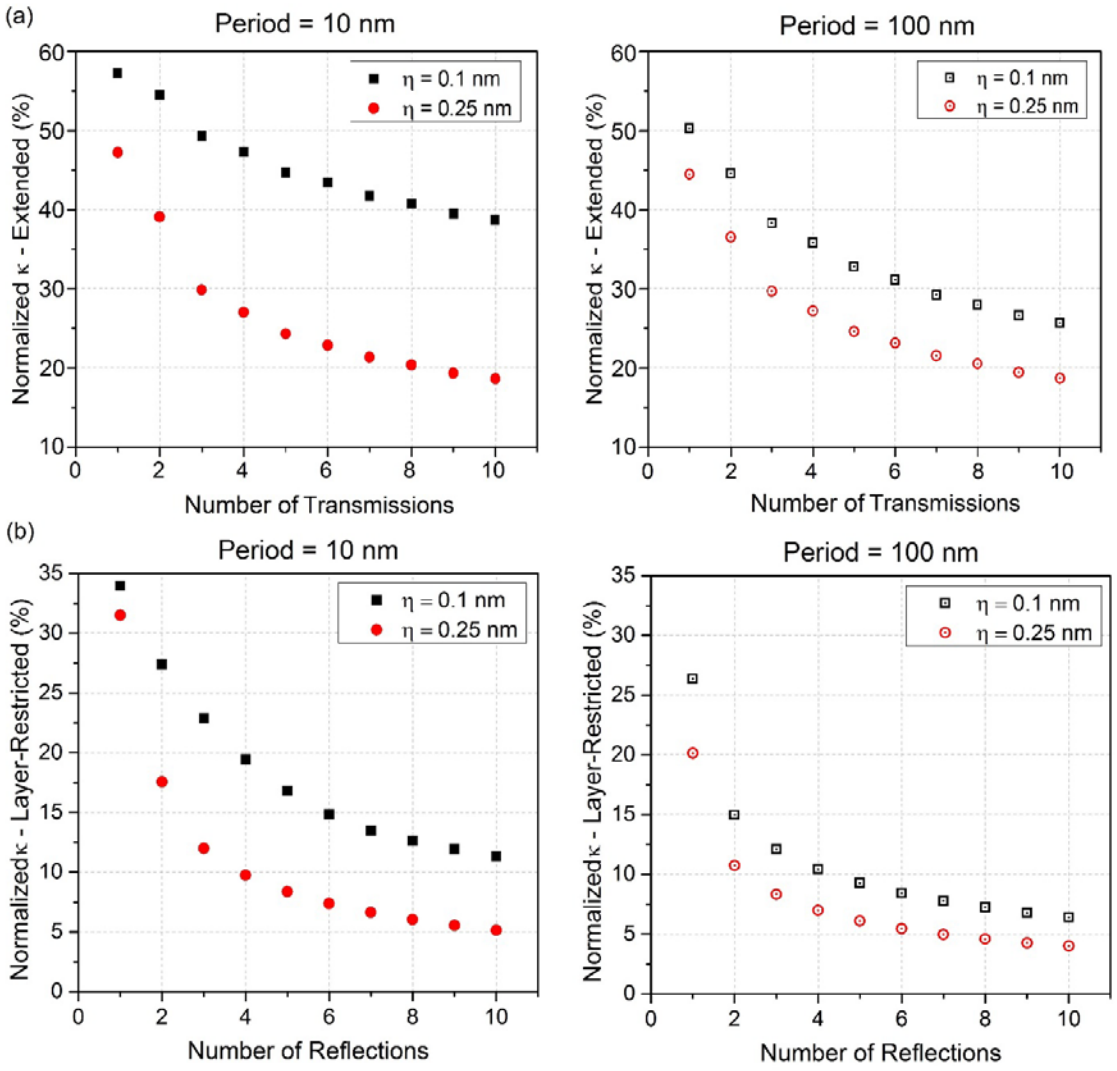

Figure 15. (a) and (b) Normalized thermal conductivity transmitted across interfaces (extended phonons) as a function of number of transmissions and (c) and (d) transmitted within a layer after 'N' number of reflections (layer-restricted phonons) in a GaAs/AlAs superlattice of period length 10 nm and 100 nm respectively.

Along with understanding of segregation of thermal conduction into various phonon trajectories, it is also essential to quantify how much heat can be transmitted across several interfaces upon scattering. This knowledge plays a key role in determining the probability of wave effects such as phonon coherent interference (i.e. dispersion relation modification owing to multiple reflections and transmissions of phonons at interfaces [63]) and quantum confinement (i.e. dispersion modification owing to multiple reflection of phonons within a single layer [124]) in superlattices. Phonon interference effects caused by interference of phonons with their reflections from superlattice interfaces [63] require that a sufficiently large proportion of heat is transmitted across multiple interfaces. The observation of quantum confinement effects is governed by coherent interference of multiple reflections of layer-restricted phonons [102]. In this section we provide the percentage of total thermal conductivity that is transmitted across interfaces as a function of the number of interfaces (for extended phonons) and that which is retained within a layer after multiple reflections from its boundaries (for AIM and BSM components of layer-restricted phonons). In Figure 15a and Figure 15b, we present the proportion of thermal conductivity retained by phonons upon 'N' transmission and reflection events in GaAs-AlAs superlattices, respectively. We perform this analysis for different values of period length and roughness. We note that the amount of heat transmitted across interfaces and reflected from surfaces reduces with increasing roughness. In Figure 15a, we observe that a significant proportion (~40%) of the total thermal conduction is retained after scattering from 10 interfaces in a 10 nm period length superlattice with roughness η = 0.10 nm, and decreases to 20% as the roughness increases to η = 0.25 nm. An interesting observation is that the proportion of heat transmitting across interfaces decreases as we increase the period

length from 10 nm to 100 nm. For smooth surfaces (η = 0.10 nm), it is clear that the larger the distance between the surfaces, the smaller the heat transmitted across the interfaces. However for rough surfaces (η = 0.25 nm), as the distance between the surfaces is increased, mean free paths are also increased, and the heat transmitted is weakly varying with period length due to a balance between these two effects as shown in Figure 15a. We evaluated in Figure 15b the fraction of heat retained upon 'N' reflections from surfaces for phonons that are layer-restricted (by AIM and BSM mechanisms) in terms of the normalized cumulative conductivity. A component-wise analysis reveals that TIR-AIM is the dominant mechanism contributing to layer-restriction of heat after multiple phonon 'bounces' within a layer. Due to comparable dispersion relations for GaAs and AlAs, available frequencies exist for transmission in the adjoining media which leads to lower TIR-BSM. Furthermore, phonons of all frequency ranges can be confined by TIR-AIM while those layer-restricted due to TIR-BSM are only high frequency phonons, and the latter are more diffusively scattered upon reflection at rough interfaces. From this analysis, we can predict how, for GaAs-AlAs superlattices, small period length and small interface roughness lead to a higher proportion of heat being carried after 'N' bounces.

3.2.4 Thermal Spectrum for Superlattices

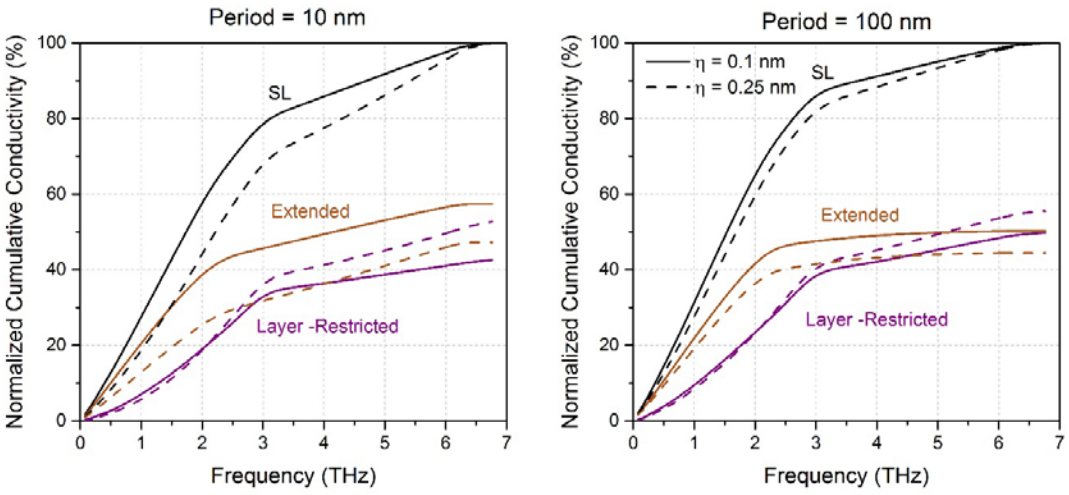

Figure 16. Frequency spectrum for GaAs/AlAs superlattices of period length (a) 10 nm and (b) 100 nm at room temperature at interfacial roughness values η = 0.1 nm (solid lines) and η = 0.25 nm (dashed lines). The total, layer-restricted and extended phonons' thermal transport contributions are depicted by black, purple and brown lines respectively.

Another important aspect of nanoscale heat transport lies in the analysis of the quantity of heat carried by phonons of varying frequency and MFP length. This is essential to designing superlattices for applications where thermal conduction manipulation of certain physical properties such as long MFPs or small frequencies can increase the probability of scattering by additional centers such as nanoparticles. In this section, we quantify the heat carried by phonons across various frequencies and MFPs through frequency and MFP spectra of GaAs-AlAs superlattices in terms of their normalized cumulative conductivities. In Figure 16, we show the thermal phonon frequency spectra in GaAs-AlAs superlattices with period length values of 10 nm and 100 nm and interface roughness of η = 0.10 nm and 0.25 nm. We note that, with increasing period length, a larger proportion of the heat is carried by lower frequency phonons, since reduced interface density allows for longer MFPs. We also observe a blue shift in the frequency with increasing roughness i.e. a rightward shift in the frequency spectrum. This is because with

increasing roughness, the effect of diffuse scattering on low-frequency phonons is larger than that for high-frequency phonons. The kinks observed in the frequency spectra correspond to the ends of the dispersion relations for transverse phonons. By comparing the plots for different roughness values, we gauge that with increasing roughness, a larger fraction of phonons are layer-restricted than extended. This indicates that MFP reduction due to increased roughness causes fewer phonons to transmit to adjacent layers. Interface roughness modification thus provides a crucial strategy to manipulate the amount of thermal conduction and distribution amongst its components. We next provide a thorough comprehension of the MFP spectrum of GaAs/AlAs superlattices.

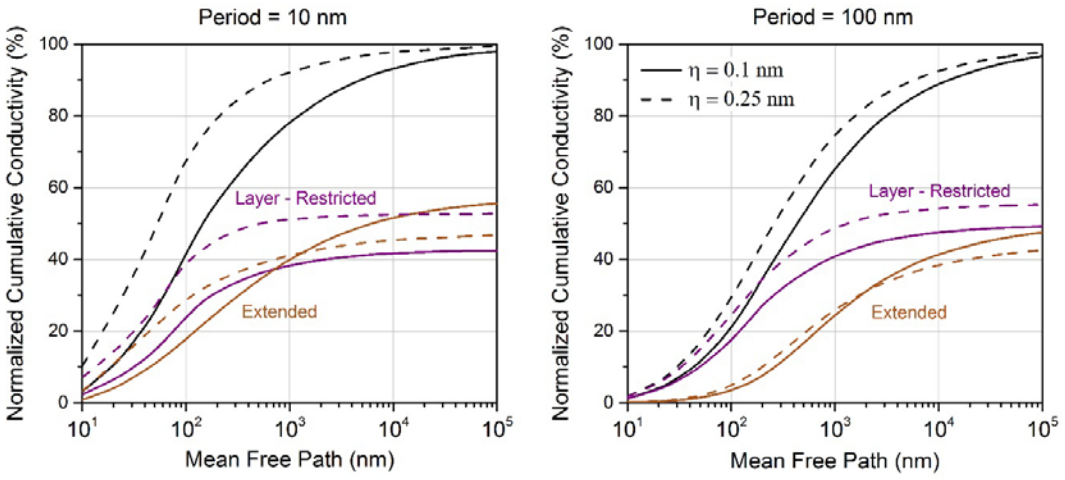

Figure 17. Mean free path spectrum for GaAs/AlAs superlattices of period length (a) 10 nm and (b) 100 nm at room temperature at interfacial roughness values η = 0.1 nm (solid lines) and η = 0.25 nm (dashed lines). The total, layer-restricted and extended phonons' thermal transport contributions are depicted by black, purple and brown lines respectively.

In Figure 17, we present the MFP spectra in GaAs/AlAs superlattices with physical parameters as considered earlier in terms of period length and roughness. We observe that with increasing period length, the spectra shift towards the right i.e. a larger proportion of

thermal conduction is through larger MFP phonons. For instance, phonons having MFP larger than 1μm carry ~20% of the total heat in a 10 nm period length superlattice (with η = 0.1 nm) whereas this proportion increases to ~35% in a 100 nm period length superlattice. This spectral shift towards larger MFPs is attributed to a reduction in the interface density. With increased interface roughness values, we see that the superlattice MFP spectra shift towards the left i.e. shorter MFPs, corresponding to an enhancement in diffusive interfacial scattering. Comparing these results to those for MFP spectra in Si/Ge superlattices [118], we note that a larger fraction of thermal conduction corresponds to extended phonons, and we attribute this to a reduced acoustic mismatch in GaAs/AlAs. This is reaffirmed in our observation of the saturation MFP, i.e. a specific MFP length of phonons beyond which additional thermal conductivity contribution is not significant, which is about 10 μm for GaAs/AlAs superlattices while this value is about 1μm for Si/Ge superlattices. In agreement with the discussion of frequency spectrum, we mark that with increasing roughness a larger fraction of thermal conduction is layer-restricted than extended.

3.2.5 Temperature Variation – Experimental Verification and Discussion

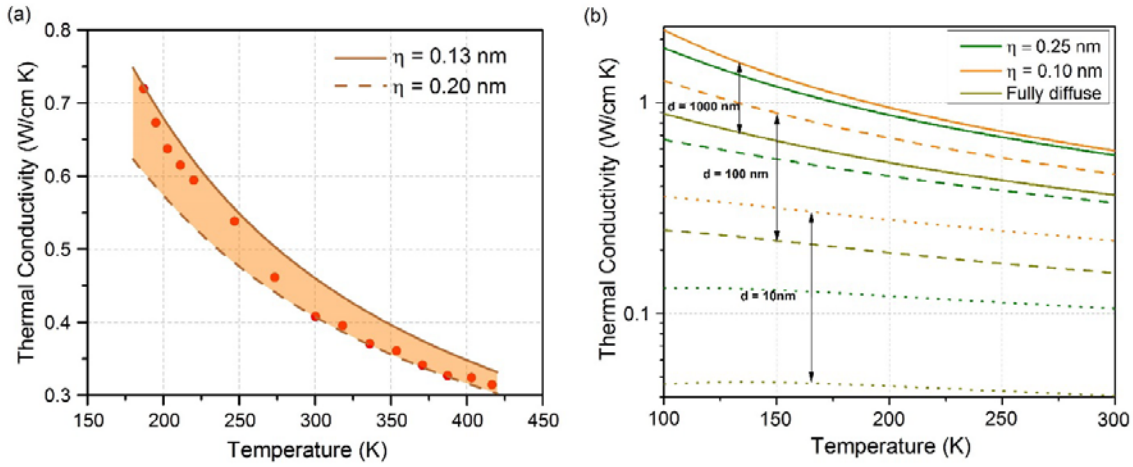

Figure 18. (a) Experimental validation of the thermal conductivity model showing reasonable agreement between predicted values (dashed and solid lines) and experimental values (orange dots) of thermal conductivity as a function of temperature in GaAs/AlAs superlattices of period length 140 nm (with equal volume fraction of either constituent) (b) Prediction of thermal conductivity of GaAs/AlAs superlattices as a function of temperature for period lengths 10 nm (dotted), 100 nm (dashed), and 1000 nm (solid) and interfacial roughness η = 0.1 nm (orange), 0.25 nm (green) and fully diffusive (dark yellow) interfaces.

We also predict the temperature variation of in-plane thermal conductivity of superlattices and compare it with previously established experimental data [125]. We provide a prediction of the thermal conductivity variation with temperature at different period lengths and for different interface roughness conditions. In Figure 18a, we show the effects of temperature on the thermal conductivity for a GaAs (70 nm)/AlAs (70 nm) superlattice in solid and dashed lines while the symbols demarcate the experimental values for measurements by Yu et. al [125]. We note that the predicted theoretical values are in good agreement with the experimental data. In Figure 18b, we present the temperature variation of thermal conductivity for GaAs-AlAs superlattices. We observe that thermal conductivity in this temperature regime reduces with increasing temperature. This is attributed to a rise in anharmonic phonon-phonon scattering with increasing temperature. We notice that with increasing period length, the thermal conductivity is a strongly varying

function of temperature. This is due to reduction in interface density which reduces the impact of the temperature-independent interfacial scattering, thereby making the temperature-dependent internal scattering the dominant scattering mechanism.

3.2.6 Application – Quantum Cascade Lasers and MQW Photodiodes

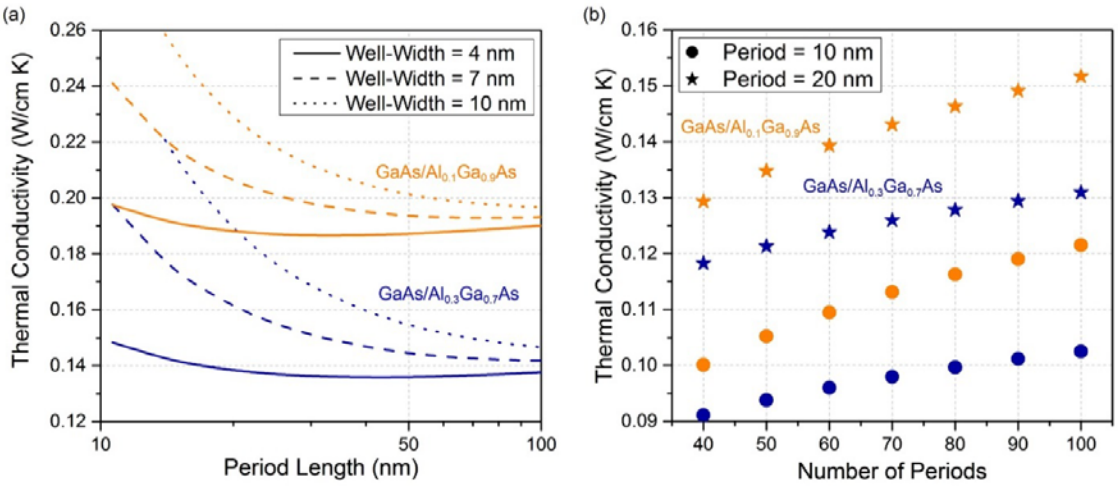

Figure 19. (a) Thermal conductivity of GaAs/$Al_{0.1}Ga_{0.9}As$ (orange lines) and GaAs/$Al_{0.3}Ga_{0.7}As$ (blue lines) superlattices as a function of period length for different well widths i.e. thicknesses of GaAs as 4 nm (solid), 7 nm (dashed) and 10 nm (dotted) lines. (b) Thermal conductivity of finite-sized GaAs/$Al_{0.1}Ga_{0.9}As$ (orange symbols) and GaAs/$Al_{0.3}Ga_{0.7}As$ (blue symbols) superlattices as a function of the number of periods in the superlattice structure for period lengths 10 nm (circles) and 20 nm (stars).

In this section, we apply the above thermal analysis to optoelectronic devices such as quantum cascade lasers (QCLs) and quantum well infrared photodetectors (QWIPs). A ubiquitous structural configuration in these devices consists of superlattice structures with large number of periods. For infrared wavelength operations, QCLs and QWIPs commonly involve GaAs/$Al_xGa_{1-x}As$ as superlattice constituent materials [14,18-20], where GaAs and $Al_xGa_{1-x}As$ layers act as potential wells and barriers, respectively. QCL active regions generate a large amount of thermal power and reducing the lattice temperature is necessary for optimum performance and avoiding damage [121]. Temporal noise at high

temperatures is a limiting factor for QWIPs [126]. Importantly, Suoto et. al. found that in-plane thermal conduction plays the primary role in determining the peak temperature in the active region of a laser diode [127]. Thus, it is imperative to develop a thorough comprehension of thermal transport in these devices. In Figure 19a, we provide quantitative predictions for in-plane thermal conductivity of GaAs/$Al_{0.1}Ga_{0.9}As$ and GaAs/$Al_{0.3}Ga_{0.7}As$ superlattices while varying the well and barrier widths. The well widths considered are 4 nm, 7 nm and 10 nm while the overall period of the superlattice has been varied from 10 to 100 nm by changing the barrier widths. We observe that thermal conductivity of GaAs/$Al_{0.1}Ga_{0.9}As$ superlattices are larger than the corresponding GaAs/$Al_{0.3}Ga_{0.7}As$ superlattices due to larger conductivity of $Al_{0.1}Ga_{0.9}As$ [122,128]. We find that, for the same period, thermal conductivity of superlattices increases with increasing well-width due to larger bulk thermal conductivity of GaAs. On the other hand, for the same well width, thermal conductivity exhibits a slight minimum with increasing barrier width. The initial decrease can be attributed to increasing volume fraction of the alloys in the superlattice while the increase is attributed to a reduction in the interface density. These conductivity predictions provide crucial insights for thermal management in optoelectronic device design. Since a variety of devices and applications employ superlattices with finite number of periods [21,129,130], we also compute the conductivity of realistic, finite-sized superlattices. We assume fully diffuse scattering at the external boundaries of the finite-sized superlattice which causes a limitation on the MFP of the extended phonons. We assume that, on an average, the z-projection of the MFP of extended phonons can take a maximum value of half of the overall superlattice length. In Figure 19b, we implement this criterion to predict the thermal conductivity of GaAs/$Al_xGa_{1-x}As$ superlattices (equal

volume fractions of GaAs and alloy) with varying number of periods. We observe that thermal conductivity increases with increasing number of periods as increasingly larger MFPs of phonons can exist. For larger number of periods, the device conductivity values approach the infinite superlattice thermal conductivity. Our theoretical predictions incorporating finite-size effects on superlattices thus allows to determine the role of device size in terms of thermal dissipation and performance.

3.3 GaAs/AlAs Superlattices – Cross-Plane Configuration

We develop and employ a rigorous phonon transport approach to elucidate and provide physical insight on cross-plane thermal transport in III-V semiconductor superlattices. Our novel approach allows to consider mode-by-mode phonon coupling between the different materials in the superlattice in addition to a rigorous description of superlattice interfaces in terms of roughness and correlation lengths. Using our approach, we study the impact of length-related physical properties such as period length and interfacial roughness, on the thermal conductivity of III-V semiconductor and their alloy-based superlattices. We present a thermal spectral analysis of the heat conduction by determining the phonon frequency spectrum and study the impact of modulating physical properties. We also contrast the findings with in-plane superlattice heat conduction [131] and predict the effective anisotropy in these multilayer nanostructures. In addition, we develop a microscopic analysis of superlattice heat conduction by establishing a modal thermal conductivity contribution for thermal phonons in GaAs/AlAs superlattices. Our findings from the finite-sized nanostructure analysis provide key inputs for designing superlattice nanostructures with desired thermal transport capabilities which is critical for III-V semiconductor based technological applications such as optoelectronic devices.

3.3.1 Period Length

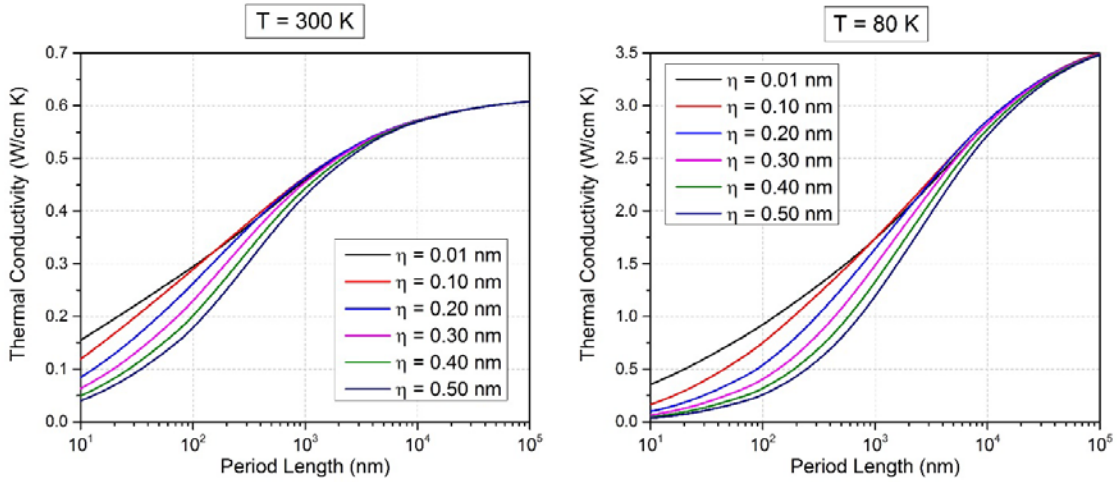

Figure 20. Cross-plane thermal conductivity for GaAs/AlAs superlattices as a function of period length for varying interfacial roughness from η = 0.00 nm to η = 1.00 nm for (a) T = 300 K and (b) T = 80 K.

We show in Figure 20 the quantitative prediction of the cross-plane thermal conductivity κ of GaAs-AlAs superlattices at temperatures T=300K and T=80K with varying period lengths from d = 10 nm to d = 100μm and interface roughnesses from η=0.00 to η=1.0 nm. We observe how the thermal conductivity decreases with decreasing period length, which can be attributed to an increase in surface scattering due to increasing interfacial density. We also notice that with increasing values of roughness η, the thermal conductivity reduces due to an enhancement in the diffusive interfacial scattering. We note that the predicted thermal conductivity values converge to the mean of bulk conductivities of GaAs and AlAs for larger period lengths independently of the surface roughness, which is consistent with the fact that for large periods the effects of the interfaces become negligible.

3.3.2 Anisotropy

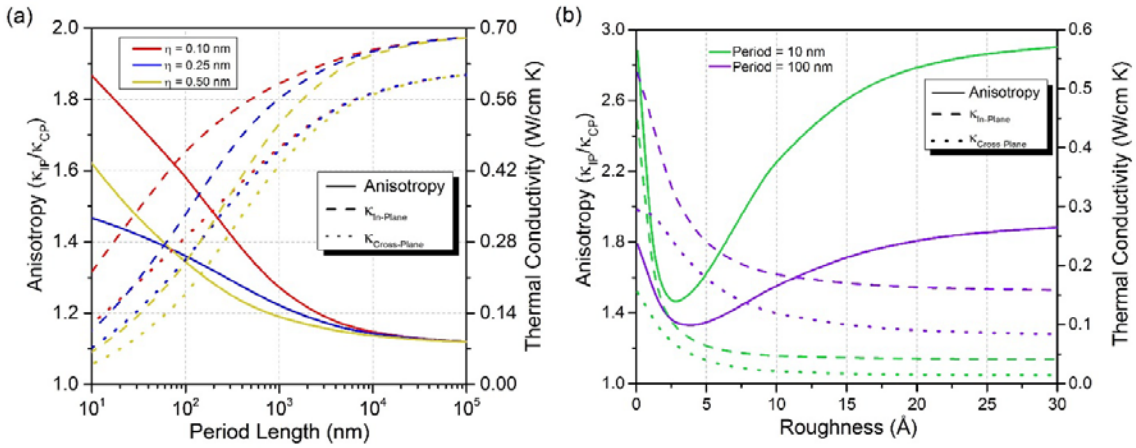

Figure 21. (a) Anisotropy ratio κ_{IP}/κ_{CP} (left axis) and in–plane κ_{IP} and cross-plane κ_{CP} thermal conductivities (right axis) as a function of period length for varying roughness values η = 0.10 nm, 0.25 nm, and 0.50 nm at T = 300 K. (b) Anisotropy and thermal conductivities as a function of interfacial roughness η for period length values d = 10 nm and d = 100 nm.

We next examine the anisotropic thermal conduction in GaAs-AlAs superlattices by contrasting the cross-plane κ_{CP} and in-plane κ_{IP} thermal conductivities. We have previously introduced a detailed treatment for computing the in-plane thermal conductivity κ_{IP} in an earlier study [131] (Also see Section 3.2). In Figure 21a, we show the variation of the ratio of in-plane thermal conductivity to the cross-plane thermal conductivity as a function of superlattice period length and for different interfacial roughness conditions. We observe that the ratio κ_{IP}/κ_{CP} is greater than one for all values of period length, meaning that κ_{CP} is smaller than κ_{IP} which is consistent with the fact that in general surface scattering has a stronger impact on cross-plane heat conduction [79,132]. However, our predictions show that the anisotropy κ_{IP}/κ_{CP} can be as high as 1.9 for low roughness and small period lengths. We notice that for large period lengths, the plots converge to κ_{IP}/κ_{CP} ~1.12 irrespective of the interfacial roughness, which is the ratio of bulk in-plane to bulk cross-plane thermal conductivity. In Figure 21b, we predict the variation of the ratio κ_{IP}/κ_{CP} as a function of the interfacial roughness for period lengths d = 10 nm and d = 100 nm. Here-

in, we discover an interesting non-linear trend, with the existence of a minimum. This can be understood from the fact that for in-plane conduction in small period length superlattices, the majority of the thermal conductivity reduction due to increasing roughness takes place at small roughness values due to shadowing and thereafter, conductivity remains fairly constant [118] whereas for cross-plane conduction the reduction at small surface roughness is less strong. The interlayer phonon coupling reduces with increasing roughness and for large roughness values we obtain the superlattice thermal conductivity that corresponds to the thermal conductivity of de-coupled thin films made of the constituent materials arranged in series and parallel for cross-plane and in-plane configurations respectively, thus causing the superlattice anisotropy to saturate with increasing roughness. For larger period lengths, the in-plane thermal conductivity reduction with roughness is much slower and thereby, the anisotropy values are lower. This detailed description of anisotropy of GaAs-AlAs superlattices can provide crucial inputs towards device design where thermal conduction needs to be modulated independently in different directions. An archetype of such a device is a directional heat spreader [5,133,134] wherein thermal dissipation is more efficient in a given direction owing to large contrast of conductivities along different directions and find applications such as thermal interface materials [135]. Thus, the above thorough investigation of anisotropy in superlattices can provide in-depth analysis for the applicability of III-V semiconductor superlattices for nanoscale thermal management applications.

3.3.3 Frequency Spectrum

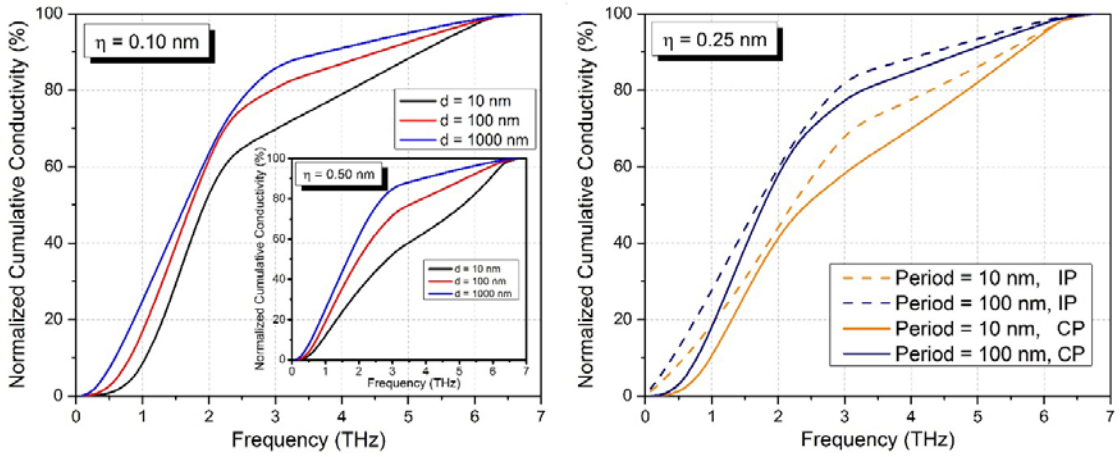

Figure 22. (a) Frequency Spectrum for cross-plane heat conduction in GaAs/AlAs superlattices at room temperature with interfacial roughness η = 0.1 nm for period lengths d = 10 nm, 100 nm, and 1000 nm. (Inset) Frequency spectrum for η = 0.5 nm. (b) Contrasting the in-plane (IP) and cross-plane (CP) frequency spectrum for GaAs/AlAs superlattices with interfacial roughness η = 0.25 nm for period length d = 10 nm and d = 100 nm.

In Figure 22, we elucidate the normalized cumulative thermal conduction spectrum in terms of the frequency of phonons in GaAs-AlAs superlattices. The spectrum indicates the fraction of heat conduction by phonons up to a certain frequency. For instance, in a GaAs-AlAs superlattice of period length d = 100 nm, with interfacial roughness η = 0.1 nm, about 80% of heat is carried by phonons having frequencies less than 3 THz at room temperature (Figure 22a). We undertake a thorough examination of the thermal spectrum and its variation with various factors such as period length and interfacial roughness. We observe that with increasing period lengths, the frequency spectrum experiences a red shift (i.e. a larger fraction of the heat is carried by phonons with lower frequencies) because a reduction in interface density reduces diffusive scattering and thereby, allows phonons with lower frequencies (and correspondingly larger MFPs) to carry more heat. As the interfacial roughness increases (contrasting with the inset in Figure 22a), the spectrum undergoes a blue shift i.e. more heat is carried by higher frequency phonons. This behavior can be

attributed to the large incremental diffusive scattering for low frequency phonons. We also compare the thermal spectra for the cross-plane and the in-plane conduction configurations of the superlattice in Figure 22b. We note that for superlattices with identical structural conditions (e.g. period, surface roughness), more percentage of heat is carried by high frequency phonons in the cross-plane configuration rather than the in-plane thermal conduction configuration due to stronger diffuse scattering effects in the cross-plane configuration. Another distinctive feature is the fact that low frequency phonons (f < 1THz) exhibit a steep increase in their thermal conductivity contribution in the in-plane case whereas they have a lesser contribution in the cross-plane configuration for surface roughness η = 0.25 nm. This indicates that large wavelength phonons with frequencies f < 1THz carry a smaller amount of heat in cross-plane superlattice. This distinction in behavior while contrasting the two geometries can be attributed to the effects of boundary scattering being in general stronger in the cross-plane structure than the in-plane case due to the direction of gradient being perpendicular to the interfaces which results in stronger interfacial scattering.

3.3.4 Temperature Variation and Experimental Validation

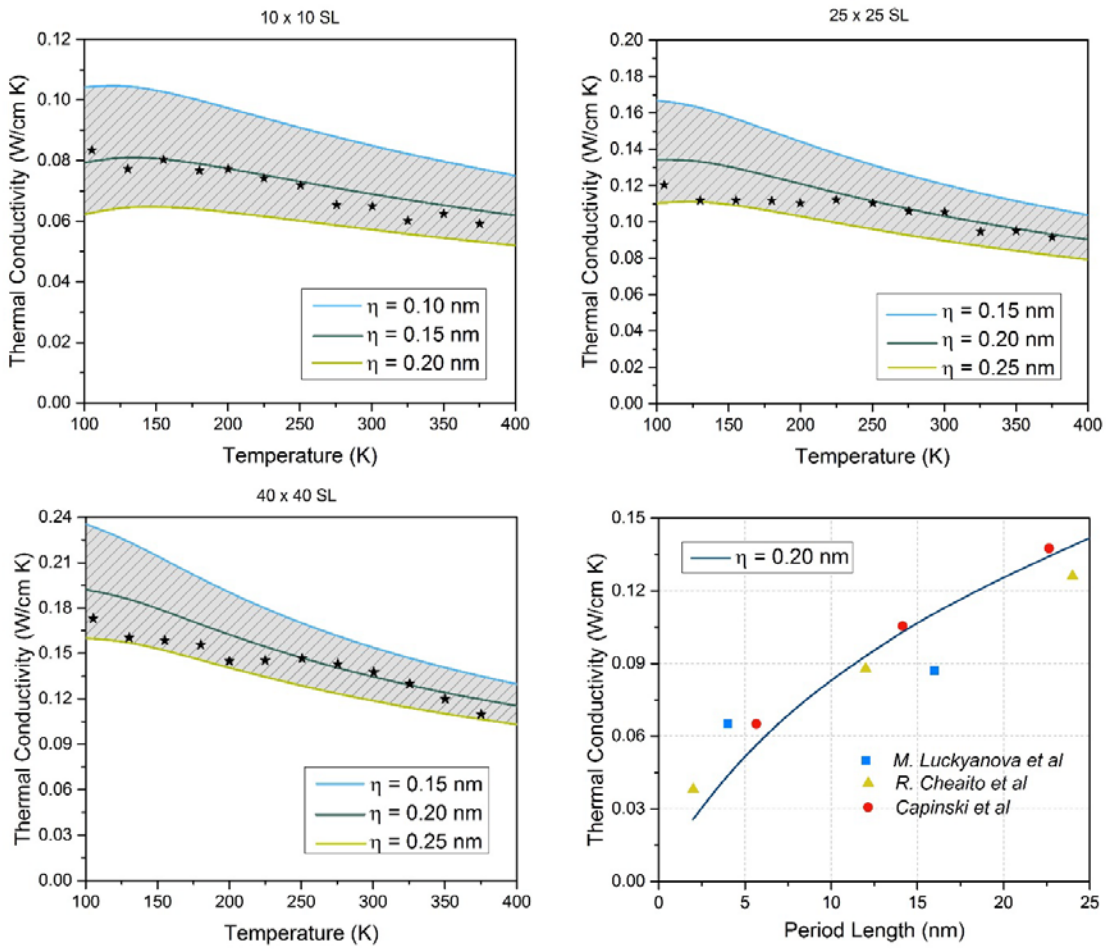

Figure 23. Experimental validation of cross-plane thermal transport predictions showing excellent agreement between the experimental data and predictions of conductivity as a function of temperature for GaAs/AlAs superlattices of period length (a) 20, (b) 50 and (c) 80 monolayers respectively. (d) Experimental data and superlattice thermal conductivity predictions with roughness η = 0.2 nm as a function of period length.

We validate our theoretical predictions through comparison of experimental measurements of thermal conductivity as a function of temperature and period length. In Figure 23a-c, we provide the thermal conductivity calculations for GaAs/AlAs superlattices with individual layer thicknesses consisting of 10, 25 and 40 monolayers respectively (periods d = 5.66 nm, 14.15 nm, and 22.64 nm). We remark that our predictions provide an excellent match with the experimental data extracted from Ref [80]

with roughness values of η = 0.15 nm (Figure 23a), η = 0.20 nm (Figure 23b) and η = 0.20 nm (Figure 23c) respectively. The relatively low interfacial roughness values are consistent since the close lattice constants of GaAs and AlAs ensure minimal lattice defects and smooth interfaces within the superlattice. To further validate our theoretical predictions, in Figure 23d we provide the thermal conductivity variation with period length in GaAs/AlAs superlattices along with experimental data from Refs. [80,85,132]. Our estimation with a roughness value of η = 0.2 nm provides a good agreement with the data and thus, substantiates our claim of low interfacial roughnesses for GaAs/AlAs superlattices. In Figure 24, we present the quantitative predictions of the variation of cross-plane thermal conductivities of GaAs-AlAs superlattices with temperature for a broad range of physical properties such as period lengths and interfacial roughnesses. We observe that for large period lengths, the thermal conductivity steadily reduces with temperature whereas with reducing period length, it exhibits a weak dependence on temperature. This can be understood in light of the interplay of phonon-phonon internal scattering and diffusive interfacial scattering effects. At large period lengths, the low interfacial density causes temperature-dependent phonon-phonon scattering to be the dominant factor whereas at small period lengths, the temperature-independent interfacial scattering is the significant determinant of the thermal conductivity. Figure 24 provides an extensive analysis on the thermal conductivity (i.e. temperature, period, and surface roughness) that allows to explore the impacts of various physical properties on thermal transport across temperatures while providing key inputs for heat modulation in device configurations.

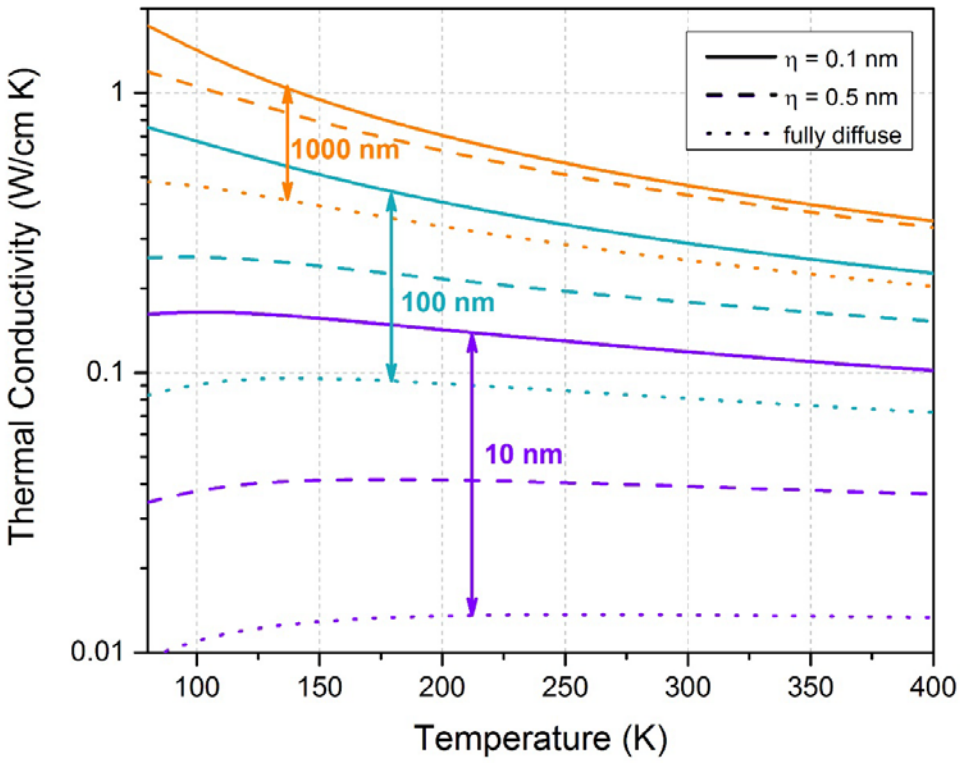

Figure 24. Thermal conductivity of GaAs/AlAs superlattices in the cross plane configuration with period lengths *d* =10 nm (purple), 100 nm (light blue), and 1000 nm (orange) with varying interfacial roughness *η* = 0.10 nm (solid), 0.50 nm (dashed) and fully diffuse (dotted) interfaces as a function of temperature.

3.3.5 Alloying

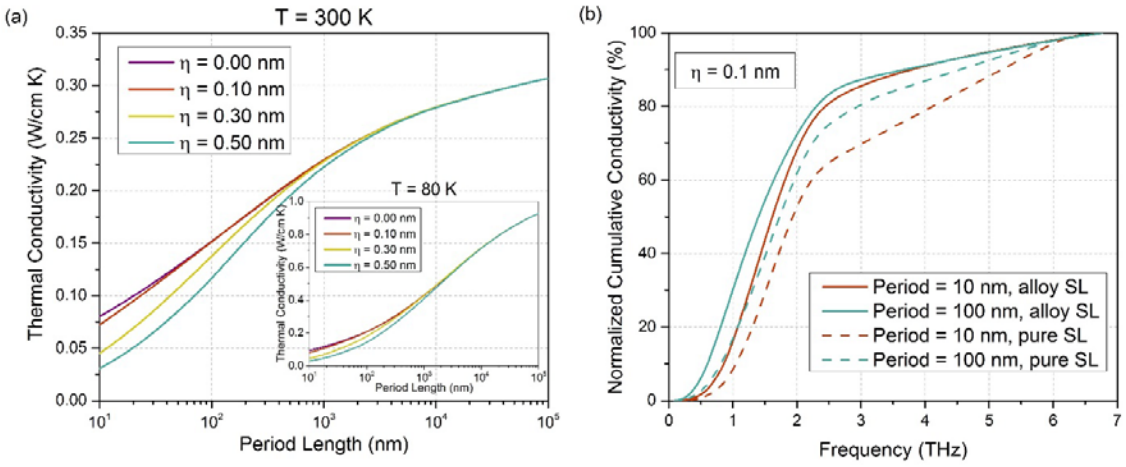

Figure 25. (a) Thermal conductivity of GaAs/$Ga_{0.1}Al_{0.9}As$ superlattices as a function of period length for varying interfacial roughness from η = 0.01 nm to η = 0.50 nm at T = 300 K and T = 80 K (Inset). (b) Contrasting room temperature frequency spectrum for GaAs/AlAs and GaAs/$Ga_{0.1}Al_{0.9}As$ superlattices of period length d = 10 nm and 100 nm with roughness η = 0.1 nm.

Alloying III-V semiconductors finds numerous application in optoelectronics such as quantum cascade lasers [4,14] and infrared photodetectors [19,20] as it allows to tailor the electronic band gaps. We next explore the impact of introducing alloy atoms on the cross-plane thermal transport in III-V semiconductor superlattices. In Figure 25a, we calculate the cross-plane thermal conductivity of GaAs/$Ga_{0.1}Al_{0.9}As$ superlattices as a function of period length at temperatures T = 300 K and T = 80 K (inset) for different interface conditions. We mark that the room temperature thermal conductivity of the alloyed superlattices is lower than that of pure GaAs/AlAs superlattices by almost a factor of 2. This is primarily attributed to the lower thermal conductivity of bulk $Ga_{0.1}Al_{0.9}As$ (κ~0.25 W/cm K) in contrast with AlAs (κ~0.90 W/cm K) due to alloy scattering of phonons. In Figure 25b, we further show the impact of alloy scattering by predicting the thermal phonon frequency spectrum for AlGaAs-superlattices while also providing a

contrast with the spectrum for pure superlattices i.e. GaAs/AlAs superlattices with no alloying. We find that a much larger fraction of heat is carried by low frequency phonons in alloy-based superlattices than that in pure superlattices. This can be attributed to the fact that alloy scattering is most impactful for high frequency phonons and increases their scattering rates significantly, thus reducing their ability to carry heat [117]. This alloy scattering feature also explains the observation that with increasing period length, the alloy superlattice spectra undergoes a smaller red shift than that for pure superlattices at high frequencies. This shows that alloying can be a valuable tool to engineer the amount of heat carried by phonons with different frequencies.

3.3.6 Modal Thermal Conductivity Analysis

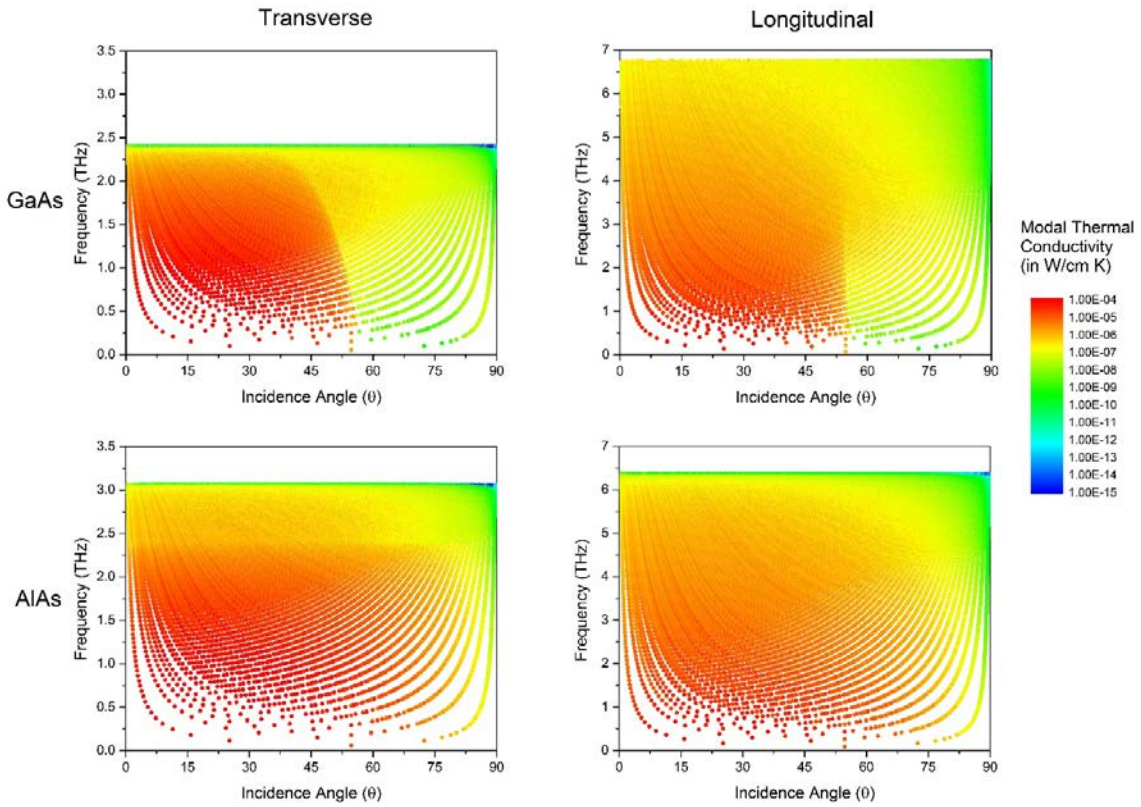

Figure 26. Modal thermal conductivity of phonons in GaAs/AlAs superlattice of period length d = 100 nm, roughness η = 0.20 nm depicted with frequency vs. incidence angle plots where color indicates the thermal conductivity of the particular mode for transverse polarization in (a) GaAs and (c) AlAs and longitudinal polarization in (b) GaAs and (d) AlAs.

A microscopic analysis of the distribution of thermal energy in superlattices necessitates a description wherein we can quantify the amount of heat carried by various phonon modes. Towards this end, in Figure 26, we present a visual analysis of the modal thermal conductivity in GaAs/AlAs superlattices by depicting the average amount of heat carried by a given phonon mode within the superlattice structure when the thermal gradient is perpendicular to the interfaces. Specifically, we depict the amount of heat carried by transverse and longitudinal polarizations for phonons starting from AlAs and GaAs by representing the modes as a function of the frequency and incidence angle with respect to the normal. Since the thermal conductivity is a function of the position, we select the center

of the layers as representative points to depict the modal analysis within the superlattice. We notice that low frequency phonons have large modal thermal conductivity (although their density of states is small). The thermal contribution of a specific frequency (and incidence angle) range can be obtained from Figure 26 by summing modal contributions of all modes within that range. For transverse and longitudinal phonons originating in GaAs (Figure 26a and b), we mark a sudden transition in the amount of heat carried by phonons depicted by the sharp transition in colors from red to yellow at $\theta \sim 54°$. This is attributed to total internal reflection (TIR) within GaAs and the loss of interlayer coupling once the incidence angle increases beyond this critical angle. This visual interpretation of modal analysis, thus, also provides the thermal transport transition within the nanostructures due to the critical angle as a function of the frequency. Since the group velocity tends to be negligible at the zone boundary for transverse phonons, we find a drastic reduction in the amount of thermal energy of phonons for transverse phonons at their high frequencies. For transverse phonons in GaAs and AlAs (Figure 26a and c), the cut-off frequency of GaAs and AlAs phonons (~2.4 THz and ~3.1THz respectively) can be clearly seen by a sudden transition in colors towards blue. On the other hand, for longitudinal phonons (Figure 26b and d) do not exhibit such sudden transition because phonon group velocities are non-zero at zone boundaries. A comprehensive modal thermal transport analysis as presented in Figure 26 elucidates the various phonon transport characteristics and trajectories and can provide vital inputs for tuning thermal conduction.

3.3.7 Applications to Nanostructured Devices

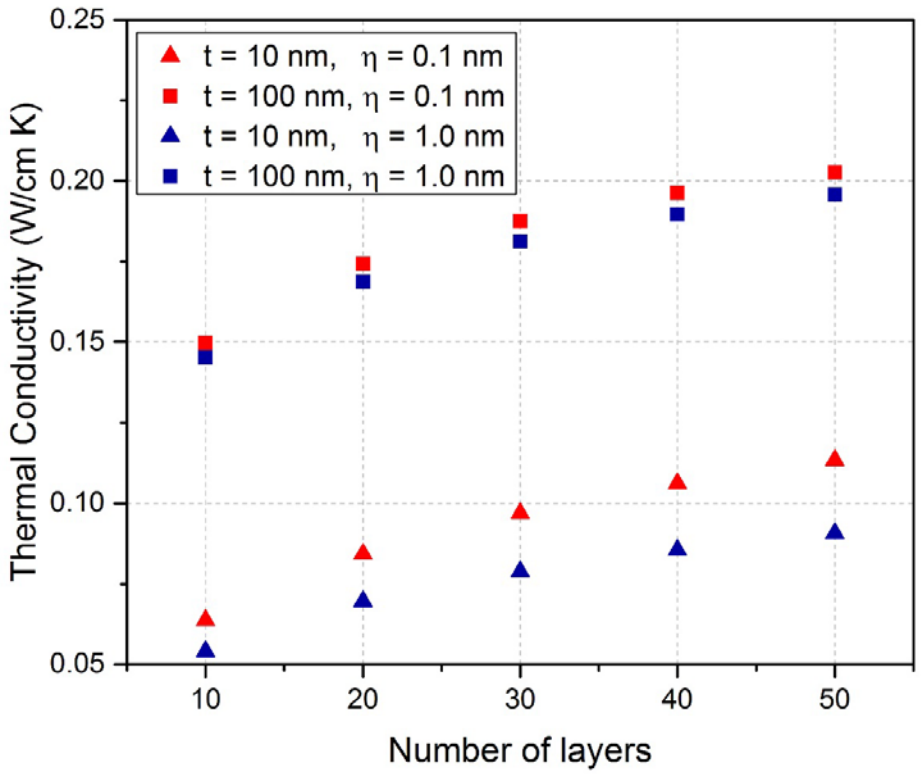

Figure 27. Thermal conductivity of finite-sized GaAs/$Al_{0.1}Ga_{0.9}As$ superlattices as a function of the number of periods for period lengths d = 10 nm (triangles) and d = 100 nm (squares) with interfacial roughness as η = 0.1 nm (red symbols) and η = 1.0 nm (blue symbols).

In this section, we apply the cross-plane thermal transport analysis to realistic finite-sized devices based on III-V semiconductor superlattices owing to their multifarious optoelectronic applications such as quantum cascade lasers (QCLs) and quantum well infrared photodetectors (QWIPs) [14,18,19]. These structures typically employ GaAs/$Al_xGa_{1-x}As$ superlattices with a finite number of periods [21,130], thus necessitating the need to compute the impact of overall device size on thermal transport. We limit the MFPs of phonons crossing multiple layers of the superlattice by assuming fully diffusive boundaries at the edges of the device, thus, setting the upper limit of the x-projection of the MFP as half of the overall superlattice size. In Figure 27, we demonstrate the effect of

increasing the number of periods on the thermal conductivity of a GaAs/$Al_{0.1}Ga_{0.9}As$ superlattice. We notice that conductivity increases with increasing number of periods due to presence of larger MFPs. For larger number of periods, the conductivity tends to that of an infinite superlattice. We also observe that there is a larger impact of overall structure size on smoother superlattices since there is lower interfacial scattering allowing more phonons to reach the boundaries of the nanostructure. Thus, these predictions provide useful inputs which can be utilized to guide device design and thermal management in typical nanostructured devices.

3.4 Film-on-Substrate

Thin-film on substrate is a ubiquitous system in optoelectronic applications as they constitute fundamental architectures for various types of devices such as lasers, photodetectors, and LEDs [86,88-92,110-112,136,137]. Although enhancing thermal conduction is essential to create highly efficient electronics and optoelectronics, to date, a large number of studies on nanomembranes [8-10,12,94,96,99] have shown that thermal conduction decreases as the spacing is decreased and the development of approaches that enable to increase heat conduction in these nanosystems has been difficult. In this work, we show that, in contrast to established understanding of thermal transport, the in-plane thermal conduction of film-on-substrate nanomembranes can be increased with decreasing film thicknesses, which is exactly opposite to free-standing and silicon-on-insulator studies which predict that it decreases. Specifically, we demonstrate how thermal conduction in film-on-substrate (FOS) systems is distinct from free-standing thin films and emphasize on the importance of taking into account accurate thermal conductivities for design of FOS optoelectronic devices and read out from experiments. We study the cases of a Ge thin film

grown over Si substrate and an $Al_{0.1}Ga_{0.9}As$ thin film grown over GaAs substrate. We show that for semiconductor substrates such as Si and GaAs, accounting for thermal coupling between substrate and thin film is necessary to accurately understand heat transport in FOS based heterostructure devices. We evaluate the physical mechanism behind the thermal conductivity dependence on different structural conditions while rigorously accounting for interfacial coupling. We also perform a detailed examination of the thermal phonon spectra in terms of thermal conductivity contributions by phonons with different frequencies and mean free paths, thereby systematically studying the effects of substrate-thin film coupling. Rationally designed phonon coupling in FOS architectures can lead to a fundamental new approach for thermal management in optoelectronic devices such as infrared photodetectors and LEDs.

3.4.1 AlGaAs Thin-Film on GaAs Substrate – Thin Film Thickness Variation

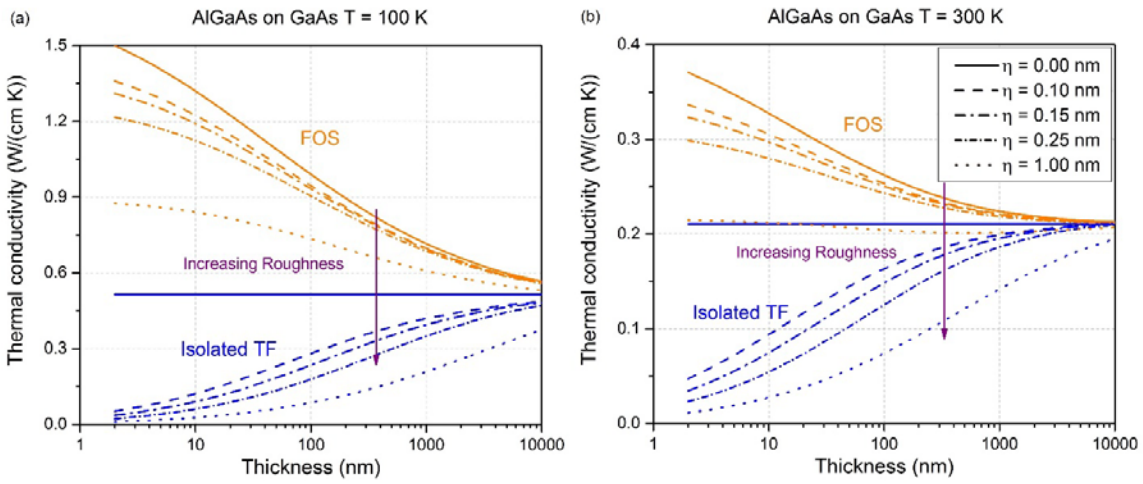

Figure 28. Thermal conductivity of an $Al_{0.1}Ga_{0.9}As$ thin film grown on GaAs substrate in FOS architecture (orange lines) and an isolated free-standing $Al_{0.1}Ga_{0.9}As$ thin film (blue lines) for different interfacial roughnesses at temperatures (a) T=100 K and (b) T=300 K. The vertical arrow denotes the direction of increasing roughness. Blue horizontal line corresponds to the bulk thermal conductivity of $Al_{0.1}Ga_{0.9}As$.

We show in Figure 28 the predicted thermal conduction variation of a ternary alloy $Al_{0.1}Ga_{0.9}As$ thin films atop a GaAs substrate for the case of equal inner and outer surface conditions, while varying the thickness of the $Al_{0.1}Ga_{0.9}As$ thin film. Our calculations show that the thermal conductivity κ of the thin film in the FOS architecture increases with decreasing thickness, which is exactly the opposite of the conventional free-standing calculations [12,102] which predict that it decreases. Specifically, we found that the thermal conductivity of a nanofilm in a FOS structure can be larger than the bulk thermal conductivity (horizontal blue line) as well as that of an isolated, free-standing nanomembrane of the same material with similar structural properties. The observed enhancement in the thermal conductivity ($\Delta\kappa$) of the $Al_{0.1}Ga_{0.9}As$ film is attributed to phonon injection from the substrate [107]. For certain surface conditions, interfacial coupling between the thin film and the substrate allow phonons to be exchanged between the two media. In the FOS case we consider, the phonon mean free paths (MFP) of the substrate material are larger than their corresponding thin-film phonon MFP. Since the local thermal conductivity at a point inside the thin film is determined by the effective MFP of phonons reaching that point, the local thermal conductivity of the thin-film in the FOS structure is enhanced beyond the isolated thin-film value due to an injection of larger MFP phonons from the substrate, which leads to a larger effective MFP for phonons in the thin-film. For the case when phonons in the thin film have larger MFPs compared to the substrate, the thermal conductivity of the FOS would be smaller than the corresponding isolated thin-film. It is noteworthy that the thermal conductivity κ of the film can be enhanced beyond the $Al_{0.1}Ga_{0.9}As$ bulk conductivity value. We denote this enhancement of thermal conduction beyond the bulk conductivity values by $\Delta\kappa_{bulk}$ whereas we denote

the enhancement beyond isolated thin film conductivity values as $\Delta\kappa_{iso}$. We remark that we observe an increasing $\Delta\kappa_{bulk}$ with reducing thickness of thin film for a wide range of interfacial roughnesses. This finding can have profound consequences since achieving enhanced thermal conduction is a key component of enabling heat dissipation from hot spots in optoelectronic and microelectronic applications. The facilitation of effective heat dissipation in nanostructures can further promote miniaturization and efficient power consumption in devices. We observe this trend of enhancement beyond bulk conductivity $\Delta\kappa_{bulk}$ to be significant even at T = 300K, which shows that devices will be competent for room temperature operation as well. We note that, the unconventional increase in the thermal conductivity of the thin film in the FOS architecture with decreasing thickness can be understood in light of recognizing the role of interfacial scattering and film thickness. For small roughnesses we have low diffusive interfacial scattering, and due to the low acoustic impedance mismatch between $Al_{0.1}Ga_{0.9}As$ and GaAs there is a strong interlayer phonon coupling in the system. With decreasing film thickness, the volume fraction in the film in which there is an enhancement of thermal conductivity arising from interlayer phonon coupling increases because phonons being injected from GaAs, which have finite MFP, are allowed to influence a larger film proportion. As a result, the thermal conductivity κ of the film increases with decreasing thickness for η = 0, 0.10, 0.15 and 0.25 nm because the enhancement by phonon coupling is larger than the decrease by diffuse interface scattering. On the other hand, for the isolated free-standing thin film, we observe a reduction in thermal conductivity with decreasing thickness, which is due to conventional boundary scattering. Note that in this case there is no interlayer phonon coupling and therefore there are no physical mechanisms to observe an increase in heat conduction.

Significantly, we found that the different physical mechanisms behind thermal transport in isolated and FOS nanomembranes can lead to opposite thermal conductivity behaviors when the film thickness is reduced. We note that we investigate the thermal conductivity of the thin film atop the substrate and not that of the entire structure consisting of the substrate and thin film. Figure 28 also shows how the thermal conductivity increases with reducing roughness and temperature. We remark that for case of very rough interfaces (e.g. η = 1.0 nm) and T=300 K (Figure 28b), we observe a minimum in thermal conductivity for a film thickness close to t = 500 nm, which is due to the competition between thermal conductivity enhancement by phonon coupling and thermal conduction reduction by interfacial scattering. We highlight that this minimum in thermal conductivity is independent of any thermal phonon wave effects or coherent heat conduction which have been reported in other studies [33,65,124,138].

3.4.2 Ge Thin-Film on Si Substrate – Thin Film Thickness Variation

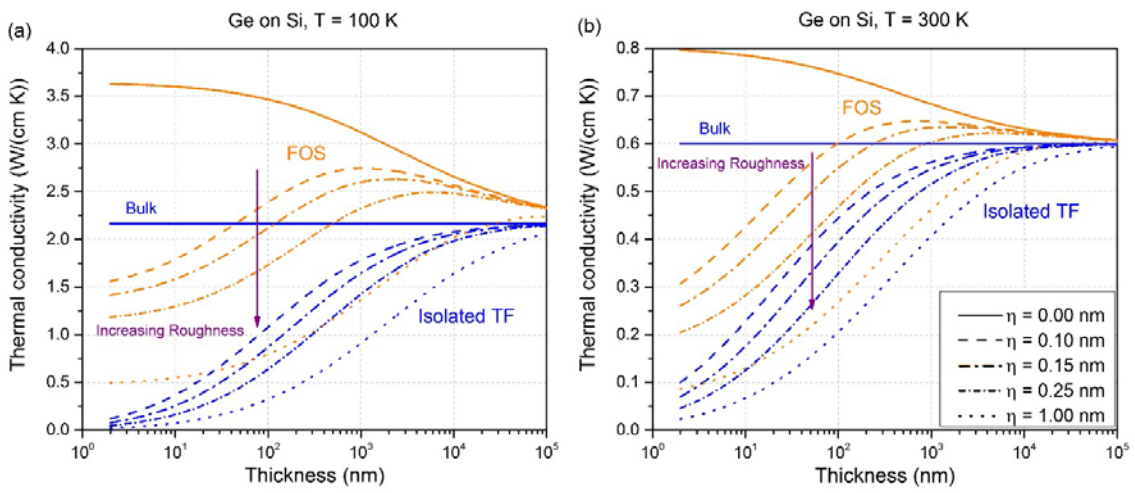

Figure 29. Thermal conductivity of a Ge thin film grown on Si substrate in FOS architecture and an isolated free-standing Ge thin film depicted by orange and blue lines respectively for different interfacial roughnesses at temperatures (a) *T* = 100 K and (b) *T* = 300 K. Blue horizontal line corresponds to bulk thermal conductivity of Ge.

In Figure 29a and Figure 29b, we consider an FOS system consisting of a thin film of Ge deposited on a Si substrate, where we study the variation of thermal conductivity of the FOS film and contrast it with that of bulk Ge and an isolated thin film of Ge. Our numerical predictions show that for certain surface conditions and thicknesses the thermal conductivity of the thin film on substrate still increases beyond the bulk Ge thermal conductivity with decreasing thickness but enhancement effects by phonon coupling are less pronounced in this case due to dissimilar dispersion relations for Si and Ge. The thermal conductivity of FOS is also enhanced beyond the corresponding isolated thin film conductivity values. We note that a large acoustic impedance between Si and Ge owing to a difference in densities and phonon mode velocities leads to significant reduction in transmission and phonon coupling in the Si-Ge case. Thus with decreasing thickness, we generally observe a decrease in the thermal conductivity of the FOS due to increasing

diffuse scattering effects. However, for cases where the interfacial diffuse scattering is not the dominant mechanism (for instance, when $\eta = 0$) the thermal conduction increases since the volume fraction in which the enhancement takes place increases with decreasing spacing. These combined mechanisms for phonon transport (phonon coupling and interface scattering) also explain the maxima observed in the thermal conductivity of the FOS Si-Ge system. We also mark that the thermal conductivity enhancement ($\Delta\kappa_{iso}$), diminishes with increasing thickness of the thin film. This is due to the reducing influence of surface scattering and phonon coupling and the fact that thin film conductivities tend towards the bulk conductivity with increasing thickness. We also show in Figure 29 the impact of surface conditions and temperature variation and find how the thermal conductivity and its enhancement increases with reduction in surfaces roughness and temperature.

3.4.3 Frequency Spectrum

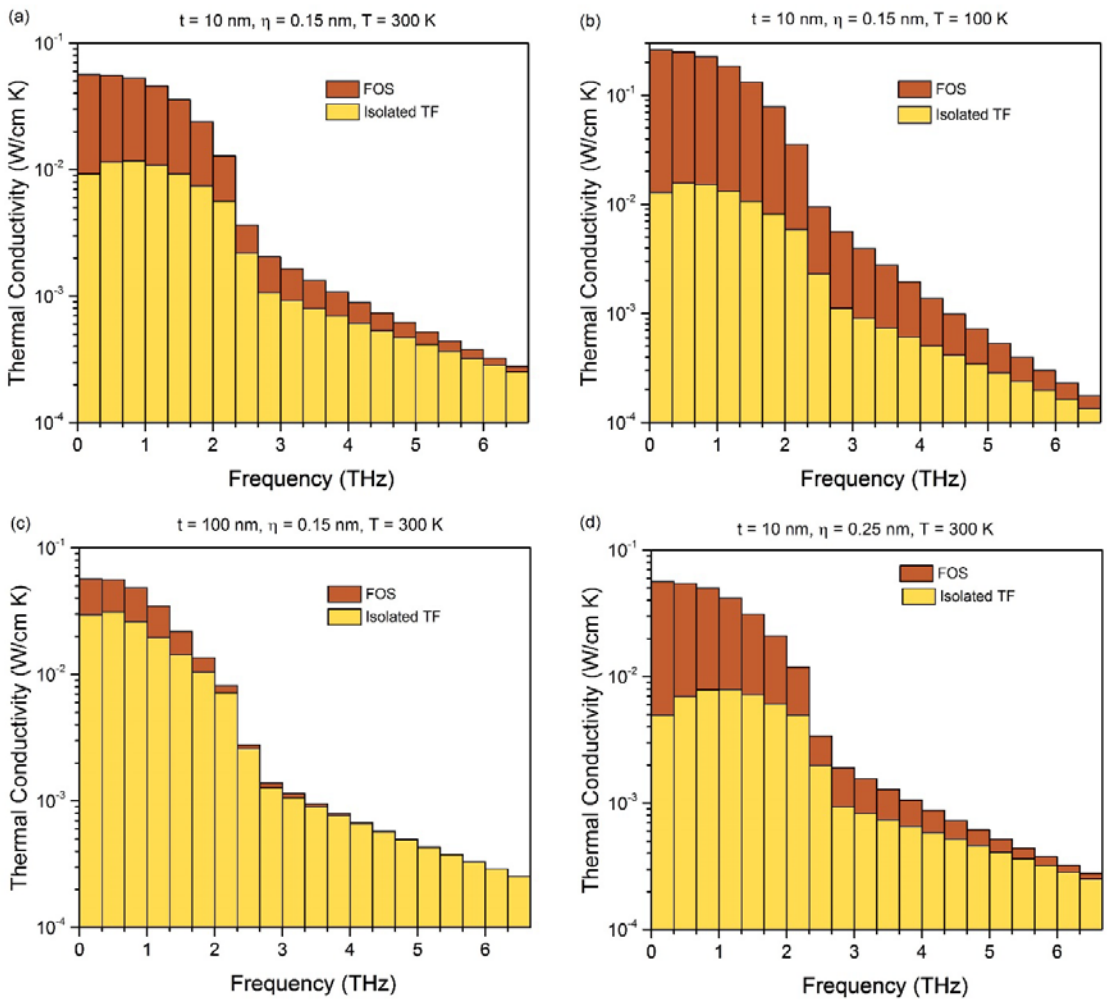

Figure 30. Frequency spectrum of an $Al_{0.1}Ga_{0.9}As$ thin film grown on GaAs substrate in FOS architecture (orange) and an isolated free-standing $Al_{0.1}Ga_{0.9}As$ thin film spectrum (yellow) depicted in terms of the thermal conductivity contributions of different frequency ranges for the following configurations (a) t = 10 nm, η = 0.15 nm, T = 300 K, (b) t = 10 nm, η = 0.15 nm, T = 100 K, (c) t = 100 nm, η = 0.15 nm, T = 300 K , and (d) t = 10 nm, η = 0.25 nm, T = 300 K where t is thickness of thin film, η is interfacial roughness and T is temperature.

In order to provide additional insights and guidelines for the rational design of FOS nanostructures, we next present an in-depth spectral analysis of the phonon injection mechanism and its effects on the spectral thermal conductivity. In particular, we focus on determining the enhancement in thermal conductivity for phonons with different thermal phonon frequencies and mean free paths. In Figure 30, we show the thermal phonon

frequency spectrum for an $Al_{0.1}Ga_{0.9}As$ over GaAs FOS system and compare it with the spectrum for a free-standing $Al_{0.1}Ga_{0.9}As$ thin film. Note that we present the spectrum in terms of the thermal conductivity contribution of different frequency bands. In Figure 30a, the $Al_{0.1}Ga_{0.9}As$ thin film has thickness t = 10 nm and inner and outer roughness of η = 0.15 nm at T = 300 K. We observe that the spectral thermal conductivity for the FOS shows a clear enhancement compared to the thin-film spectrum. In particular, this enhancement is larger for lower frequencies while it diminishes as the frequency increases. This is attributed to the fact that diffusive interfacial scattering reduces at lower frequencies, which allows for larger phonon interlayer coupling and thermal conductivity enhancement. The predominance of enhancement for low frequency phonons also explains why there is a steady decline for thermal conductivity spectral contributions as the frequency increases for the case of FOS. On the other hand, the isolated thin film spectrum exhibits a maxima which is a consequence of the competition between a rise in phonon occupation and reduction in scattering times (phonon-phonon and boundary scattering) with increasing frequency. We have also examined the dependence of the frequency spectra with changing temperature, thickness, and interfacial roughness. In Figure 30b we compare the FOS and isolated thin film spectra with same physical parameters at T = 100 K and notice a boost in the thermal conductivity enhancement due to the reduction in phonon-phonon scattering. In addition, we show the modulation in thermal spectrum with film thickness by considering an $Al_{0.1}Ga_{0.9}As$ thin film of thickness t = 100 nm at T = 300 K in Figure 30c. We see that the reduction in enhancement due to the large spacing leads to high frequencies having almost equal contribution for the FOS and isolated thin film systems. In Figure 30d, we provide the thermal frequency spectrum at t = 10 nm and a larger interface roughness

η = 0.25 nm, and found that the enhancement $\Delta\kappa_{iso}$ at lower frequencies is higher than $\Delta\kappa_{iso}$ at η = 0.15 nm (Figure 30a) due to larger impact of diffuse scattering on the low frequency spectrum of the isolated thin film.

3.4.4 Mean Free Path Spectrum

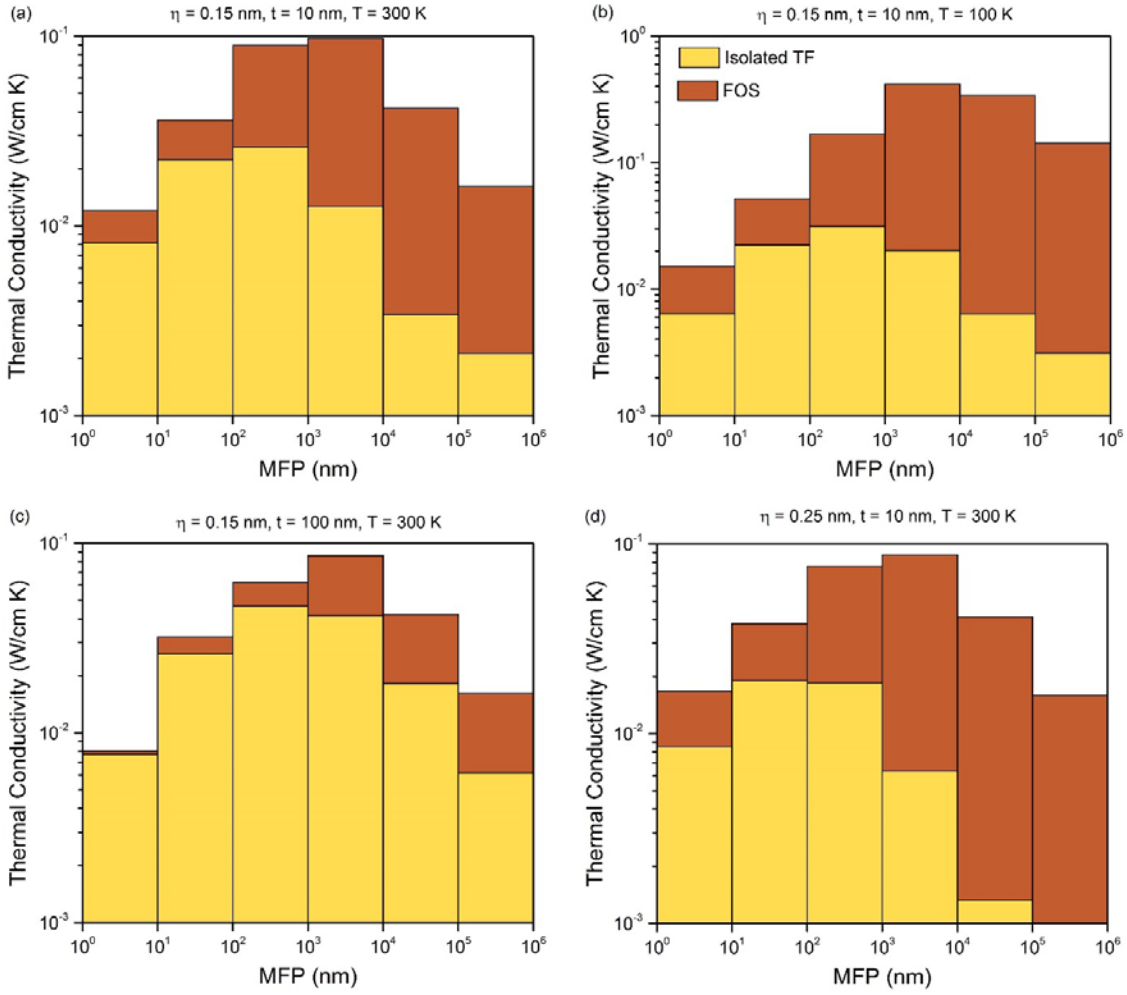

Figure 31. Mean Free Path spectrum of an $Al_{0.1}Ga_{0.9}As$ thin film grown on GaAs substrate in FOS architecture (orange) and an isolated free-standing $Al_{0.1}Ga_{0.9}As$ thin film spectrum (yellow) depicted in terms of the thermal conductivity contributions of different mean free path ranges. The variation of thermal spectrum is shown for (a) *t* = 10 nm, η = 0.15 nm, *T* = 300 K, (b) *t* = 10 nm, η = 0.15 nm, *T* = 100 K, (c) *t* = 100 nm, η = 0.15 nm, *T* = 300 K, and (d) *t* = 10 nm, η = 0.25 nm, *T* = 300 K.

In addition to understanding the thermal energy distribution within different frequency bands, comprehension of mean free path spectrum is vital in designing nanomaterials for efficient thermal transport. In Figure 31 we contrast the thermal phonon MFP spectrum of the $Al_{0.1}Ga_{0.9}As$ over GaAs FOS and $Al_{0.1}Ga_{0.9}As$ thin film architectures in terms of the thermal conductivity contributions of different MFP ranges which differ by one order of magnitude. We show in Figure 31a the thermal MFP spectrum for an $Al_{0.1}$-$Ga_{0.9}As$ thin film of thickness 10 nm with inner and outer roughness of $\eta = 0.15$ nm at T = 300 K. Different thermal conductivity enhancements $\Delta\kappa$ are observed for different MFPs and we note that the enhancement as well as thermal conductivity κ contribution undergoes a maxima for MFP lengths lying in $\ell=10^3$-10^4 nm range. The κ maxima is explained by considering that short MFP phonons (i.e. high frequency) have high scattering rates while large MFP (i.e. low frequency) phonons have low occupation probabilities. We undertake a thorough investigation of this spectral distribution by considering the impact of temperature, film thickness and interfacial roughness. In Figure 31b, we present the MFP spectral analysis for similar physical features of the FOS and isolated thin film at a temperature T = 100 K. We observe that for the temperatures under consideration the MFP range for maximal thermal conductivity contribution κ remains essentially constant but thermal conductivity enhancement $\Delta\kappa$ for larger MFPs increases much more than it does for lower MFPs. This aligns with reduced phonon-phonon scattering at the lower temperature. We predict that shifting the maximum contribution MFP range to a higher value is possible upon further lowering of temperature (not shown). We study the case of larger thin film thickness in Figure 31c and find that there is a significant reduction in thermal conductivity enhancement $\Delta\kappa_{iso}$ across phonon MFPs when contrasted with the

enhancement in Figure 31a. Upon changing the interfacial roughness to a higher value in Figure 31d, enhancement of large MFP (> 10^4 nm) phonons increases which aligns with the observation in the frequency spectrum in Figure 30d. A detailed study of the thermal phonon MFP spectrum and quantitative predictions of its modification upon varying physical conditions can provide key inputs for controlling thermal transport in FOS-based nanostructures and optoelectronic devices.

3.4.5 Thermal Conductivity Enhancement Spectrum

Since our focus is to understand the impact of interfacial coupling on heat transfer augmentation, we also analyze the thermal spectra by quantifying the thermal conductivity enhancement. In this section, we investigate the significance of interfacial characteristics on the coupling in FOS architectures through a spectral analysis by studying the cumulative thermal conductivity enhancement ($\Delta\kappa_{iso} = \kappa_{FOS} - \kappa_{thin\text{-}film}$) as a function of thermal phonon frequencies and MFPs.

3.4.5.1 $Al_{0.1}Ga_{0.9}As$ thin-film on GaAs substrate

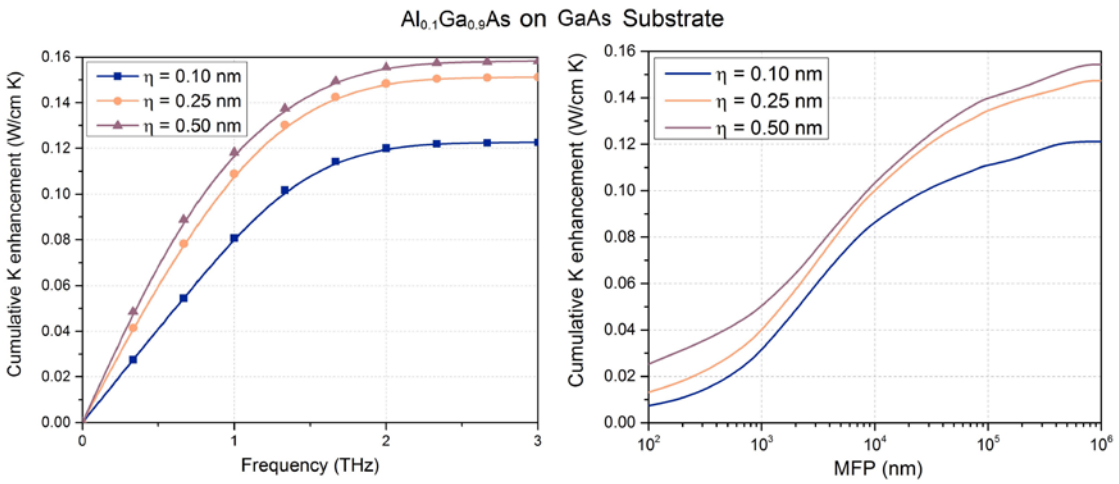

Figure 32. Phonon spectra in terms of cumulative thermal conductivity enhancement as a function of frequency and MFP in a $Al_{0.1}Ga_{0.9}As$ thin-film (thickness t = 50 nm) on GaAs substrate system with interfacial roughnesses as η = 0.10 nm, 0.25 nm and 0.50 nm.

In Figure 32, we show the thermal conductivity enhancement spectrum for an $Al_{0.1}Ga_{0.9}As$ on GaAs FOS in terms of the cumulative thermal conductivity as a function of thermal phonon frequency and MFPs for thin film thickness t = 50 nm. This depicts the $\Delta\kappa$ until a certain phonon frequency or MFP. We observe that thermal conductivity enhancement increases with an increase in roughness. This finding seems rather counterintuitive since the transmission coefficient decreases with increasing roughness. We can understand this behavior by realizing that thermal conductivity enhancement is determined by the amount of increase in conductivity over the baseline thermal conductivity of an isolated thin film. Since $Al_{0.1}Ga_{0.9}As$ and GaAs have very close dispersion relations and low acoustic mismatch, transmission is not significantly lowered with increasing roughness. However, the thermal conductivity of the isolated thin film undergoes a significant decline owing to boundary scattering from rough interfaces [102]. Since the small change in transmission is outweighed by the reduction of isolated thin-film

conductivity, we find that thermal conductivity enhancement increases with increasing roughness. Note that, in-plane thermal conductivity of a smooth $Al_{0.1}Ga_{0.9}As$ isolated thin film or FOS is larger than the corresponding structures with larger roughness. We observe, in Figure 32a, that enhancement per unit frequency decreases with increasing frequency due to a reduction in transmission and the spectrum saturates at about 2 THz. We also note in Figure 32, that the increase in enhancement is smaller when roughness increases from η = 0.25 nm to η = 0.50 nm in contrast with η = 0.10 nm to η = 0.25 nm. This is in alignment with the limiting case of fully diffusive interface, where we have negligible enhancement (but this is only possible for very large roughness values), thus indicating that enhancement would achieve a maximum for a certain roughness value.

3.4.5.2 Ge thin-film on Si Substrate

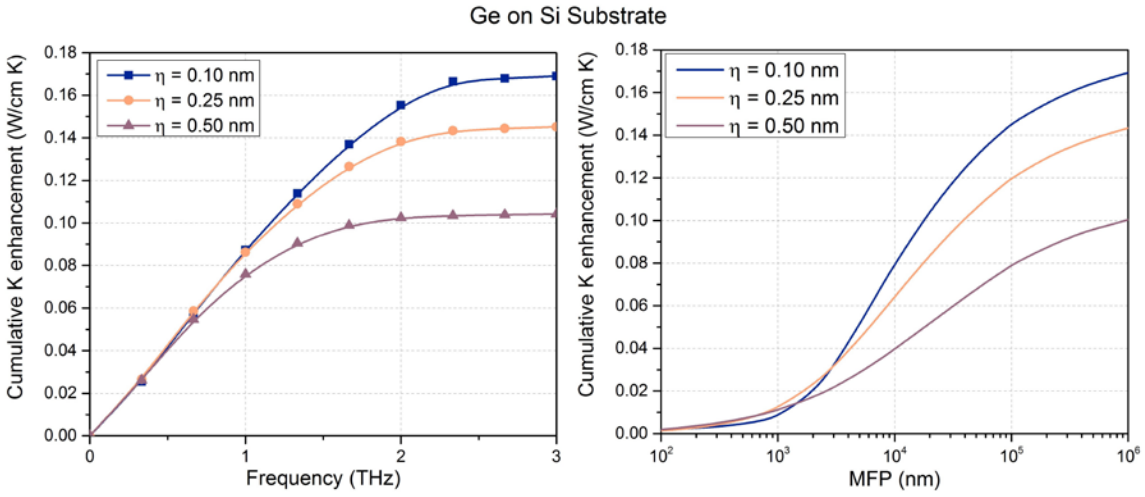

Figure 33. Phonon spectra in terms of cumulative thermal conductivity enhancement as a function of frequency and MFP in a Ge thin-film (thickness *t* = 50 nm) on Si substrate system with interfacial roughnesses as *η* = 0.10 nm, 0.25 nm and 0.50 nm.

We show, in Figure 33, the analogous thermal conductivity enhancement spectra for a Ge on Si FOS for a thin-film with similar structural properties. We observe that with

increasing roughness thermal conductivity enhancement reduces. Accounting for the role of significant dispersion and acoustic mismatch between Si and Ge, we find that transmission coefficient reduces significantly with increasing roughness. In the case of Ge on Si FOS, the reduction in thermal conductivity of FOS due to a reduction in transmission outweighs the reduction in thermal conductivity of the isolated free-standing thin film. This is in contrast with the $Al_{0.1}Ga_{0.9}As$ on GaAs case where we observe the opposite trend due to similar dispersion relations and low acoustic mismatch. This provides us a key insight into how acoustic mismatch and dispersion similarity affect the significance of roughness in coupling and thereby, influence the enhancement spectra. We observe, in Figure 33a, that thermal conductivity enhancement spectrum saturates around a frequency of about 3 THz. Contrasting the MFP spectra of Ge on Si FOS system in Figure 33b with that of the $Al_{0.1}Ga_{0.9}As$ on GaAs in Figure 32b, we find that the phonon injection mechanism/coupling results in enhancement across all MFPs for the latter case while it is only observed at large MFPs in the former case of Ge on Si. Similar dispersion relations of $Al_{0.1}Ga_{0.9}As$ and GaAs allow phonons from one media to readily transmit into the other owing to easily satisfying the transmission conditions. In the case of Si and Ge, only phonons below 2.4 THz (transverse) and 7.2 THz (longitudinal) can find corresponding phonons upon transmission. Therefore, low frequency phonons having large MFPs undergo significant enhancement. These observations in the spectral analysis can have important experimental consequences for thermal conductivity readout procedures since they provide an in-depth understanding of enhancement and its dependence on interfacial characteristics as well as dispersion and acoustic mismatch.

3.4.6 Varying Interfacial Roughness

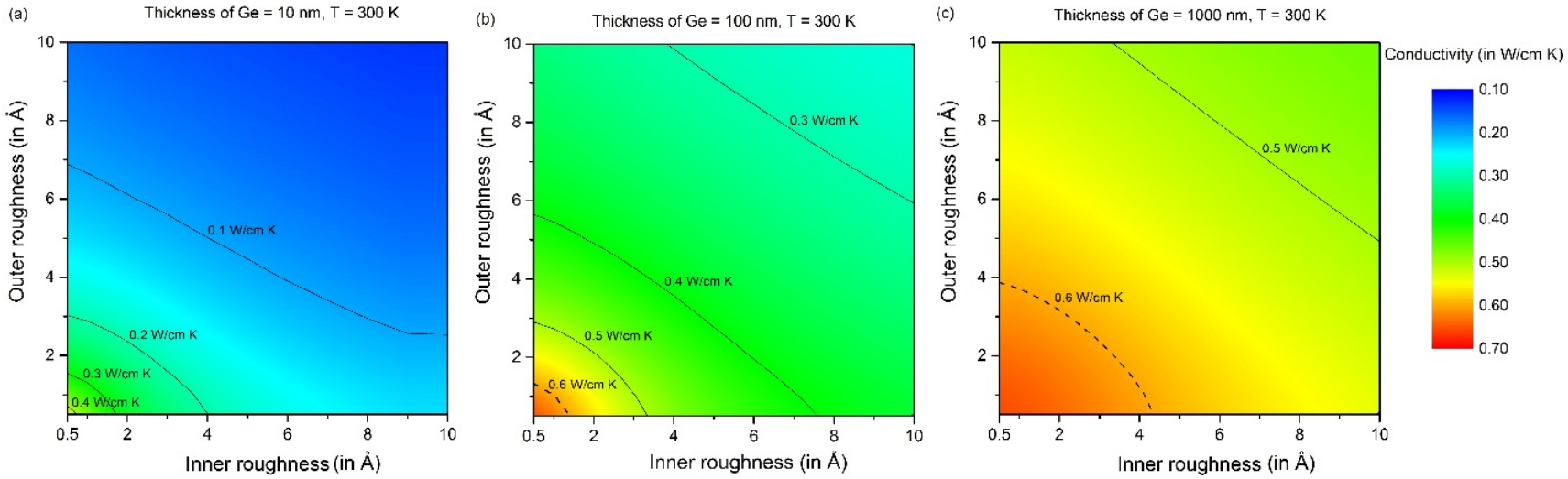

Figure 34. Thermal conductivity variation of a Ge thin film grown on Si substrate in FOS architecture as a function of inner η_i and outer η_o interfacial roughness of the film for thicknesses (a) t = 10 nm, (b) t = 100 nm, and (c) t = 1000 nm at temperature T = 300 K. Black solid lines are constant conductivity contours while dashed line denotes the bulk thermal conductivity of Ge ~ 0.6 W/cm K.

Since thermal phonon coupling between thin film and substrate is expected to be influenced by the system structural conditions, we next investigate the effects on thermal conductivity of FOS that result from varying the inner (thin film-substrate interface) and outer (thin film-air) interfacial roughness individually. To this end, we present in Figure 34a-c, the thermal conductivity for an FOS system consisting of a Ge thin film on a Si substrate, where we quantitatively predict thermal conduction for varying Ge thin film thicknesses from t=10 nm to t=1000 nm. We observe different thermal conductivity dependence on inner roughness as compared to outer roughness, thus leading to asymmetric contours of constant thermal conductivity. We see that there is a higher thermal conductivity reduction when increasing inner roughness contrasted to the case of increasing outer roughness. This is ascribed to the additional diffusive interfacial scattering due to partial transmission and reflection of phonons at the inner interface, whereas phonons at the outer interface only have specular and diffusive reflections. We have demarcated in Figure 34 with dashed black line the contours denoting the bulk value of the thermal conductivity of Ge as ~0.6 W/cm K at T = 300 K. These constitute indicators of the upper bounds of interfacial roughness in order to exceed the bulk value of thermal conductivity of Ge in the FOS via interlayer phonon coupling.

3.5 Fundamental Inquiry into Interfacial Coupling

Upon having elaborated a thorough evaluation of the thermal conductivity enhancement in FOS architectures, we provide a deeper investigation of phonon interfacial coupling. We furnish a 2D quantitative analysis of the transmission coefficient and its dependence on phonon frequencies, interfacial roughness and acoustic and dispersion mismatch of the materials across an interface. We postulate an averaged transmission

coefficient by taking an average of transmission coefficients across all transmitted wavevectors between two media and study their variation with interfacial roughness. We investigate the impact of coupling in terms of thermal conductivity enhancement in FOS architectures, and generate visual illustrations of localized thermal energy distribution in these structures and contrast them with those in bulk materials and isolated thin-films. This unique heat visualization provides for how thermal phonon MFPs are spatially distributed and details the impact of nanostructuring and interfacial coupling on this distribution. We also examine the dependence of the spatial distribution on the interfacial roughness, temperature and choice of different media across the interface. This fundamental analysis paves the way to comprehend interfacial coupling between materials in terms of experimentally quantifiable parameters.

3.5.1 Transmission Coefficient Analysis

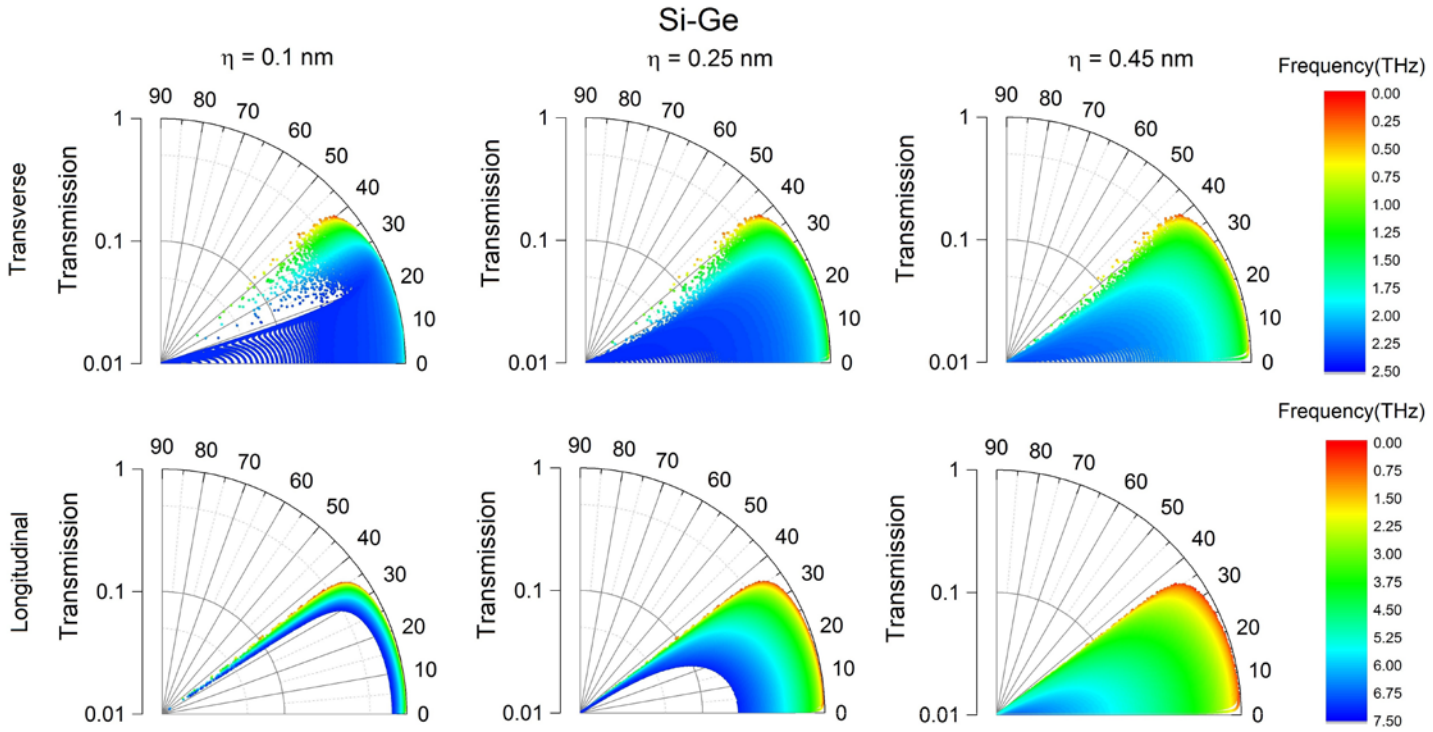

Figure 35. Transmission co-efficient (radial coordinate) as a function of phonon frequency (colormap) and phonon incidence angle (azimuthal coordinate) for transverse and longitudinal phonons incident on a Si/Ge interface with interfacial roughness as η = 0.10 nm, 0.25 nm and 0.45 nm.

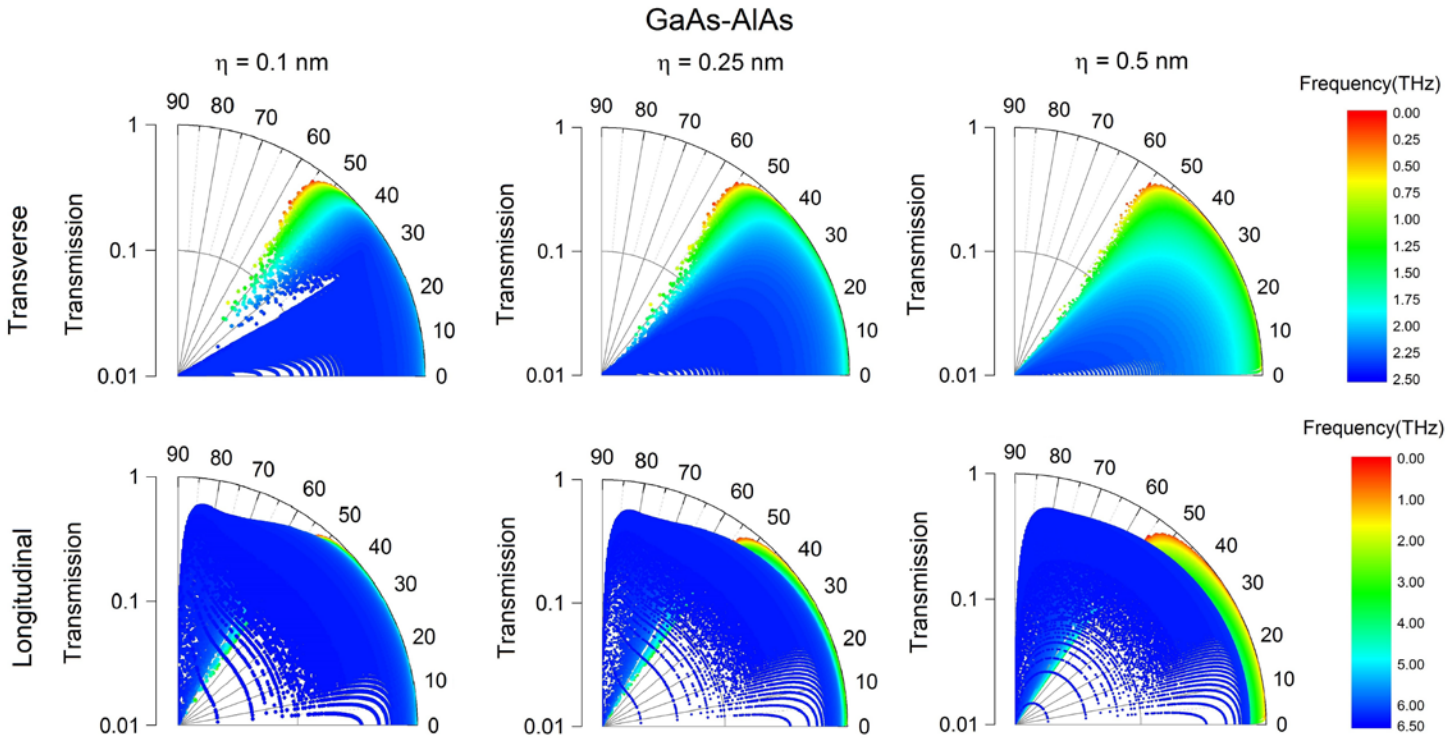

Figure 36. Transmission co-efficient (radial coordinate) as a function of phonon frequency (colormap) and phonon incidence angle (azimuthal coordinate) for transverse and longitudinal phonons incident on a GaAs/AlAs interface with interfacial roughness as η = 0.10 nm, 0.25 nm and 0.50 nm.

First, we have presented the variation of the transmission co-efficient of thermal phonons incident from Ge on a Si-Ge interface while the various frequencies have been demarcated using a colormap. We notice that with decreasing roughness transmission increases, allowing higher frequencies to have larger transmission and thereby the area shaded in blue becomes larger. We also notice that as frequency increases, critical angle for transmission decreases. This is evident from the fact that a larger wavelength color from the colormap envelops a lower wavelength color (for instance, green area envelops blue area, yellow area envelops the green area and so on). The reason for this phenomenon is a faster reduction in group velocity of Si phonons vs group velocity of Ge phonons as the wave vector approaches the Brillouin zone edge. In order to analyze the impact of acoustic and dispersion mismatch, we extend the analysis to GaAs-AlAs which have a lower acoustic and dispersion mismatch than Si-Ge. Analogously, in Figure 36, we show the transmission co-efficient variation for an AlAs-GaAs interface where phonon are incident from GaAs. We find that the transverse polarization has a critical angle for transmission ~58^{o} while for the longitudinal polarization, there is no critical angle, with transmission taking place for all angles. This can be understood from the fact that longitudinal dispersion relations of GaAs and AlAs intersect at a frequency f_0 ~ 6.3 THz which allows for phonons of that frequency to transmit at any angle since the same k-vector couples across the interface. We observe a trend similar to the Si-Ge case with changing roughness for the transverse polarization.

From the above discussion, we recognize that transmission coefficient as defined in Eq. 13, captures the dispersion and acoustic mismatch along with accounting for interface features such as roughness. We define an averaged transmission coefficient

(ATC) as a measure of coupling between two interfaces by taking a mean of the transmission coefficients over all wave-vectors ($\vec{k}$) which get transmitted. This parameter allows us to predict the possibility of coupling and quantify it which is essential to predict the change in thermal conductivity due to coupling. Thermal conductivity modification due to coupling in layered nanostructures plays a crucial role in performing thermal readouts which would need to be modified to account for coupling. Thermal conductivity changes also open a vast avenue to modulating thermal conduction which can be utilized in rational nanomaterial design frameworks such as enhanced thermal conductivity for heat dissipation from hotspots in a microelectronic circuit [139].

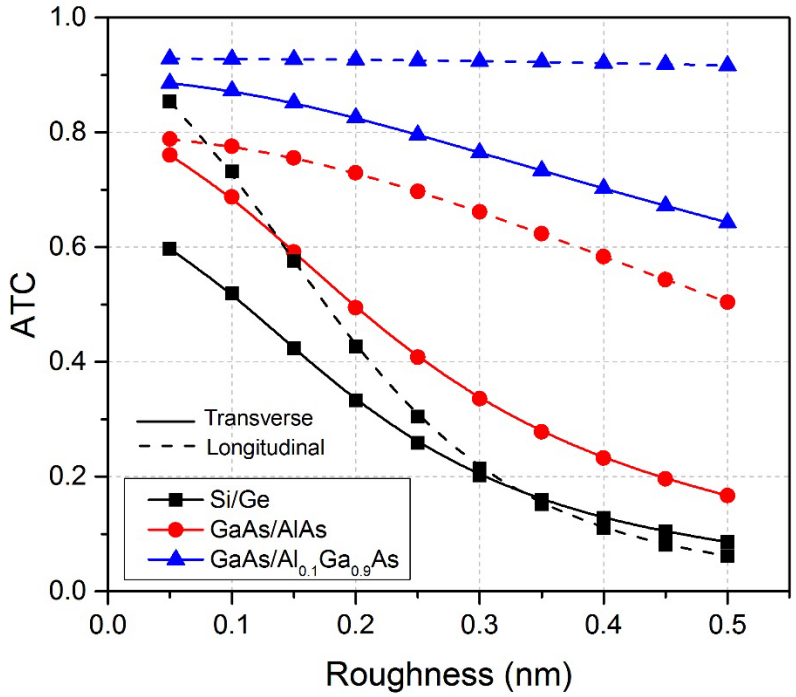

Figure 37. Averaged Transmission Coefficient (ATC) as a function of interfacial roughness for Si/Ge, GaAs/AlAs and GaAs/$Al_{0.1}Ga_{0.9}As$ interfaces for transverse and longitudinal polarizations.

In Figure 37, we observe a reduction in the ATC with increasing roughness, with generally larger ATC values for material pairs with closer dispersion and low acoustic impedance mismatch. This is in alignment with previous work in enhancing phonon transmission [140]. We also notice that a larger ATC is found for longitudinal phonons in contrast with transverse phonons. This is due to the non-zero group velocities at zone boundaries for longitudinal phonons as well group velocities being larger than transverse phonons. This also explains why the reduction in ATC for longitudinal phonons with increasing roughness is lesser compared to the case of transverse phonons. We notice that ATC for longitudinal phonons in the Si-Ge case is larger than the ATC for GaAs-AlAs case at lower roughnesses since longitudinal group velocities in Si-Ge are larger than GaAs-AlAs and there is a dominance of the interfacial characteristics in determining transmission rather than the acoustic impedance mismatch.

This analysis provides us with an in-depth understanding of the variation of transmission coefficient as a function of interfacial structural characteristics such as roughness as well as its dependence on acoustic impedance mismatch between different pairs of materials across an interface. This extensive comprehension furthers our understanding of interfacial coupling which impacts thermal conduction in nanoscale devices involving an interface between two materials.

3.5.2 Phonon Visualization

In section 3.4, we marked that an essential outcome of interlayer coupling in materials is the modulation in thermal conductivity taking place due to exchange of phonons across the interface during transmission. Thermal conductivity of the

nanostructure is obtained by averaging the localized thermal conductivity at every point within the nanostructure. To obtain the localized thermal conductivity, we need the distribution of phonons, in particular the deviation from the equilibrium distribution (Eqs. 1-3 and 7) [31]. Equivalently, this can be understood as distribution of MFPs of phonons arriving at a point [107]. In order to analyze this phonon MFP distribution, we provide a pictorial depiction of heat distribution and study how various factors such as boundary scattering and shadowing impact this distribution in a nanostructure. We present a comprehensive analysis by contrasting this spatial thermal energy distribution for Ge bulk, thin-film and thin-film on (Si) substrate configurations (see Figure 38 for schematic) to apprehend the impact of nanostructuring and interfacial coupling which collectively impact thermal conduction in film-on-substrate systems.

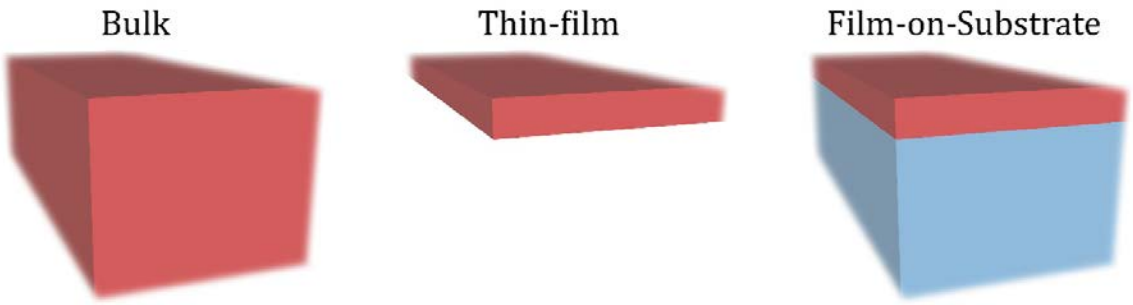

Figure 38. Schematic of bulk system, thin-film of Ge and (Ge) thin-film on (Si) substrate.

In this sub-section, we emphasize on visualizing this significant outcome of coupling and investigate the impact of varying roughness on the coupling-induced thermal conductivity enhancement.

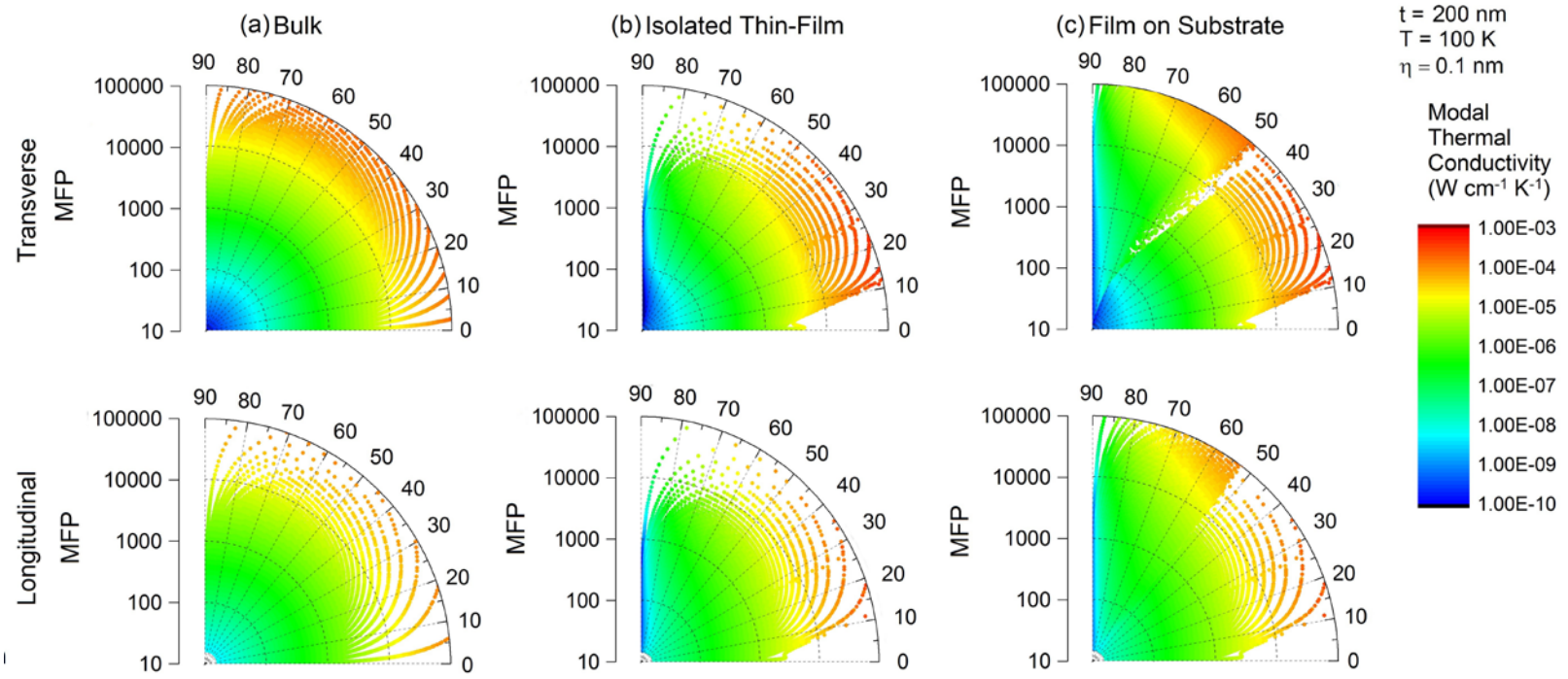

Figure 39. Spatial distribution of thermal energy in terms of thermal phonon MFPs (radial coordinate) and their angles subtended with x-y plane (azimuthal coordinate) for (a) bulk Ge, (b) Ge thin-film and (c) Ge thin-film on Si substrate systems, wherein the modal thermal conductivity contribution is given by the colormap. Here, *t* is the thickness of the isolated thin-film and the film atop the substrate and *η* is the surface roughness.

In Figure 39, we have shown a 2D visualization of spatial distribution of heat in terms of thermal phonon MFPs around a point in a bulk material, an isolated thin-film and a thin-film on substrate (FOS). We consider that the thermal gradient is in the x-direction while the thin-film is bounded in the z-direction. In these log-polar plots, we have depicted the phonon MFP along the radial direction while the polar angle captures the direction of propagation of phonons in terms of angle with the x-y plane (90˚- incidence angle). The color of a point on the plot, indicates the amount of heat carried by the phonon originating there and terminating at the origin. The color of points further away from origin is darker indicating that more heat is carried by phonons away from the point which can be understood from the fact that they have larger MFPs. We observe that for the bulk case in Figure 39a, the phonon MFP distribution arriving at a point is radially symmetric as expected since there is no directional preference within a bulk material. For the case of thin-films, the spatial thermal distribution would vary depending on the location within the thin-film. For a comparative analysis with the bulk case, we have averaged the distribution for 20 uniformly distributed points in the z-direction and plotted the MFP distribution in Figure 39b. We observe in Figure 39b that for small angles with x-y plane, there is a severe MFP reduction. This can be attributed to shadowing since at small angles with x-y plane, the phonons tend to propagate increasingly parallel to the thin-film surface and they interact with a significantly reduced area of the surface. This causes a drastic reduction in the specular reflection coefficient, thereby reducing MFPs of phonons. On the other hand, for phonons propagating at larger angles, boundary scattering due to finite-size effects cause a reduction in the MFPs. This reduction is seen across a broad range of angles and thus, the resultant conductivity is smaller than bulk values. In order to examine the impact of

interlayer coupling, we investigate the phonon MFP distribution in the FOS architecture. For the case of Ge on Si FOS in Figure 39c, we observe larger MFPs for phonons with incidence angle (90˚ – polar angle) less than the critical angle in transverse and longitudinal polarizations. We also notice a darker shade (more towards red) for these phonons which implies increased thermal conduction. These are evident indicators of thermal conductivity enhancement due to phonon injection from substrate as a consequence of interfacial coupling. We note that the MFP reduction due to shadowing is still significant, since the critical angle is small. We remark that the overall thermal conductivity in the FOS can exceed that of the bulk material which is the case while contrasting Figure 39a and Figure 39c. The high density of dark shades corresponding to long MFP phonons that show up in Figure 39c for angles less than the critical angle contribute to an enhancement beyond the bulk thermal conductivity. This finding has a crucial significance in enabling swift heat removal in microelectronic and optoelectronic devices, thereby improving their efficiency.

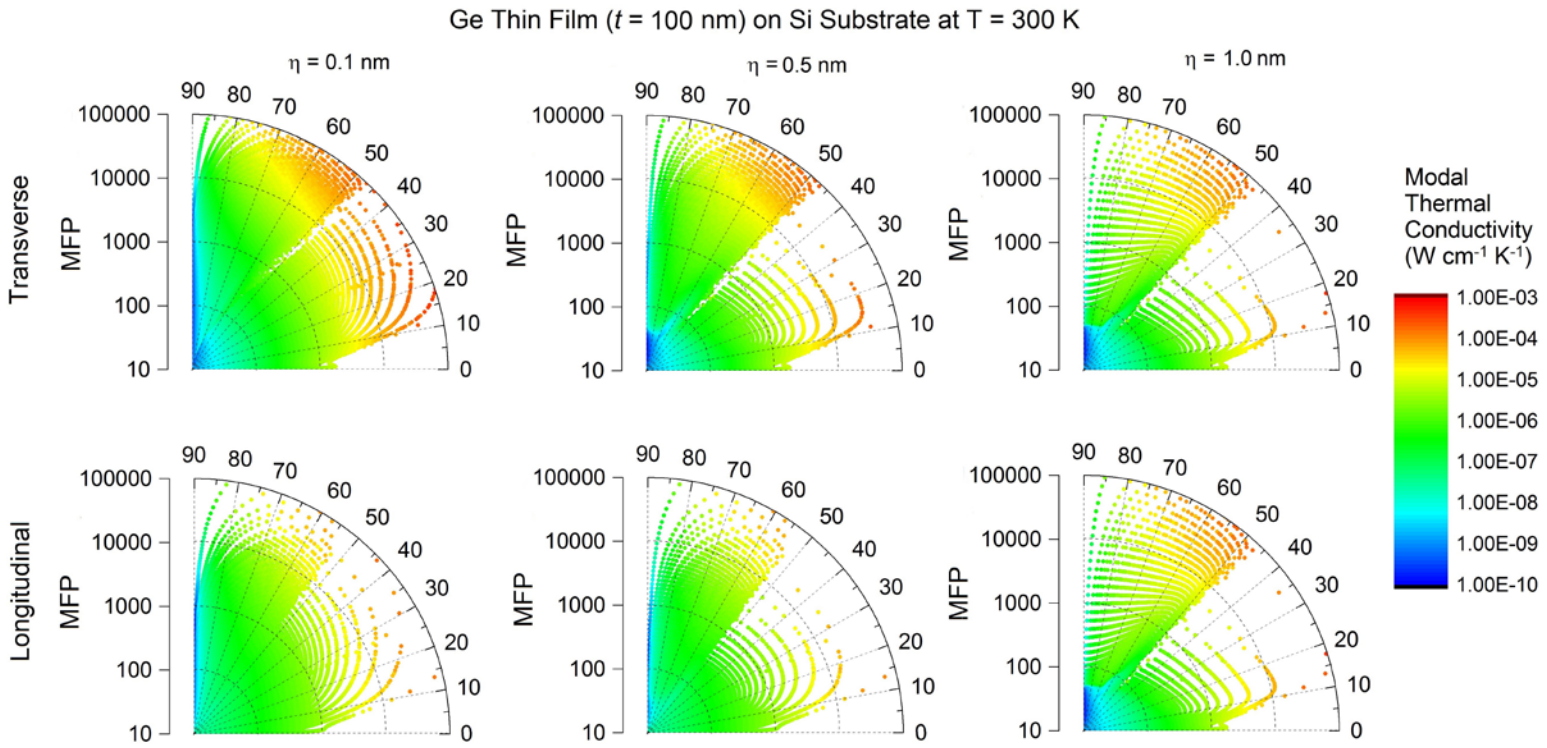

Figure 40. Spatial distribution of thermal energy in terms of thermal phonon MFPs (radial coordinate) and their angles subtended with x-y plane (azimuthal coordinate) for Ge thin-film on Si substrate systems with interfacial roughnesses as η = 0.1 nm, 0.50 nm and 1.00 nm, wherein the modal thermal conductivity contribution is given by the colormap.

In Figure 40, we demonstrate a visual representation of the impact of changing roughness on the spatial distribution of thermal phonon MFPs in Ge on Si FOS architectures. We observe a reduction in the density of points plotted with increasing interfacial roughness from $\eta = 0.1$ nm to $\eta = 1.0$ nm, which is indicative of reduction in MFPs. We notice that with increasing the interfacial roughness there is a large reduction in the MFPs of phonons which have propagation angles smaller than the critical angle of incidence. This can be attributed to the fact that these phonons do not engage in coupling and undergo reduction owing to boundary scattering. On the other hand, we detect a smaller reduction in MFP for phonons having larger propagation angles since phonon injection from substrate can compensate for enhanced diffusive scattering. We also examine the temperature dependence of the spatial distribution of heat in a nansostructure considering analogous visualizations for an $Al_{0.1}Ga_{0.9}As$ thin-film of thickness $t = 1000$ nm on GaAs substrate and interfacial roughness $\eta = 0.1$ nm. In Figure 41, we provide the heat distribution in the $Al_{0.1}Ga_{0.9}As$ on GaAs FOS systems for temperatures varying from T = 100 K to T = 500 K for both transverse and longitudinal phonon polarizations. In Figure 41, we discover how the MFP distribution shrinks towards lower MFPs with increasing temperature. We observe clear reductions in the maximum phonon MFP and modal thermal conductivity contributions which can be attributed to the rising phonon scattering rate with increasing temperature. Note that, we do not encounter a clear signature of MFP reduction due to shadowing since phonon injection from GaAs substrate dominates even at low angles with x-y plane due to similar dispersion relations and low acoustic impedance mismatch which wasn't the case in Ge on Si FOS systems. Nevertheless, the asymmetric thermal contribution profile is indicative of significant deviation from the bulk profile.

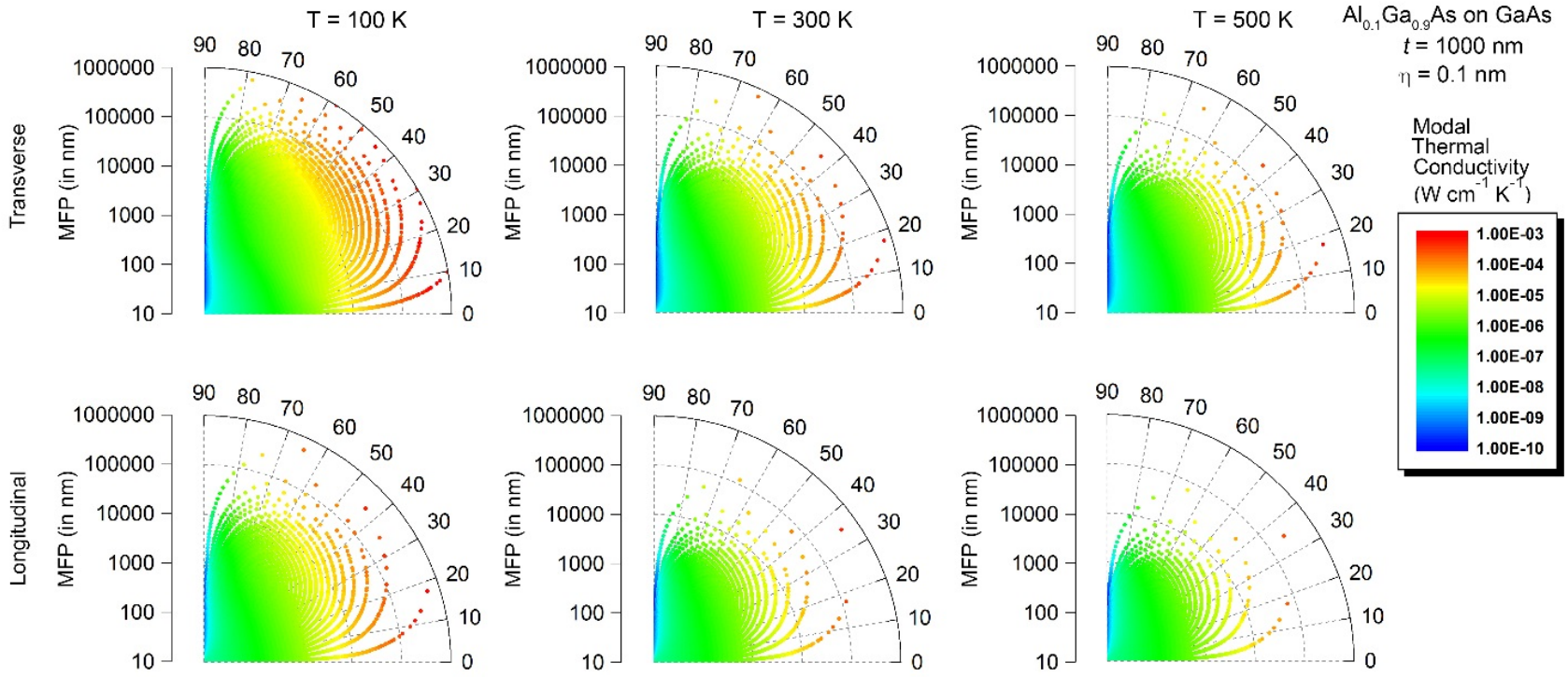

Figure 41. Spatial distribution of thermal energy in terms of thermal phonon MFPs (radial coordinate) and their angles subtended with x-y plane (azimuthal coordinate) for $Al_{0.1}Ga_{0.9}As$ thin-film on GaAs substrate systems at temperatures T = 100 K, 300 K, and 500 K, wherein the modal thermal conductivity contribution is given by the colormap.

These 2D visualizations of phonon MFPs and corresponding thermal energy distributions provide localized insights into how interfacial coupling impacts thermal conduction in nanostructures. They provide an understanding of how phonons MFPs are spatially distributed which can be leveraged to modulate thermal conduction by implementing scattering mechanisms which can target phonon MFPs at various length scales [35].

CHAPTER 4.

PRELIMINARY ANALYSIS OF THERMAL PHONON WAVE PHENOMENON

In this Chapter, we briefly analyze the possibility of wave effects for nanostructures with periodic boundaries such as superlattices. Thermal phonon wave effects is an emerging research area that has captured significant interest in recent years [33,34,36,63,116]. For certain structures and temperatures, wave effects can modify phonon dispersion relations, opening opportunities to control phonon group velocities and density of states, which are critical transport properties affecting the thermal conductivity [63]. The coherent interference of multiple reflected phonons originating from the phase-preserving specular scattering at interfaces is the basic mechanism for the appearance of wave effects. It is important to highlight that thermal phonons are incoherent in the sense that they are formed by random vibrations of the atomic lattice. Although thermal phonons are incoherently generated, wave effects due to coherent interference refer to wave effects arising from the coherent interference of phonons with themselves after reflection and transmission at multiple surfaces or interfaces.

4.1 Types of Phonon Wave Effects

Semiconductor superlattices are excellent candidates for investigating thermal phonon wave effects due to their nearly atomic flat interfaces which increase the amount of specular scattering. Fundamentally, specular scattering of phonons in superlattices can give rise to two distinct wave effects – thermal band gaps and quantum confinement –

depending on the phonon energy distribution and trajectories. Specifically, for 'layer-restricted' phonons, multiple reflections at the confining surface boundaries of the layer can interfere coherently and give rise to "quantum confinement" effects (formation of phononic quantum wells) and on the other hand, for 'extended' phonons, multiple reflections at the interfaces between the layers of the superlattice can interfere coherently and give rise to "thermal band gaps". We note that in both cases the net effect is the modification of the phonon dispersion relations and thus the velocities and density of states of thermal phonons. (Note that, specific conditions for development of phonon quantum confinement effects in terms of film thickness, roughness and temperatures have been analyzed in Ref. [141].) Since a complete description of wave effects necessitates accounting for thermal band gaps and quantum confinement, it is critical to predict the fraction of heat which is 'extended' in contrast to 'layer-restricted' in order to manipulate the extent of thermal band gaps and quantum confinement respectively. For instance, in section 3.1.1 and 3.1.2, we have highlighted the fraction of heat conducted by layer-restricted and extended phonons respectively as a function of the superlattice structural features such as period length and interfacial roughness. In a Si-Ge superlattice with period length d=100nm, roughness η = 0.1 nm, and f_{Si}=0.75–f_{Ge}=0.25, the relative amount of heat carried by extended phonons is close to 30%. This is therefore the most favorable superlattice for the development of thermal band gaps in the sense that 30% of the heat is carried by phonons that see multiple interfaces. We note, however, that for strong coherent interference effects in Si-Ge superlattices, phonons must see at least ten interfaces[142,143] . We calculated the fraction of heat carried by phonons that travel through five superlattice periods (i.e. 10 interfaces) and found that it is reduced to 16%.

This small amount is one reason why strong wave effects and a minimal thermal conductivity are not observed for in-plane transport. We would like to clarify that bulk phonon mean free paths in Si and Ge can be relatively long but they are strongly reduced in superlattices due to surface scattering. As a result, only a small fraction of phonons can travel across multiple layers when the Si-Ge superlattice interfaces are rough and thus, there are negligible wave effects.

4.2 Pathways for Accentuating Wave Phenomenon

We note that coherent interference of thermal phonons occurs when phonon wavelengths are comparable to the characteristic length of the structure and phonon mean free paths (MFP) are large enough for the formation of forbidden frequency ranges. In superlattices, one of the conditions for the emergence of wave effects is that phonon wavelengths are comparable to the superlattice period $d = a + b$ (i.e. Bragg's law $\lambda \sim 2d$). Since in typical semiconductors at T=300K most of the heat is carried by phonons with wavelengths λ=1-10nm [114], wave effects should emerge for period lengths scales smaller than 10nm. In particular, Bragg's law establishes that the superlattice period for strong wave effects should be d~2-3nm [116]. This is fully consistent with first-principle simulations and experiments which report that strong wave effects occur at periods p~3-4nm [33,64]. Accounting for the amount of continued thermal conduction along with wavelength and MFP conditions is crucial towards framing strategies that can enhance the possibility of wave effects in periodic nanostructures.

We highlight some methodologies that can intensate the impact of wave phenomenon on thermal conduction in superlattices. For 'layer-restricted' phonons, the

strength of quantum confinement is predicted to increase with acoustic impedance contrast between the SL constituent materials due to an increasing fraction of phonons becoming layer-restricted [118]. On the other hand, for 'extended' phonons, cross-plane configuration is expected to have stronger wave effects. This can be understood through the following reasoning. When the temperature gradient ∇T is normal to the layers, layer-restricted phonons travel perpendicularly to ∇T while extended phonons (which can be subject to coherent interference) move along ∇T. This is in direct contrast to in-plane phonon transport. As a result, for cross-plane phonon transport, phonons that can be subject to coherent interference carry a more significant part of the heat, and wave effects may become significant. Cross-plane phonon wave effects have been reported theoretically using wave theory[65] and molecular dynamics[70,71] and experimentally in oxide superlattices[33]. Other techniques of enhancing thermal phonon wave effects involve modulating thermal conduction towards low frequency phonons through the use of alloying, impurity and structural defects, nanoparticles and regulating temperature [35,116,117]. In alloys, the mass-difference in the atomic lattice gives rise to diffuse scattering of short-wavelength phonons, restricting their ability to carry heat [116,117,144]. As a result, the relative amount of heat carried by long-wavelength phonons increases with respect to the pure materials. Phonons with long wavelengths (i.e. low frequencies) have large mean-free-paths and are more prone to undergo specular interface scattering, which increases the likelihood of developing extended modes and wave effects[63]. At low temperatures, the proportion of heat carried by long-wavelength phonons increases but for reasons different to those in alloying. In this case, high-frequency phonons are not thermally excited and therefore do not carry heat. The heat spectrum is

thus made of long-wavelength phonons, which are likely to scatter specularly at interfaces and develop extended modes and wave effects. Wave effects at low temperatures have been recently demonstrated experimentally in two-dimensional periodic porous materials [34,60].

It is important to highlight that wave effects would appear for certain structures under certain conditions, and full characterization of the structures in terms of periodicity *and* interface roughness as well as temperature needs to be investigated to clearly establish when wave effects on thermal transport can develop in engineered nanosystems. Also, a comprehensive analysis would require a clear demarcation of the fraction of thermal conduction which is coherent and that which is incoherent and therein, highlighting the impact of coherent interference based wave effects on thermal conduction.

CHAPTER 5.

CONCLUSION – SUMMARY AND OUTLOOK

5.1 Summary of Findings

A key element to understanding and predicting thermal transport in multilayered nanostructures is the phonon interfacial interaction mechanism. In this thesis, we have implemented a thorough treatment for the interfacial interaction by providing a rigorous analysis accounting for characteristics of phonons (frequency and incident angle), materials adjacent to the interface (acoustic impedance, dispersion mismatch) and interfacial structural characteristics (roughness and correlation length). We integrate this interfacial scattering mechanism along with a semi-classical transport formalism, namely the Boltzmann Transport Equation and study the thermal transport in layered semiconductor nanostructures composed of Si/Ge, GaAs/AlAs and their alloys.

5.1.1 In-plane Heat Conduction in Superlattices

We commence with studying thermal conduction in Si/Ge and GaAs/AlAs based superlattices in the in-plane thermal configuration and we move beyond computing thermal conductivity and also determine the thermal energy distribution based on phonon trajectories within the superlattice. We provided a detailed description of the amount of thermal energy carried by phonons restricted to a layer and those which are extended over multiple layers in the superlattice and denote the two categories as ‘layer-restricted’ and ‘extended’ phonons respectively. We further segregate the ‘layer-restricted’ phonons depending on the interfacial interaction mechanisms into TIR-BSM, TIR-AIM and MFP

reduction and study their dependence on structural parameters of the superlattice such as period length and roughness. The results in this microscopic analysis provide new tools to manipulate the proportion of heat that is conducted in a single or multiple layers and can be utilized for the rational design of thermal systems. We also quantified the amount of heat that continually transmits in a superlattice after N reflections and transmission events for phonons and investigate the importance of this metric in being an essential step towards understanding coherent phonon effects in superlattices. We performed a spectral analysis by determining the frequency and MFP spectra and their dependence on period length and roughness. The frequency and MFP spectra can be utilized to design thermal devices based on superlattices as material platforms, as they allow to determine ballistic vs. diffusive and coherent vs. incoherent heat conduction regimes. The spectral analysis also provides guidelines on tailoring thermal conduction in devices and materials requiring a certain band of frequencies or MFPs. We supplemented this thermal analysis with a finite-sized nanostructure analysis to provide pathways to extend the work to real-word applications wherein superlattices do not have an infinite number of periods. Additionally, we also provided conductivity predictions for varying well and barrier widths in GaAs/AlAs alloy-based superlattices. These findings can yield crucial inputs towards designing nanostructures with tailored thermal properties especially for optoelectronic applications.

5.1.2 Cross-plane Transport in III-V Superlattices

In contrast with the in-plane thermal conduction, we also evaluated thermal conduction in the through-plane configuration in III-V semiconductor superlattices. In addition to a structural, spectral and finite-sized-nanostructure thermal transport analysis, we contrasted the in-plane and through-plane conductivities and determined the anisotropy.

We studied the anisotropy as a function of period length and roughness. We found that, in general, interfacial scattering has a stronger effect on thermal conduction in the cross-plane configuration. We also observed a minima in the anisotropy as a function of roughness, due to the differential impact of interfacial scattering in the two configurations. The understanding of anisotropy can be applied to various thermal material designs, for instance, directional heat spreaders which require different rates of thermal conduction in different directions. We also explored the impact of alloying on the thermal conductivity and spectra of the superlattices and contrasted it with those of the pure superlattices. We found a shift towards lower frequencies due to alloying reducing the phonon relaxation time for high frequency phonons. We also performed a modal thermal conductivity analysis i.e. an in-depth study of the quantity of heat carried by different phonon modes and polarizations by plotting modes as a function of frequency and incidence angle. We determined the phonon energy distribution as well as trajectories within the superlattice.

5.1.3 Film-on-Substrate Architecture

A detailed investigation of interfacial phonon interaction led us to uncovering the phonon injection mechanism wherein thermal phonons originating in a medium coupled across an interface into another medium resulting in modulation of thermal conductivity of the two media. We inspected how interfacial and material properties as well as structural dimensions influence the effectiveness of the phonon injection mechanism. Next, we delved into an important application of phonon interlayer coupling – thin-film on substrate architecture. We quantitatively predicted how the phonon injection mechanism results in a significant modulation of thermal transport in a thin-film grown on substrate vis-à-vis an isolated thin film. In contrast to established thermal transport in nanomembranes, we

showed that it is possible to increase the in-plane thermal conductivity of a thin film by placing it on top of an appropriate substrate and that the thermal conductivity increases with decreasing spacing. In an unconventional result, we noted an increasing thermal conductivity with reducing thin-film thickness which can be attributed to the increasing volume fraction available for phonon injection. An important outcome was to note that thermal conductivity could be enhanced beyond the bulk value for that material which can have critical consequences in enhancing the efficiency of microelectronic and optoelectronic devices requiring swift thermal dissipation/removal of heat. Phonon injection-based thermal conductivity enhancement arises from an interplay of acoustic impedance mismatch, materials thermal transport properties, interfacial characteristics, and thickness of thin film atop the substrate. The spectral analysis for the FOS architecture provides that low frequency and large MFP phonons experienced enhancement to a larger extent owing to larger transmission coefficient at lower frequencies. The thermal conductivity enhancement spectra indicated that with increasing roughness, the trade-off between thermal conductivity reduction due to boundary scattering and that due to reduction in transmission could lead to a maxima in thermal conductivity enhancement for a specific roughness. Materials with closer dispersion relations yielded thermal conductivity enhancement over a broad MFP range when contrasted to materials with more distinct dispersion relations. The analysis of the FOS architectures suggests that experimental measurement of thermal conductivity of thin-films needs to account for thermal coupling between thin film and substrate and the consequent conductivity modification. This provides for the need to develop a rigorous conductivity read-out model for experiments. The FOS is a fundamentally important architecture which forms the basis

for numerous nanostructured semiconductor applications. Understanding and controlling thermal transfer for FOS opens new avenues for enhancing the efficiency of optoelectronic devices such as photodetectors and lasers.

5.1.4 Interfacial Coupling Analysis

We investigated the interlayer coupling between two materials while rigorously accounting for interfacial characteristics and accounting for dispersion and acoustic mismatch through a detailed mode-wise analysis of the transmission co-efficient between Si/Ge and GaAs/AlAs. We studied the impact of varying interfacial roughness and quantified the interlayer coupling by formulating an averaged transmission coefficient for interfaces. We investigated interfaces between Si/Ge, GaAs/AlAs and GaAs/$Al_{0.1}Ga_{0.9}As$, thus exploring the impact of varying acoustic impedance mismatch across an interface. These interfaces are widely found among nanostructures such as superlattices, FOS configurations and nanomembranes which find applications as photodetectors, lasers etc. We found that higher acoustic impedance mismatch led to interfacial features such as roughness having a significant role in determining transmission and coupling across media. We developed a microscopic comprehension of the coupling phenomenon through visualizing its immediate consequence of thermal conductivity modulation. Specifically, we examined thermal conductivity enhancement in FOS architectures through visualizing a spatial distribution of thermal phonon MFPs reaching a point within the nanostructure. We demonstrate clear signatures of thermal conductivity enhancement beyond the thermal conductivity of an identical isolated thin film and also the bulk materials under specific conditions. We provided visual illustrations of the impact of varying interfacial roughness and temperature on the spatial distribution of phonon MFPs. The analysis presented allows

us to quantify interlayer coupling which is vital in providing accurate thermal conductivity measurements and opens new avenues to modulation in thermal conductivity at the nanoscale.

5.1.5 Thermal Phonon Wave Effects

We outline the importance of studying superlattices in context of investigating thermal phonon wave phenomenon by distinguishing the two types of wave effects that phonons can exhibit in a superlattice structure. We classify them according to the phonon trajectories – 'layer-restricted' phonons can coherently interfere to give rise to quantum confinement or phononic quantum wells whereas 'extended' phonons can interfere to develop thermal band gaps. We highlight the importance of comprehending the energy distribution and the percentage of thermal energy that continues upon multiple interactions with the interfaces as being vital determinants of the impact of wave effects on thermal conduction. We provide a broad range of methodologies that can be implemented to enhance the significance of wave effects in superlattice nanostructures. These included cross-plane transport, use of alloying, impurity and structural defects and low temperature regimes. We emphasized that an accurate analysis of wave effects needs the specification of various structural and physical characteristics such as periodicity, roughness and temperature. Additionally, since thermal conduction consists of a broad spectrum of phonons, it would be of fundamental interest to quantify the fraction of heat that is subject to coherent wave effects and that which propagates through incoherent phonon interactions.

5.2 Future Explorations and Outlook

The analysis presented in this work opens up new avenues and challenges in nanoscale thermal transport that would address further real-word applications and also deepen the fundamental understanding of phonon transport.

5.2.1 Finite-sized Multilayers with Varying Layer Widths

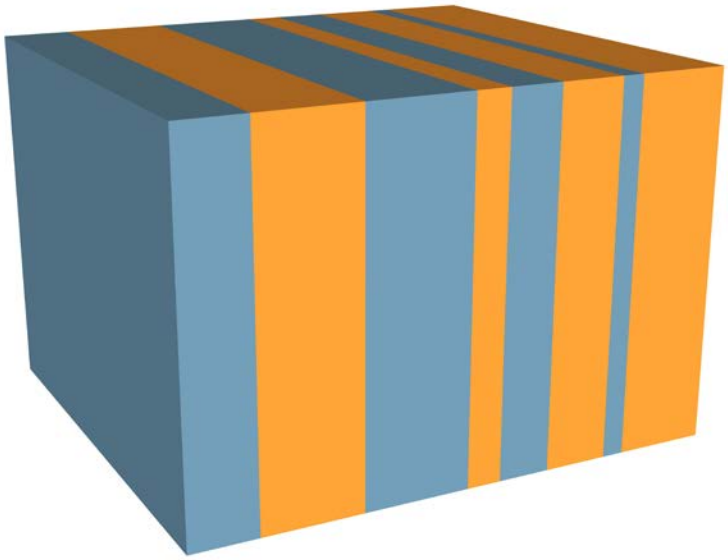

Figure 42. Schematic of a random multilayer consisting of alternating layers made of the same material.

One of the ubiquitously found layered nanostructures is a multilayer with varying layer widths (Figure 42). This structure finds a plethora of optoelectronic applications such as QCLs, QWIPs, etc. [14,18,19]. An in-depth analysis and control of thermal transport in the cross-plane configuration for these devices is often crucial to enhancing efficiencies [24,25,30]. Additionally, such multilayer structures are also found in thermoelectric applications as well. An investigation of optimized structures for thermoelectric generators provided that Gaussian distribution of barrier widths in a multilayer structure resulted in

highest thermoelectric efficiency at maximum output power [145]. A fundamental study looking to go beyond the random-alloy limit of thermal conductivity also found that thermal conductivity of a random multilayer was lower than that of a superlattice or alloy made of similar material composition [146]. Thermal transport analysis in these structures requires extending the interfacial interaction analysis, specifically the interfacial boundary conditions, and the use of principle of detailed balance. Typical devices with such structures have 10s-100s of interfaces and thereby, a rigorous computation of transport would require solving N x N matrices where N is of the order 10^1-10^2. Thus, a parallel processing algorithm to solve such huge matrices would be needed so that a detailed modal analysis can also be incorporated. It would also be intriguing to contrast these results with superlattices and study the anisotropy in multilayer structures as they could provide crucial inputs for thermal management in devices.

5.2.2 Film-on-Substrate – Cross Plane Configuration

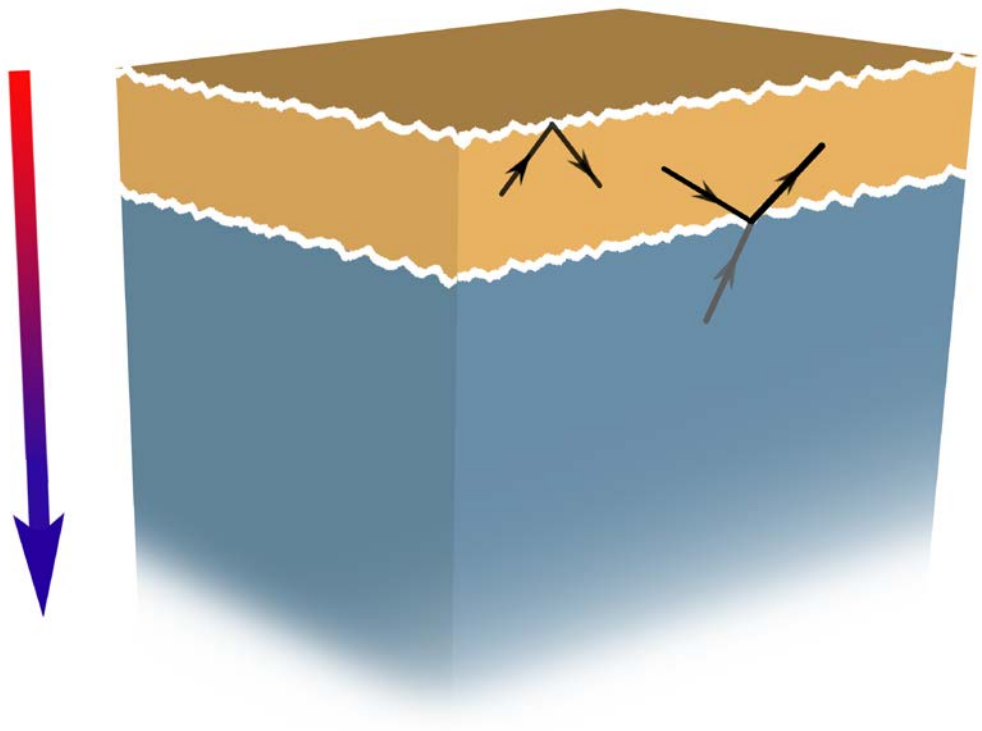

Figure 43. Schematic of cross-plane thermal transport in a film-on-substrate architecture. The arrow on the left shows the direction of the thermal gradient. The arrows in the figure show the phonon interactions influencing transport in the thin-film.

In section 3.3, we examined thermal transport properties in film-on-substrate architectures when the gradient was applied parallel to the interfaces between the thin-film and substrate. The similar architecture finds a plethora of application when the gradient is applied perpendicular to the interface as well (Figure 43). Not only in optoelectronic devices such as LEDs and photodetectors [89-92], but also experimental readout procedures from thermal measurement setups such as Time-Domain Thermoreflectance (TDTR) and Frequency-Domain Thermoreflectance (FDTR) employ the FOS nanostructure in the cross-plane configuration [94,147,148]. Thereby, this problem is crucial for achieving better devices and optimizing experimental readout techniques so that

they account for the substrate-film coupling. This problem can be addressed by integrating the cross-plane formalism for thermal transport in nanomembranes [149] with interlayer coupling mechanism [107] and accounting for the fact that substrates are much thicker than thin-films grown atop. A challenge to be resolved is the loss of structural symmetry which is in contrast with the configurations in nanomembranes and superlattices.

5.2.3 Incorporating Wave Effects in the Boltzmann Formalism

A crucial step in advancing the comprehension of phonon wave effects is to incorporate them within the Boltzmann transport formalism. The advantage of incorporating into a continuum formalism is the length-scaling associated i.e. one can quantitatively estimate the impact of wave effects at various characteristic length scales unlike atomistic formulations where in the simulation cell-size if often limited by computing abilities. The key lies in considering the dispersion relation and density of states modification while simultaneously accounting for phonon scattering due to interfacial roughness. A meticulous understanding of thermal phonon wave phenomenon necessitates a deeper analysis of the extent of dispersion relation modification that occurs when interfaces are rough. Current literature [36,60,64] discusses wave-like phonon transport only for perfect interfaces or low temperatures wherein the interfacial roughness is very small vis-à-vis the phononic wavelengths. The challenge is to develop a formalism wherein the approximation of perfect interfaces can be relaxed.

Additionally, a broad spectrum of phonon wavelengths and mean free paths implies that there could be partial coherent and partial incoherent transport and thus it would be crucial to estimate the fraction of thermal conduction that is coherent and incoherent and

characterize the parameters that would indicate the dominance of either regime. A further spectral analysis would provide insights on which frequencies, wavelength and MFPs of phonons are more subject to coherent wave effects. This would help in further controlling the extent of thermal conduction by manipulating the fraction and properties of phonons which are subject to wave effects.

Current studies in the literature indicate that a minimum in thermal conductivity of superlattices (with increasing period length) is attributed to wave effects occurring due to phonons interfering after reflection and transmission from multiple interfaces i.e. formation of “thermal band gaps”. It would be insightful to explore experimental methodologies and signatures that can capture the impact of “quantum confinement” (wave effects due to transport of phonons in a single layer) in multilayered nanostructures. In these investigations, it will be essential to distinguish ballistic transport from coherent transport when it comes to looking for experimental signatures of coherent transport.

5.2.4 Experimental Validation of Thermal Transport Characteristics

The thermal transport characteristics predicted in this work can be subject to experimental validation. Of vital interest would be experimental techniques that can provide thermal spectra such as the MFP and frequency spectra. Furthermore, our predictions of in-plane thermal transport behavior in FOS structures are unconventional (especially $Al_{0.1}Ga_{0.9}As$ films on GaAs substrates show increasing conductivity with reducing thickness) and it would be vital to validate them experimentally. This would have consequential implication on thermal measurements’ experimental readout techniques. Typical readout techniques for thin-films grown on substrates do not account for interlayer

coupling. We posit that for materials with similar dispersion relations and low interfacial roughness, interlayer coupling would impact thermal conduction and as suggested by the predictions in section 3.4.1, they can exhibit trends which are in contradiction to the trend for isolated thin-films.

APPENDIX A. PERMISSIONS FOR USE OF COPYRIGHTED MATERIALS

Portions of this thesis have originally been published in the below mentioned publications. Permissions for reproduction of the content have been obtained and we would like to provide the following acknowledgements.

1. "Phonon Surface Scattering and Thermal Energy Distribution in Superlattices" (2017), *Scientific Reports*, Vol. 7 (5625). Content has been reproduced under a CC BY 4.0 License. A copy of the license can be found at http://creativecommons.org/licenses/by/4.0/.
2. "Unconventional Thermal Transport in Thin Film-on-Substrate Systems" (2018), *Journal of Physics D: Applied Physics*, Vol. 51, No. 36 (365302). Content has been reproduced with permission from IOP Publishing. The original article can be found at https://doi.org/10.1088/1361-6463/aad533
3. "Cross-Plane Heat Conduction in III-V Semiconductor Superlattices" (2019), *Journal of Physics: Condensed Matter*, Vol. 31, No. 34 (345301). Content has been reproduced with permission from IOP Publishing. The original article can be found at https://doi.org/10.1088/1361-648X/ab2172
4. "Analysis of In-Plane Thermal Phonon Transport in III-V Compound Semiconductor Superlattices" (2018), *Nanoscale and Microscale Thermophysical Engineering*, Vol. 22, No. 3 (239-53). "This is an **Accepted Manuscript** of an article published by Taylor & Francis in ***Nanoscale and Microscale Thermophysical Engineering*** on July 9, 2018 available online at the Taylor &

Francis Ltd web site: https://tandfonline.com/doi/full/10.1080/15567265.2018.1486929 ."

5. "Enhancing Thermal Transport in Layered Nanomaterials" (2018), *Scientific Reports*, Vol. 8 (1880). Content has been reproduced under a CC BY 4.0 License. A copy of the license can be found at http://creativecommons.org/licenses/by/4.0/.

REFERENCES

[1] Cahill, D G *et al.* Nanoscale Thermal Transport. *Journal of Applied Physics* **93** 793 (2003)

[2] Cahill, D G *et al.* Nanoscale Thermal Transport. II. 2003–2012. *Applied Physics Reviews* **1** 011305 (2014)

[3] Rogalski, A Infrared Detectors: Status and Trends. *Progress in Quantum Electronics* **27** 59 (2003)

[4] Gmachl, C, Capasso, F, Sivco, D L, and Cho, A Y Recent Progress in Quantum Cascade Lasers and Applications. *Reports on Progress in Physics* **64** 1533 (2001)

[5] Venkatasubramanian, R, Siivola, E, Colpitts, T, and O'quinn, B Thin-Film Thermoelectric Devices with High Room-Temperature Figures of Merit. *Nature* **413** 597 (2001)

[6] Shi, L *et al.* Evaluating Broader Impacts of Nanoscale Thermal Transport Research. *Nanoscale and Microscale Thermophysical Engineering* **19** 127 (2015)

[7] Snyder, G J and Toberer, E S Complex Thermoelectric Materials. *Nat Mater* **7** 105 (2008)

[8] Aubain, M S and Bandaru, P R Determination of Diminished Thermal Conductivity in Silicon Thin Films Using Scanning Thermoreflectance Thermometry. *Applied Physics Letters* **97** 253102 (2010)

[9] Ju, Y S and Goodson, K E Phonon Scattering in Silicon Films with Thickness of Order 100 Nm. *Applied Physics Letters* **74** 3005 (1999)

[10] Majumdar, A Microscale Heat Conduction in Dielectric Thin Films. *Journal of Heat Transfer* **115** 7 (1993)

[11] Sellan, D P, Turney, J E, Mcgaughey, A J H, and Amon, C H Cross-Plane Phonon Transport in Thin Films. *Journal of Applied Physics* **108** 113524 (2010)

[12] Maldovan, M Micro to Nano Scale Thermal Energy Conduction in Semiconductor Thin Films. *Journal of Applied Physics* **110** 034308 (2011)

[13] Faist, J *et al.* Quantum Cascade Laser. *Science* **264** 553+ (1994)

[14] Sirtori, C *et al.* GaAs/$Al_xGa_{1-x}As$ Quantum Cascade Lasers. *Applied Physics Letters* **73** 3486 (1998)

[15] Kuo, Y-H *et al.* Strong Quantum-Confined Stark Effect in Germanium Quantum-Well Structures on Silicon. *Nature* **437** 1334 (2005)

[16] Wood, T H *et al.* High-Speed Optical Modulation with GaAs/GaAlAs Quantum Wells in a P-I-N Diode Structure. *Applied Physics Letters* **44** 16 (1984)

[17] Wood, T H Multiple Quantum Well (MQW) Waveguide Modulators. *Journal of Lightwave Technology* **6** 743 (1988)

[18] Liu, H C *et al.* Gaas/Algaas Quantum-Well Photodetector for Visible and Middle Infrared Dual-Band Detection. *Applied Physics Letters* **77** 2437 (2000)

[19] Gunapala, S D *et al.* 9-um Cutoff 256x256 GaAs/$Al_xGa_{1-x}As$ Quantum Well Infrared Photodetector Hand-Held Camera. *IEEE Transactions on Electron Devices* **44** 51 (1997)

[20] Clames, J-Y *et al.* Device Simulation for GaAs⁄AlGaAs Superlattice Infrared Photodetector with a Single Current Blocking Layer. *Journal of Applied Physics* **97** 064910 (2005)

[21] S. Goswami, P B, J. Singh Wavelength Selective Detection Using Excitonic Resonances in Multiquantum-Well Structures. *IEEE Journal of Quantum Electronics* **27** 875 (1991)

[22] Kagawa, T, Kawamura, Y, Asai, H, and Naganuma, M InGaAs/InAlAs Superlattice Avalanche Photodiode with a Separated Photoabsorption Layer. *Applied Physics Letters* **57** 1895 (1990)

[23] Page, H *et al.* 300 K Operation of a GaAs-Based Quantum-Cascade Laser at $\Lambda \approx 9$ Mm. *Applied Physics Letters* **78** 3529 (2001)

[24] Kemp, A J *et al.* Thermal Management in Vertical-External-Cavity Surface-Emitting Lasers: Finite-Element Analysis of a Heatspreader Approach. *IEEE Journal of Quantum Electronics* **41** 148 (2005)

[25] Lindberg, H *et al.* Thermal Management of Optically Pumped Long-Wavelength Inp-Based Semiconductor Disk Lasers. *IEEE Journal of Selected Topics in Quantum Electronics* **11** 1126 (2005)

[26] Lorenzen, D *et al.* Micro Thermal Management of High-Power Diode Laser Bars. *IEEE Transactions on Industrial Electronics* **48** 286 (2001)

[27] Arik, M, Petroski, J, and Weaver, S, in *ITherm 2002. Eighth Intersociety Conference on Thermal and Thermomechanical Phenomena in Electronic Systems (Cat. No.02CH37258)*2002), pp. 113.

[28] Xiaowei, L *et al.* High-Saturation-Current InP-InGaAs Photodiode with Partially Depleted Absorber. *IEEE Photonics Technology Letters* **15** 1276 (2003)

[29] Paslaski, J S *et al.*, in *SPIE's 1996 International Symposium on Optical Science, Engineering, and Instrumentation* (SPIE, 1996), p. 10.

[30] Williams, K J and Esman, R D Design Considerations for High-Current Photodetectors. *Journal of Lightwave Technology* **17** 1443 (1999)

[31] Ziman, J M 1960 *Electrons and Phonons* (Oxford: Oxford University Press).

[32] Chen, G Thermal Conductivity and Ballistic-Phonon Transport in the Cross-Plane Direction of Superlattices. *Physical Review B* **57** 14958 (1998)

[33] Ravichandran, J *et al.* Crossover from Incoherent to Coherent Phonon Scattering in Epitaxial Oxide Superlattices. *Nat Mater* **13** 168 (2014)

[34] Zen, N *et al.* Engineering Thermal Conductance Using a Two-Dimensional Phononic Crystal. *Nature Communications* **5** 3435 (2014)

[35] Biswas, K *et al.* High-Performance Bulk Thermoelectrics with All-Scale Hierarchical Architectures. *Nature* **489** 414 (2012)

[36] Luckyanova, M N *et al.* Coherent Phonon Heat Conduction in Superlattices. *Science* **338** 936 (2012)

[37] Hochbaum, A I *et al.* Enhanced Thermoelectric Performance of Rough Silicon Nanowires. *Nature* **451** 163 (2008)

[38] Sondheimer, E H The Mean Free Path of Electrons in Metals. *Advances in Physics* **1** 1 (1952)

[39] Fuchs, K The Conductivity of Thin Metallic Films According to the Electron Theory of Metals. *Mathematical Proceedings of the Cambridge Philosophical Society* **34** 100 (2008)

[40] Khalatnikov, I and Adamenko, I Theory of the Kapitza Temperature Discontinuity at a Solid Body-Liquid Helium Boundary. *Soviet Journal of Experimental and Theoretical Physics* **36** 391 (1973)

[41] Swartz, E T and Pohl, R O Thermal Boundary Resistance. *Reviews of Modern Physics* **61** 605 (1989)

[42] Swartz, E T and Pohl, R O Thermal Resistance at Interfaces. *Applied Physics Letters* **51** 2200 (1987)

[43] Stoner, R J and Maris, H J Kapitza Conductance and Heat Flow between Solids at Temperatures from 50 to 300 K. *Physical Review B* **48** 16373 (1993)

[44] Lim, J *et al.* Quantifying Surface Roughness Effects on Phonon Transport in Silicon Nanowires. *Nano Letters* **12** 2475 (2012)

[45] Tian, Z, Esfarjani, K, and Chen, G Enhancing Phonon Transmission across a Si/Ge Interface by Atomic Roughness: First-Principles Study with the Green's Function Method. *Physical Review B* **86** 235304 (2012)

[46] Latour, B, Shulumba, N, and Minnich, A J Ab Initio Study of Mode-Resolved Phonon Transmission at Si/Ge Interfaces Using Atomistic Green's Functions. *Physical Review B* **96** 104310 (2017)

[47] Zhang, W, Fisher, T S, and Mingo, N Simulation of Interfacial Phonon Transport in Si–Ge Heterostructures Using an Atomistic Green's Function Method. *Journal of Heat Transfer* **129** 483 (2006)

[48] Lin, J, Shenghong, J, Xingang, L, and Xing, Z Tuning Phonon Transmission and Thermal Conductance by Roughness at Rectangular and Triangular Si/Ge Interface. *Materials Research Express* **3** 095024 (2016)

[49] Merabia, S and Termentzidis, K Thermal Boundary Conductance across Rough Interfaces Probed by Molecular Dynamics. *Physical Review B* **89** 054309 (2014)

[50] English, T S *et al.* Enhancing and Tuning Phonon Transport at Vibrationally Mismatched Solid-Solid Interfaces. *Physical Review B* **85** 035438 (2012)

[51] Sun, L and Murthy, J Y Molecular Dynamics Simulation of Phonon Scattering at Silicon/Germanium Interfaces. *Journal of Heat Transfer* **132** 102403 (2010)

[52] Alkurdi, A, Pailhès, S, and Merabia, S Critical Angle for Interfacial Phonon Scattering: Results from Ab Initio Lattice Dynamics Calculations. *Applied Physics Letters* **111** 093101 (2017)

[53] Tian, Z, Lee, S, and Chen, G Heat Transfer in Thermoelectric Materials and Devices. *Journal of Heat Transfer* **135** 061605 (2013)

[54] Gudiksen, M S *et al.* Growth of Nanowire Superlattice Structures for Nanoscale Photonics and Electronics. *Nature* **415** 617 (2002)

[55] Nakamura, S The Roles of Structural Imperfections in Ingan-Based Blue Light-Emitting Diodes and Laser Diodes. *Science* **281** 956 (1998)

[56] Trigo, M *et al.* Confinement of Acoustical Vibrations in a Semiconductor Planar Phonon Cavity. *Physical Review Letters* **89** 227402 (2002)

[57] Fan, X *et al.* SiGeC/Si Superlattice Microcoolers. *Applied Physics Letters* **78** 1580 (2001)

[58] Fan, X *et al.* High Cooling Power Density SiGe/Si Microcoolers. *Electronics Letters* **37** 126 (2001)

[59] Vashaee, D and Shakouri, A Thermionic Power Generation at High Temperatures Using SiGe/Si Superlattices. *Journal of Applied Physics* **101** 053719 (2007)

[60] Puurtinen, T and Maasilta, I Low-Temperature Coherent Thermal Conduction in Thin Phononic Crystal Membranes. *Crystals* **6** 72 (2016)

[61] Chen, G Size and Interface Effects on Thermal Conductivity of Superlattices and Periodic Thin-Film Structures. *Journal of Heat Transfer* **119** 220 (1997)

[62] Lee, S, Cahill, D G, and Venkatasubramanian, R Thermal Conductivity of Si-Ge Superlattices. *Applied physics letters* **70** 2957 (1997)

[63] Maldovan, M Phonon Wave Interference and Thermal Bandgap Materials. *Nat Mater* **14** 667 (2015)

[64] Daly, B C, Maris, H J, Imamura, K, and Tamura, S Molecular Dynamics Calculation of the Thermal Conductivity of Superlattices. *Physical Review B* **66** 024301 (2002)

[65] Simkin, M V and Mahan, G D Minimum Thermal Conductivity of Superlattices. *Physical Review Letters* **84** 927 (2000)

[66] Capinski, W S and Maris, H J Thermal Conductivity of GaAs/AlAs Superlattices. *Physica B: Condensed Matter* **219** 699 (1996)

[67] Chen, Y *et al.* Minimum Superlattice Thermal Conductivity from Molecular Dynamics. *Physical Review B* **72** 174302 (2005)

[68] Konstantinos, T, Patrice, C, Jean-Yves, D, and Abdelhak, S Thermal Conductivity of Gaas/Alas Superlattices and the Puzzle of Interfaces. *Journal of Physics: Condensed Matter* **22** 475001 (2010)

[69] Latour, B, Volz, S, and Chalopin, Y Microscopic Description of Thermal-Phonon Coherence: From Coherent Transport to Diffuse Interface Scattering in Superlattices. *Physical Review B* **90** 014307 (2014)

[70] Huberman, S C, Larkin, J M, Mcgaughey, A J H, and Amon, C H Disruption of Superlattice Phonons by Interfacial Mixing. *Physical Review B* **88** 155311 (2013)

[71] Landry, E S and Mcgaughey, A J H Effect of Interfacial Species Mixing on Phonon Transport in Semiconductor Superlattices. *Physical Review B* **79** 075316 (2009)

[72] Garg, J and Chen, G Minimum Thermal Conductivity in Superlattices: A First-Principles Formalism. *Physical Review B* **87** 140302 (2013)

[73] Chen, P *et al.* Role of Surface-Segregation-Driven Intermixing on the Thermal Transport through Planar Si/Ge Superlattices. *Physical Review Letters* **111** 115901 (2013)

[74] Garg, J, Bonini, N, and Marzari, N High Thermal Conductivity in Short-Period Superlattices. *Nano Letters* **11** 5135 (2011)

[75] Tian, Z, Esfarjani, K, and Chen, G Green's Function Studies of Phonon Transport across Si/Ge Superlattices. *Physical Review B* **89** 235307 (2014)

[76] Chen, G and Neagu, M Thermal Conductivity and Heat Transfer in Superlattices. *Applied Physics Letters* **71** 2761 (1997)

[77] Liu, C-K *et al.* Thermal Conductivity of Si/SiGe Superlattice Films. *Journal of Applied Physics* **104** 114301 (2008)

[78] Aksamija, Z and Knezevic, I Thermal Conductivity of $Si_{1-x}Ge_x/Si_{1-y}Ge_y$ Superlattices: Competition between Interfacial and Internal Scattering. *Physical Review B* **88** 155318 (2013)

[79] Mei, S and Knezevic, I Thermal Conductivity of III-V Semiconductor Superlattices. *Journal of Applied Physics* **118** 175101 (2015)

[80] Capinski, W S *et al.* Thermal-Conductivity Measurements of GaAs/AlAs Superlattices Using a Picosecond Optical Pump-and-Probe Technique. *Physical Review B* **59** 8105 (1999)

[81] Huxtable, S T *et al.* Thermal Conductivity of Si/SiGe and SiGe/SiGe Superlattices. *Applied Physics Letters* **80** (2002)

[82] Borca-Tasciuc, T *et al.* Thermal Conductivity of Symmetrically Strained Si/Ge Superlattices. *Superlattices and Microstructures* **28** 199 (2000)

[83] Yang, B *et al.* Measurements of Anisotropic Thermoelectric Properties in Superlattices. *Applied Physics Letters* **81** 3588 (2002)

[84] Liu, W L *et al.* Anisotropic Thermal Conductivity of Ge Quantum-Dot and Symmetrically Strained Si/Ge Superlattices. *Journal of Nanoscience and Nanotechnology* **1** 39 (2001)

[85] Cheaito, R *et al.* Interplay between Total Thickness and Period Thickness in the Phonon Thermal Conductivity of Superlattices from the Nanoscale to the Microscale: Coherent Versus Incoherent Phonon Transport. *Physical Review B* **97** 085306 (2018)

[86] Kressel, H and Ettenberg, M Low-Threshold Double Heterojunction AlGaAs/GaAs Laser Diodes: Theory and Experiment. *Journal of Applied Physics* **47** 3533 (1976)

[87] Chowdhury, I *et al.* On-Chip Cooling by Superlattice-Based Thin-Film Thermoelectrics. **4** 235 (2009)

[88] Hartmann, J M *et al.* Reduced Pressure–Chemical Vapor Deposition of Ge Thick Layers on Si(001) for 1.3–1.55-um Photodetection. *Journal of Applied Physics* **95** 5905 (2004)

[89] Hurwitz, C E, Rossi, J A, Hsieh, J J, and Wolfe, C M Integrated GaAs-AlGaAs Double-Heterostructure Lasers. *Applied Physics Letters* **27** 241 (1975)

[90] Colace, L *et al.* Efficient High-Speed near-Infrared Ge Photodetectors Integrated on Si Substrates. *Applied Physics Letters* **76** 1231 (2000)

[91] Köck, A, Gornik, E, Hauser, M, and Beinstingl, W Strongly Directional Emission from AlGaAs/GaAs Light-Emitting Diodes. *Applied Physics Letters* **57** 2327 (1990)

[92] Schnitzer, I, Yablonovitch, E, Caneau, C, and Gmitter, T J Ultrahigh Spontaneous Emission Quantum Efficiency, 99.7% Internally and 72% Externally, from AlGaAs/GaAs/AlGaAs Double Heterostructures. *Applied Physics Letters* **62** 131 (1993)

[93] Chávez-Ángel, E *et al.* Reduction of the Thermal Conductivity in Free-Standing Silicon Nano-Membranes Investigated by Non-Invasive Raman Thermometry. *APL Materials* **2** 012113 (2014)

[94] Cheaito, R *et al.* Experimental Investigation of Size Effects on the Thermal Conductivity of Silicon-Germanium Alloy Thin Films. *Physical Review Letters* **109** 195901 (2012)

[95] Liu, W and Asheghi, M Thermal Conduction in Ultrathin Pure and Doped Single-Crystal Silicon Layers at High Temperatures. *Journal of Applied Physics* **98** 123523 (2005)

[96] Mazumder, S and Majumdar, A Monte Carlo Study of Phonon Transport in Solid Thin Films Including Dispersion and Polarization. *Journal of Heat Transfer* **123** 749 (2001)

[97] Wang, X and Huang, B Computational Study of in-Plane Phonon Transport in Si Thin Films. *Scientific Reports* **4** 6399 (2014)

[98] Jeong, C, Datta, S, and Lundstrom, M Thermal Conductivity of Bulk and Thin-Film Silicon: A Landauer Approach. *Journal of Applied Physics* **111** 093708 (2012)

[99] Turney, J E, Mcgaughey, A J H, and Amon, C H In-Plane Phonon Transport in Thin Films. *Journal of Applied Physics* **107** 024317 (2010)

[100] Aksamija, Z and Knezevic, I Anisotropy and Boundary Scattering in the Lattice Thermal Conductivity of Silicon Nanomembranes. *Physical Review B* **82** 045319 (2010)

[101] Gomes, C J, Madrid, M, Goicochea, J V, and Amon, C H In-Plane and out-of-Plane Thermal Conductivity of Silicon Thin Films Predicted by Molecular Dynamics. *Journal of Heat Transfer* **128** 1114 (2006)

[102] Malhotra, A and Maldovan, M Surface Scattering Controlled Heat Conduction in Semiconductor Thin Films. *Journal of Applied Physics* **120** 204305 (2016)

[103] Beckmann, P and Spizzichino, A 1963 *The Scattering of Electromagnetic Waves from Rough Surfaces* Vol. 4 (New York: MacMillan).

[104] Asheghi, M, Leung, Y K, Wong, S S, and Goodson, K E Phonon-Boundary Scattering in Thin Silicon Layers. *Applied Physics Letters* **71** 1798 (1997)

[105] Bezák, V and Krempaský, J A Phenomenological Theory of the Thermal Conductivity of Thin Films. *Czechoslovak Journal of Physics B* **18** 1264 (1968)

[106] Hood, R Q, Falicov, L M, and Penn, D R Effects of Interfacial Roughness on the Magnetoresistance of Magnetic Metallic Multilayers. *Physical Review B* **49** 368 (1994)

[107] Malhotra, A, Kothari, K, and Maldovan, M Enhancing Thermal Transport in Layered Nanomaterials. *Scientific Reports* **8** 1880 (2018)

[108] Malhotra, A, Kothari, K, and Maldovan, M Modulating Thermal Conduction Via Phonon Spectral Coupling. *Journal of Applied Physics* **124** 124302 (2018)

[109] Kothari, K, Malhotra, A, and Maldovan, M Unconventional Thermal Transport in Thin Film-on-Substrate Systems. *Journal of Physics D: Applied Physics* **51** 365302 (2018)

[110] Colace, L *et al.* Metal–Semiconductor–Metal near-Infrared Light Detector Based on Epitaxial Ge/Si. *Applied Physics Letters* **72** 3175 (1998)

[111] Colace, L, Masini, G, and Assanto, G Ge-on-Si Approaches to the Detection of near-Infrared Light. *IEEE Journal of Quantum Electronics* **35** 1843 (1999)

[112] Masini, C *et al.* High-Performance P-I-N Ge on Si Photodetectors for the near Infrared: From Model to Demonstration. *IEEE Transactions on Electron Devices* **48** 1092 (2001)

[113] Maldovan, M Thermal Energy Transport Model for Macro-to-Nanograin Polycrystalline Semiconductors. *Journal of Applied Physics* **110** 114310 (2011)

[114] Esfarjani, K, Chen, G, and Stokes, H T Heat Transport in Silicon from First-Principles Calculations. *Physical Review B* **84** 085204 (2011)

[115] Hamilton, R A H and Parrott, J E Variational Calculation of the Thermal Conductivity of Germanium. *Physical Review* **178** 1284 (1969)

[116] Maldovan, M Narrow Low-Frequency Spectrum and Heat Management by Thermocrystals. *Physical Review Letters* **110** 025902 (2013)

[117] Mingo, N *et al.* "Nanoparticle-in-Alloy" Approach to Efficient Thermoelectrics: Silicides in Sige. *Nano Letters* **9** 711 (2009)

[118] Kothari, K and Maldovan, M Phonon Surface Scattering and Thermal Energy Distribution in Superlattices. *Scientific Reports* **7** 5625 (2017)

[119] Strauch, D and Dorner, B Phonon Dispersion in GaAs. *Journal of Physics: Condensed Matter* **2** 1457 (1990)

[120] Lindsay, L, Broido, D A, and Reinecke, T L Ab Initio. *Physical Review B* **87** 165201 (2013)

[121] Evans, C A *et al.* Thermal Modeling of Terahertz Quantum-Cascade Lasers: Comparison of Optical Waveguides. *IEEE Journal of Quantum Electronics* **44** 680 (2008)

[122] Afromowitz, M A Thermal Conductivity of $Ga_{1-x}Al_xAs$ Alloys. *Journal of Applied Physics* **44** 1292 (1973)

[123] Tengfei, L *et al.* Gallium Arsenide Thermal Conductivity and Optical Phonon Relaxation Times from First-Principles Calculations. *EPL (Europhysics Letters)* **101** 16001 (2013)

[124] Balandin, A and Wang, K L Significant Decrease of the Lattice Thermal Conductivity Due to Phonon Confinement in a Free-Standing Semiconductor Quantum Well. *Physical Review B* **58** 1544 (1998)

[125] Yu, X Y, Chen, G, Verma, A, and Smith, J S Temperature Dependence of Thermophysical Properties of GaAs/AlAs Periodic Structure. *Applied Physics Letters* **67** 3554 (1995)

[126] Johnson, W R, Gunapala, S, Mumolo, J, and Johnson, D, in *Photonic Devices + Applications* (SPIE, 2007), p. 10.

[127] Jorge, S, José Luis, P, and Juan, J Nanoscale Effects on the Thermal and Mechanical Properties of Algaas/Gaas Quantum Well Laser Diodes: Influence on the Catastrophic Optical Damage. *Journal of Physics D: Applied Physics* **50** 235101 (2017)

[128] Adachi, S GaAs, AlAs, and $Al_xGa_{1-x}As$: Material Parameters for Use in Research and Device Applications. *Journal of Applied Physics* **58** R1 (1985)

[129] Barron, C C, Mahon, C J, Thibeault, B J, and Coldren, L A Design, Fabrication and Characterization of High-Speed Asymmetric Fabry-Perot Modulators for Optical Interconnect Applications. *Optical and Quantum Electronics* **25** S885 (1993)

[130] Goswami, S *et al.* Low-Power Exciton-Based Heterojunction Bipolar Transistors for Thresholding Logic Applications. *IEEE Journal of Quantum Electronics* **27** 760 (1991)

[131] Kothari, K and Maldovan, M Analysis of in-Plane Thermal Phonon Transport in III–V Compound Semiconductor Superlattices. *Nanoscale and Microscale Thermophysical Engineering* **22** 239 (2018)

[132] Luckyanova, M N *et al.* Anisotropy of the Thermal Conductivity in GaAs/AlAs Superlattices. *Nano Letters* **13** 3973 (2013)

[133] Mizuno, H, Mossa, S, and Barrat, J-L Beating the Amorphous Limit in Thermal Conductivity by Superlattices Design. *Scientific Reports* **5** 14116 (2015)

[134] Kim, K, He, J, Ganeshan, B, and Liu, J Disorder Enhanced Thermal Conductivity Anisotropy in Two-Dimensional Materials and Van Der Waals Heterostructures. *Journal of Applied Physics* **124** 055104 (2018)

[135] Tian, X, Itkis, M E, Bekyarova, E B, and Haddon, R C Anisotropic Thermal and Electrical Properties of Thin Thermal Interface Layers of Graphite Nanoplatelet-Based Composites. *Scientific Reports* **3** 1710 (2013)

[136] Burroughes, J H H-Mesfet Compatible Gaas/Algaas Msm Photodetector. *IEEE Photonics Technology Letters* **3** 660 (1991)

[137] Tashiro, T *et al.* A Selective Epitaxial Sige/Si Planar Photodetector for Si-Based Oeic's. *IEEE Transactions on Electron Devices* **44** 545 (1997)

[138] Ponomareva, I, Srivastava, D, and Menon, M Thermal Conductivity in Thin Silicon Nanowires: Phonon Confinement Effect. *Nano Letters* **7** 1155 (2007)

[139] Pop, E Energy Dissipation and Transport in Nanoscale Devices. *Nano Research* **3** 147 (2010)

[140] Polanco, C A and Ghosh, A W Enhancing Phonon Flow through One-Dimensional Interfaces by Impedance Matching. *Journal of Applied Physics* **116** 083503 (2014)

[141] Malhotra, A and Maldovan, M Impact of Phonon Surface Scattering on Thermal Energy Distribution of Si and Sige Nanowires. *Scientific Reports* **6** 25818 (2016)

[142] Maldovan, M and Thomas, E L 2009 *Periodic Materials and Interference Lithography: For Photonics, Phononics and Mechanics* (John Wiley & Sons).

[143] Chen, G Phonon Wave Heat Conduction in Thin Films and Superlattices. *Journal of Heat Transfer* **121** 945 (1999)

[144] Garg, J, Bonini, N, Kozinsky, B, and Marzari, N Role of Disorder and Anharmonicity in the Thermal Conductivity of Silicon-Germanium Alloys: A First-Principles Study. *Physical Review Letters* **106** 045901 (2011)

[145] Priyadarshi, P, Sharma, A, Mukherjee, S, and Muralidharan, B Superlattice Design for Optimal Thermoelectric Generator Performance. *Journal of Physics D: Applied Physics* **51** 185301 (2018)

[146] Wang, Y, Gu, C, and Ruan, X Optimization of the Random Multilayer Structure to Break the Random-Alloy Limit of Thermal Conductivity. *Applied Physics Letters* **106** 073104 (2015)

[147] Koh, Y K and Cahill, D G Frequency Dependence of the Thermal Conductivity of Semiconductor Alloys. *Physical Review B* **76** 075207 (2007)

[148] Zhu, J *et al.* Ultrafast Thermoreflectance Techniques for Measuring Thermal Conductivity and Interface Thermal Conductance of Thin Films. *Journal of Applied Physics* **108** 094315 (2010)

[149] Maldovan, M Specular Reflection Leads to Maximum Reduction in Cross-Plane Thermal Conductivity. *Journal of Applied Physics* **125** 224301 (2019)